OPTO-ELECTRICAL STUDIES OF SELF-ASSEMBLED MONOLAYER DIODES AND BULK HETERO-JUNCTION ORGANIC PHOTOVOLTAIC DEVICES

by

Alexandre Ndobe

A dissertation submitted to the faculty of
The University of Utah
in partial fulfillment of the requirements for the degree of

Doctor of Philosophy

in

Physics

Department of Physics and Astronomy

The University of Utah

December 2014

Copyright © Alexandre Ndobe 2014

All Rights Reserved

The University of Utah Graduate School

STATEMENT OF DISSERTATION APPROVAL

The dissertation of **Alexandre Ndobe**

has been approved by the following supervisory committee members:

Zeev Valentine Vardeny	, Chair	**12/12/2005** Date Approved
Eugene Mishchenko	, Member	**12/12/2005** Date Approved
Robert Wayne Springer	, Member	**05/12/2005** Date Approved
Ajay Nahata	, Member	**12/12/2005** Date Approved
Vladimir Burtman	, Member	**12/12/2005** Date Approved

and by **Carleton DeTar**, Chair/Dean of

the Department/College/School of **Physics and Astronomy**

and by David B. Kieda, Dean of The Graduate School.

ABSTRACT

The present dissertation is the result of our studies of the optical and electrical properties of self-assembled monolayer (SAM) diodes and bulk heterojunction organic photovoltaic (BOPV) devices.

In our studies of SAM diodes, we fabricated solid-state mixtures of two different kinds of molecules; 1,4 benzene-dimethane-thiol (MeBDT) and 1-pentanethiol (PT). By varying the concentration r of MeBDT with respect to PT, we can go from a regime of isolated molecular wires ($10^{-8} < r < 10^{-4}$) to a regime of aggregated molecular wire ($r > 10^{-3}$).

For $r = 0$, we found that a potential barrier dominated the transport properties of the device. In the isolated molecules regime, the conductance of MeBDT dominates the transport. In this regime, because of the linearity of the conductance with respect to r, we were able to obtain a "single molecule resistance" at $V = 0.1V$ of $R_M = 6 \times 10^{-9}$.

In the aggregated molecules regime, an ohmic response in the current-voltage (I-V) characteristics was observed for bias voltages $\leq 0.5V$ with the appearance of a new band in the differential conductance around $V = 0$ along with a new double band in the optical gap at $2.4eV$ resulting in yellow/red photoluminescence emission.

Opto-electrical studies of BOPV devices reveal that there are very few similarities between these types of solar cells and conventional solar cells. From simulations and experiemental measurements of the I-V characteristics, we found that while the open voltage circuit (V_{oc}) is important for engineers, it carries no intrinsic information of the device. It cannot exceed the built-in potential of the device ($V_{built-in}$). The later origin was found to be dependent on electrode work function difference for a non-Ohmic contact configuration and on the active layer's blend in an Ohmic contact configuration. In a bid to improve BOPV device performance, we added to the blend spin 1/2 radical molecules. At concentration ($\leq$ 2%), an increase in device performance was observed. The principal cause for this increase was the increase in the carrier's mobility as a function of the concentration of radicals.

First and Foremost to my Lord and Savior Jesus-Christ, to my Darling and our little angels Nathan, Rose and Esther

CONTENTS

ABSTRACT . . . . . **iii**

LIST OF FIGURES . . . . . **vii**

LIST OF TABLES . . . . . **xii**

LIST OF ACRONYMS . . . . . **xiii**

ACKNOWLEDGEMENTS . . . . . **xv**

CHAPTERS

1. INTRODUCTION **1**

1.1 Background and motivation 1
1.1.1 Molecular wires 1
1.1.2 Organic solar cells 3
1.2 Classes of organic solar cells 4
1.2.1 Dye-sensitized solar cells 4
1.2.2 "Bilayer"solar cells 4
1.2.3 Bulk hetero-junction solar cells 7
1.3 Organic solar cell characterization 7
1.4 Outline 9

2. EXPERIMENTAL TECHNIQUES **10**

2.1 Single molecule transport study experiments 10
2.1.1 Self-assembled monolayer (SAM) growth 10
2.1.2 Device fabrication 13
2.1.3 Device characterization 17
2.2 Organic photovoltaic device fabrication and characterization 19
2.2.1 Sample preparation 19
2.2.2 OPV characterization 26
2.2.3 Optical measurement 29
2.2.4 Admittance spectroscopy 32

3. TRANSPORT STUDIES OF SELF-ASSEMBLED MONOLAYERS . . . **41**

3.1 Evidence for SAM device formation 42
3.1.1 Conductive and nonconductive molecules 42
3.1.2 Monolayer formation 43
3.1.3 Electrode connectivity 45
3.1.4 From single molecule to aggregated molecules 45
3.2 Single molecule transport 47
3.2.1 Devices with $r = 0$ 47

3.2.2 Devices with $10^{-7} < r < 10^{-4}$ 50
3.2.3 Single molecule resistance 56
3.2.4 Modelization 56
3.3 Transport studies of aggregated molecules 58
3.3.1 Transport studies of Au/SAM/Au diodes 58
3.3.2 The formation of gap states in aggregated Au/SAM/Au devices 58
3.3.3 Gap states in Al/SAM/Al devices 62
3.4 Conclusion 67

4. BULK HETERO-JUNCTION ORGANIC PHOTOVOLTAIC DEVICE PHYSICS 70

4.1 B-OPV I-V characteristics 70
4.1.1 General mechanisms in B-OPV 70
4.1.2 Loss mechanisms in B-OPV 73
4.1.3 I-V characteristics of B-OPV 77
4.2 Towards a high efficiency B-OPV 84
4.2.1 Series resistance optimization 84
4.2.2 Best B-OPV device obtained 88
4.3 Origin of V_{oc} 93
4.3.1 Introduction 93
4.3.2 V_{oc} vs. $V_{built-in}$ 94
4.3.3 Origin of $V_{built-in}$ 96
4.4 Discussion and conclusion 102

5. SPIN 1/2 RADICAL EFFECT ON BULK HETERO-JUNCTION ORGANIC PHOTOVOLTAICS 103

5.1 Spin 1/2 radical effect on various polymer blends 104
5.1.1 Experimental 104
5.1.2 Spin 1/2 radical effect on MEHPPV:PCBM blends 104
5.1.3 Spin 1/2 radical effect on P3HT:PCBM blends 104
5.1.4 Discussion 106
5.2 Origin of the short circuit current increase 106
5.2.1 Radical effects on the photocurrent action spectrum 106
5.2.2 Radical effects on the quantum efficiency polaron generation 107
5.2.3 Radical effects on the polaron recombination time 109
5.2.4 Radical effects on the film morphology 109
5.2.5 Radical effects on the carriers' mobility 113
5.2.6 Mobility dependence on radical concentration 120
5.3 Conclusion 126

6. CONCLUSION 129

REFERENCES 131

LIST OF FIGURES

1.1 Schematic layout of an organic solar cell. 5

1.2 Schematic layout of a dye-sensitized cell. 5

1.3 Schematic band diagram of a bilayer device (a) and a bulk hetero-junction (b). The numbers refer to the operation processes explained in the text. The dashed line represents the energy levels of the acceptor, while the full lines indicate the energy level of the donor in the solar cell. 6

1.4 Typical J-V characteristics of an organic solar cell in the dark (dashed line) and illumination (solid line) conditions. The short-circuit current density (J_{SC}) and open-circuit voltage (V_{OC}) are shown. The maximum output power (P_{max}) is given by the rectangle $J_{max} \times V_{max}$. 8

2.1 Structure of SAM molecule 11

2.2 The fabrication process (schematic) of SAM SSM diodes at small ratio r of molecular wire (Me-BDT in red) to molecular insulator (PT in green). A: evaporation of an Au base electrode; B: SAM growth of the appropriate molecule mixture on the bottom Au film; C: evaporation of the upper Au electrode; D: I-V measurement set-up, where the contacts are made using silver paint. 14

2.3 The home-made high vacuum based Shlenk line and reactive vessel. The Shlenk line consists of 9 stages: glass diffusion pump (1); LN2 trap (2); vacuum and Ar gas line (3); reactive vessel (4); distillation toluene system (5); rough pump line (6); high vacuum gauge (7); low pressure gauge (8); and distillation PT system (9). The reactive vessel (4) has connection to the Shlenk line through a vacuum tube. The two input ports are for: (a) washing the reactive vessel by vapor of distilled toluene that is delivered through the supply line, and (b) input/output of the reactive precursors in solution form and (c) washing excess reagents from the reactive vessel. 16

2.4 I-V device characteristic measurement configurations (a) Two probes and (b) four probes. 18

2.5 Example of I-V characteristic obtained from characterization of a SAM device at 150K. 18

2.6 Molecular structure of PCBM. 20

2.7 Molecular structure of P3HT. 20

2.8 Molecular structure of PEDOT:PSS. 22

2.9 Pattern on the substrate after ITO etching: the grey pattern represents ITO (a), the device top view after all steps: white strips represent Al, yellow represents the spin-coated active layer and the black area represents the glass while the pattern represents ITO (b) and cross section view of the completed device (c). 24

2.10 OPV I-V measurement setup (a), Monochromatic I-V measurement (b) and IPCE measurement setup (c). 27

2.11 Example of OPV I-V under AM 1.5 illumination 28

2.12 CW PA and PL setup. 31

2.13 Simulation of frequency dependent photoinduced absorption with a $\tau_{eff} = 1ms$. 33

2.14 Simulation of the capacitance spectrum of a trap free space charge limited current device with $C_{geo} = 0.1nF$ and $\tau_{DC} = 10^{-2}$, 10^{-4} 38

2.15 Simulation of the capacitance spectrum of a dispersive space charge limited current device with $C_{geo} = 1F$, $\tau_{DC} = 10^{-4}$ and M=0,0.01,0.01,0.3. 40

2.16 Admittance spectroscopy setup. 40

3.1 Basic optical measurements of the fabricated SAM devices. (a) The optical reflectivity spectrum of SAM films with $r = 10^{-2}$ (red dashed line, 1), and $r = 10^{-6}$ (black solid line, 2) that show a prominent feature at the HOMO-LUMO transition of the Me-BDT molecule at about $5\,eV$. For $r = 10^{-2}$ there is another optical feature in the visible spectral range associated with Me-BDT aggregates. 44

3.2 Ellipsometry spectra of two optical constants: ψ (dashed line) and Δ (dot line) that were measured at three different angles, from which a film thickness of $\sim 1\,nm$ was derived. The solid lines through the data points are model fittings. 44

3.3 FTIR absorption spectra of the Me-BDT molecule bonded to the upper electrode that shows an ir-active AuS-C stretching vibration (blue line), CoS-C stretching vibration (black line) compared with a reference film that shows the ir-active S-C stretching vibration (red line). 46

3.4 Ellipsometry spectra of two optical constants: ψ (dashed line) and Δ (dotted line) that were measured at three different angles, from which a film thickness of $\sim 1\,nm$ was derived. The solid lines through the data points are model fittings. 48

3.5 Electrical transport studies of a SAM device made of PT ($r = 0$) at various temperatures. (a) and (b) show the measured I-V characteristics; (c) shows the differential conductivity spectra obtained from (a). The inset in (c) is dI/dV vs. V at 15 K. 49

3.6 Arrhenius plots of the current at different biasing voltages for the SAM device of PT (a), and SSM SAM device with $r = 10^{-6}$ (b). Red lines are linear fits for ln(I) rise at high temperatures. 51

3.7 Electrical transport studies of a SAM device made of SSM with $r = 10^{-6}$ at various temperatures. (a) and (b) show the measured I-V characteristics at different voltage ranges; (c) shows the differential conductivity spectra , dI/dV vs. V obtained from (a). The inset in (c) is dI/dV vs. V at 15 K. 52

3.8 SSM SAM devices at room temperature with $r = 10^{-5}$ (a) and (b); and $r = 10^{-7}$ (c) and (d). 53

3.9 Room temperature current of SSM SAM devices fabricated with various r-values vs. r. A linear line through the data points is also shown indicating the dominant role of the isolated Me-BDT conductivity superposition. 54

3.10 Room temperature current of SSM SAM devices fabricated with various r-values vs. r. A linear line through the data points is also shown indicating the dominant role of the isolated Me-BDT conductivity superposition. 59

3.11 Normalized optical reflectivity spectra of SAM films on Au and Al electrodes, respectively, at two r-values: (i) $r = 10^{-6}$ for isolated Me-BDT; and (ii) $r = 10^{-2}$ for molecular aggregates. The Me-BDT HOMO-LUMO transition at $\sim 4.5\,eV$, and the optical transition related to Me-BDT aggregates at $\sim 2.3\,eV$ are assigned. 60

3.12 Electrical transport measurements of SAM diodes with $r = 10^{-6}$ at various temperatures, showing isolated Me-BDT behavior. (a) I-V characteristics; (b) differential conductance spectrum obtained from (a). 61

3.13 Normalized optical reflectivity spectra of SAM films on Au and Al electrodes, respectively, at two r-values: (i) $r = 10^{-6}$ for isolated Me-BDT; and (ii) $r = 10^{-2}$ for molecular aggregates. The Me-BDT HOMO-LUMO transition at $\sim 4.5eV$, and the optical transition related to Me-BDT aggregates at $\sim 2.3\,eV$ are assigned. 63

3.14 Electrical transport measurements of aggregated SAM diodes with $r = 10^{-2}$ with Al electrodes (Al-SAM-Al) at various temperatures. (a) I-V characteristics; (b) differential conductance spectrum obtained from (a). 65

3.15 SAM diode with bottom Al and upper Au electrodes (Au-SAM-Al). The insert in (b) shows a zoom at low bias 66

4.1 Comparison of the absorption spectra of the active components with the AM1.5 solar spectrum. 71

4.2 Schematic description of Dexter exciton transfer (a), Förster exciton transfer (b) and the result of exciton transfer. 75

4.3 Aggregates configuration and their respective allowed and forbidden transitions (a) J aggregate (b) H aggregate. 76

4.4 I-V in the dark with the different transport regimes. 79

4.5 Equivalent circuit (a) In the dark (b) Under illumination. 79

4.6 IV- curves of a bulk hetero-junction solar cell measured under different illumination intensities (boxes) with fitted curves using the standard 1-diode-model (lines). Values for the parameters n and I_0 are given for each light intensity in the legend. The light intensity is given by the value of the optical density (OD) of the various grey filters and the light intensity of 110 $mWcm^2$ at $OD = 0$. . . 80

4.7 I-V under various illumination intensities fitted with the corrected model. . . . 82

4.8 I-V under illumination fitted with the corrected model. 82

4.9 Simulation of active layer thickness influence on I-V under illumination (a) I-V characteristic (b) FF and V_{oc} as a function of active layer thickness. 83

4.10 Simulation of $\mu \times \tau$ influence on I-V (a)I-V characteristic (b) FF and V_{oc} as a function of $\mu \times \tau$. 85

4.11 Simulation of illumination power influence on I-V (a) I-V characteristic (b) FF and V_{oc} as a function of illumination power. 86

4.12 I-V characteristics of devices with different PEDOT conductivity. 87

4.13 I-V characteristics of devices with different active layer thickness. 89

4.14 I-V characteristics of devices with and without LiF. 90

4.15 I-V characteristics the best device obtained with P3HT:PCBM. 91

4.16 I-V characteristics of the best device obtained with P3HT:JAL; the insert is a table of the obtained parameters. 92

4.17 Illumination dependence of MDMOPPV:PCBM (a) and P3HT:PCBM (b) I-V characteristics. 95

4.18 Energy diagram of ITO/PEDOT/P3HT:PCBM/Al or Ag. 97

4.19 I-V characteristics of ITO/PEDOT/P3HT:PCBM/X; (a) X = Ag (b) X = Al. 97

4.20 I-V characteristics of ITO/PEDOT/P3HT:PCBM/LiF/X;(a) X = Mg (b) X = Ag (c) X = Al (d) X = Au. 98

4.21 I-V characteristics of MDMOPPV:PCBM (a), P3HT:PCBM (b) and P3DT:PCBM (c) 100

4.22 Built-in voltage of a P3HT:PCBM device (a) and open circuit voltage of a silicon photodiode (b) as a function of temperature. 101

5.1 IV- curves device: ITO/PEDOT/MEHPPV:PCBM+TEMPO(1:2 + x%)/Al with $x = 0\%$, $x = 10\%$ and $x = 20\%$ at AM 1.5 elimination. 105

5.2 IV-curves device: ITO/PEDOT/P3HT:PCBM+TEMPO(1:1 + x%)/Al with $x = 0\%$, $x = 2\%$ and $x = 5\%$ (a) Batch 1 (b) Batch 2 under AM 1.5 illumination. 105

5.3 Action spectrum of: ITO/PEDOT/MEHPPV:PCBM+TEMPO(1:2 + x%)/Al with $x = 0\%$, $x = 10\%$ and $x = 20\%$. 108

5.4 Energy diagram of photoexcited film. 108

5.5 Photobleaching of MEHPPV + x% radicals. 110

5.6 PA frequency dependence (both in phase and quadrature) of MEHPPV + x% radicals at room temperature. 111

5.7 AFM images of P3HT + x% Radicals (a) Pure (b) 2% Radicals (c) 5% Radicals. 112

5.8 Impedance spectrum of pure MEHPPV fitted with the trap limited space charge limited current model developed in Chapter 2. 114

5.9 Field dependent mobility of MEHPPV as a function of radical concentration. . 117

5.10 Impedance spectrum of pure P3HT fitted with the trap limited space charge limited current model developed in Chapter 2. 118

5.11 Field dependent mobility of P3HT as a function of radical concentration 121

5.12 Diagram illustrating the Pauli Blockade process. 123

5.13 Current as a function of trap density when there are no radicals in the system. 125

5.14 Current as a function of radical density. 127

LIST OF TABLES

4.1 Build in voltage as a function of work function difference 100

5.1 Fit parameters for the impedance spectrum of pure MEHPPV 115

5.2 Fit parameters for the impedance spectrum of MEHPPV + 2% radicals 115

5.3 Fit parameters for the impedance spectrum of MEHPPV + 5% radicals 115

5.4 Fit parameters for the field dependence of the mobility for MEHPPV as a function of radical concentration 117

5.5 Fit parameters for the impedance spectrum of pure P3HT 119

5.6 Fit parameters for the impedance spectrum of P3HT + 2% radicals 119

5.7 Fit parameters for the impedance spectrum of P3HT + 5% radicals 119

5.8 Fit parameters for the field dependence of the mobility for P3HT as a function of radical concentration 121

LIST OF ACRONYMS

Acronym	Definition
AFM	Atomic Force Microscopy
$BOPV$	Bulk Heterojunction Organic Photovoltaic
C_{60}	Carbon Fullerene with 60 Carbon Atoms
COB	Continium Of Band
CW	Continuous Wave
D/A	Donor/Acceptor
DCS	Differential Conductance Spectrum
$DSSC$	Dye-Sensitized Solar Cell
DNA	Deoxyribonucleic Acid
EHP	Electron Hole Pair
ETL	Electron Transport Layer
FF	Fill Factor
$FTIR$	Fourier Transform Infrared Spectroscopy
HCL	Hydrochloric acid
$HOMO$	Highest Occupied Molecular Orbital
HTL	Hole Transport Layer
$IPCE$	Incident Photon To Electron Conversion Efficiency
ITO	Indium Tin Oxide
IV	Current Voltage
IR	Infra-Red
$LEAD$	Low Energy Atomic Diffraction
$LUMO$	Lowest Unoccupied Molecular Orbital
$MDMOPPV$	Poly[2-Methoxy-5-(3,7-diMethylOctyloxy)-1,4-phenylene vinylene]
$MEBDT$	1,4-Methane-Benzenedithiol
$MEHPPV$	Poly(2-Methoxy-5-(2-Ethylhexyloxy)-P-Phenylene Vinyle)
MIM	Metal Insulator Metal
MW	Molecular Wire
OPV	Organic Photovoltaic
$OLED$	Organic Light Emitting Diode
$P3HT$	Poly-3-Hexyl-Thiophene
PA	Photo-induced Absorption
$PCBM$	6-1-(3-(Methoxycarbonyl) (Propyl)-5-1-Phenyl-[6,6]-C_{61}
PCP	Π-Conjugated Polymer
$PEDOT/PSS$	Poly(3,4 ethylenedioxythiophene) Poly (Styrene Sulfonate)

Acronym	Definition
PL	Photo-Luminescence
$PLDMR$	Photo-Luminescence Detected Magnetic Resonance
PPV	Poly (Phenylene Vinylene)
PT	Pentathiol
PV	Photovoltaic
QCM	Quartz crystal microbalance
$RRP3HT$	Regio-Regular Poly-3-Hexyl-Thiophene
SAM	Self Assembled Monolayer
SEC	Semiconductor
SGH	Second harmonic generation
$SLCL$	Space Charged Limited Current
SPR	Surface plasmid resonance spectroscopy
SSM	Solid State Mixture
STM	Scanning Tunneling Microscopy
$TEMPO$	2,2,6,6-Tetramethylpiperidine 1-Oxyl
THF	Tetrahydrofuran
TOF	Time Of Flight
UV	Ultraviolet
$V_{built-in}$	Build in voltage
V_{oc}	Open Voltage Circuit

ACKNOWLEDGEMENTS

I would like to thank Dr. Zeev Valy Vardeny, my advisor, for his inspiration and support. His enthusiasm and optimism in exploring the unknown realm have greatly encouraged me as well as many others in the group. His invaluable insight, experience and great scientific intuition have been the source of inspiration and help during our research. I am so delighted to have spent these years under his mentorship.

I would also like to thank my supervisory committee members, Dr. Vladimir Burtman, Dr. Eugene Mishchenko, Dr. Ajay Nahata, and Dr. Wayne Springer for their inspiriting and encouraging discussions. Their invaluable advices and beneficial guidance is the great wealth I gained here.

My special thanks are also extended to Dr. Mathew Delong, Dr. Randy Polson and Dr. John Viner. They have spent many valuable hours helping me solve technical problems.

I would like to express my deepest gratitude to Dr. Vladimir Burtman, Dr. Cungeng Yang and Dr. Xiaomei Jiang. They instructed me on the lab techniques and underlying physics with great enthusiam and patience.

Other members of our group, Tomer Drori, Joshua Kennedy, Dr. Chuangxiang Sheng, Dr. Minghong Tong, Fujian Wang and Golda Hucik, Sanjeev Singh, Josh Holt, and members of other research groups, Kamdem Thaddee, Dr. Di Wu, have never hesitated to lend me their knowledge and hand. I greatly appreciate their help.

My deepest gratitude also goes to Dr. Eithan Erenfreud, Dr. John Lupton and Dr. Jing Shi. I benefited a lot from their invaluable discussions.

CHAPTER 1

INTRODUCTION

This work dwells on both molecular wires and organic solar cells. We shall introduce these two fields separately. We will present the background and motivation for each of these fields, then introduce the classes of organic solar cells and how to characterize them.

1.1 Background and motivation

1.1.1 Molecular wires

The electrical properties of organic molecules have attracted much attention due to the continuous search for new approaches for further miniaturization of electronic devices. According to Moore's law, the number of transistors on an integrated circuit is doubling every two years [1]. If this trend is to continue, the size of the transistor will soon reach the scale of atoms or molecules. Consequently, the silicon-based technology will suffer because of physical and economic limitations. Molecular electronics is one of the promising technologies which would be an alternative. The concept of molecular electronics is the use of single molecules or arrays, or layers of molecules, for the fabrication of electronic components such as wires, switches, and storage elements. The molecules can be designed and tailor-made by chemical synthesis. Their physical properties are tunable by their structure. In particular, a very small size of the molecules makes them ideal to fabricate a high-density electronic device.

In 1974, Aviram and Ratner proposed that functionalized aromatic molecules could be used as new materials for electronic devices [2]. Over two decades later, the first prototypes of the respective devices have been demonstrated [3, 4, 5]. Reed and co-workers reported on measurements of the conductance of a single molecule [3]. Since then, a whole variety of device types have been proposed. These devices range from mechanical break-junction, electro-migration break junction, nano-pore method, nano-particle bridged junction and a broad range of devices that involve STM or AFM tips as upper electrode.

Experimentally, the challenges of the field are:

- The reproducibility of the device's qualitative and quantitative results. This is due to the fact that the bond of the molecule with electrode depends on a wide range of environmental properties. It has been shown that [6] the molecule depending on its environment could bond to the electrode via more than one gold atom for example.

- The number of molecules in the junction. Many experiments that claimed to have measured the single molecule resistance could only be matched to theoretical work by considering that this molecule is not the only one in the junction. There are many other molecules that might be bonded to at least one electrode and still contribute to the total conductance of the device [7].

- In some of these experiments, it is difficult to verify that the conduction measured is actually that of the molecule attached to both electrodes or to just one of the electrodes [7]. So the connectivity of the molecule to both electrodes is in question.

- The difficulty concerning the type of method used to attach the molecule to the electrode. Some molecules have the ability to form both ionic and covalent bonds with the electrode. In this case it is hard to define the kind of contact (ohmic or not ohmic) with the electrode that is obtained.

Theoretical modeling of these devices also faces some challenges:

- The nature of charge transport through a single molecule and molecular aggregates. Once a molecule is bonded to an electrode, the very nature of the molecule itself could be changed. This is the challenge for the theorist as there is no real knowledge of the system at hand. In addition, if aggregation of the molecules occurs it becomes even more difficult to model the system and take into consideration all properties of single molecules and the bulk properties of the aggregates.

- The nature of the contact is critical for theoretical modeling. As seen for the experimentalist, the nature of the bond with the molecule is of great importance here. Because of the lack of knowledge of the molecule and its environment, the type of barrier present between the molecule and the electrode becomes unknown as well.

- The influence of vibration on the system. Conformational changes in the molecule and the type of link the molecule has with the electrode lattice could determine the nature of the electron-phonon coupling in the system.

- The role of the molecule in the entire transport process. It is hard to decide what kind of transport governs the process: coherence tunneling or thermal hopping.

- How is the metal/molecule barrier affected by an applied electric field?

If these devices must be used as molecular wires, it is imperative to know with certainty what the single molecule resistance is. The ability for the molecules used to self-assemble on the substrate provides another possibility for molecular electronics: dimensional tunability. In two-dimensional (2D) macromolecular systems, an additional "dimension"is formed due to the in-plane charge delocalization in a direction perpendicular to that of the 1D intra molecular transport. Such a situation exists, for example in casted films of regio-regular poly(3-alkyl-thiophene) in which self-assembled lamella are formed perpendicular to the film substrate and in molecular layer epitaxy structures [8, 9]. Other ordered organic molecular systems also show delocalization perpendicular to the principal molecular direction. For example: single wall carbon nanotube sheets, polyacetylene microcrystalline fibers, and even DNA double helix molecules. Currently there is a fragmental insight of charge and energy transport in 2D organics that originates mostly from the fields of π-conjugated polymers and biophysics.

1.1.2 Organic solar cells

Given the detrimental effect of using energy such as coal, oil and uranium, the need for alternative energy has never been so great. Renewable energy sources never run out and have little or no effect on the environment. Renewable energy harnessing technologies include photovoltaic systems, solar thermal applications, wind mills, wind energy electricity generators, micro-hydro power plants, biomass/biogas plants, geothermal, wave and tidal plants, and their associated energy storage components. Photovoltaic electricity generation has the singular advantage of being modular, thus decentralized electricity generation, and systems of different sizes are possible. The conversion of solar radiation into electrical energy by means of solar cells has been developed as a part of satellite and space travel technology.

The theoretical efficiency of solar cells is about 30%, and in practice, efficiencies as high as 25% have been achieved with silicon photovoltaic laboratory devices. Overall system efficiencies are in the range of 10 to 14% [10]. The technology of photovoltaic devices is well developed, but large scale application is hampered by the high price of the cells. The widespread use of solar power has been elusive because it can be difficult and costly to manufacture the commercial photovoltaic cells, which are made of inorganic crystals such as silicon. One possible alternative to circumvent this problem is to develop photovoltaic cells from materials that can be processed as easily as plastics. Organic solar cells have a singular advantage over their inorganic counterparts, in that they are much less expensive to produce.

They do not require the high deposition temperatures or complex processing as required in inorganic devices, and they can be deposited onto large flexible substrates. For example, organic cells (Figure 1.1) might be made in different colors and be flexible enough to use on window blinds, walls, and other materials in buildings. This provides design options that could lower the cost of using the cells. Unfortunately, lagging energy conversion efficiencies have held their application back. The last few years have seen tremendous progress in the application of organic materials for photovoltaic following the success of this class of materials in other electrical, electronic and optoelectrical applications.

1.2 Classes of organic solar cells

1.2.1 Dye-sensitized solar cells

The dye-sensitized solar cell (Figure 1.2)(DSSC) is a real revolution in solar energy 40 years after the invention of silicon solar cells [11, 12]. The working mechanism is based on a photoelectrochemical mechanism, resembling the photosynthesis in plant leaves. The efficiencies of the DSSC are as high as those obtained from amorphous silicon solar cells (10 - 11%) [13]. It was invented in 1991 by Prof Michael Graetzel in Switzerland. As the dye molecules are hit by light, electrons in the dye are transmitted to TiO_2. Then the electrons are collected by the front electrode and supplied to the external load. The dye molecules are then electrically reduced to their initial states by electrons transferred from the redox couple in the electrolyte. The oxidized ions in the electrolyte diffuse to the back electrode to receive electrons.

1.2.2 "Bilayer"solar cells

In the planar hetero-junction, or "bilayer"device [14] , the organic D/A (donor/acceptor) interface separates excitons much more efficiently than an organic/metal interface in the single layer device. The energetic diagram of such a bilayer device is depicted in Figure 1.3(a). Sunlight photons which are absorbed inside the device excite the donor molecule (1), leading to the creation of excitons. However, the acceptor phase can also absorb light, but for simplicity only the photons that are absorbed by the donor phase are considered here. The created excitons start to diffuse (3) within the donor phase and if they encounter the interface with the acceptor then a fast dissociation takes place (4) leading to charge separation [15, 16]. The resulting metastable electron-hole pairs across the D/A interface may still be coulombically bound and an electric field is needed to separate them into free charges [17, 18]. Therefore, at typical operation conditions, the photon-to-free-electron conversion efficiency is not maximal. Subsequently, the separated free electrons (holes) are

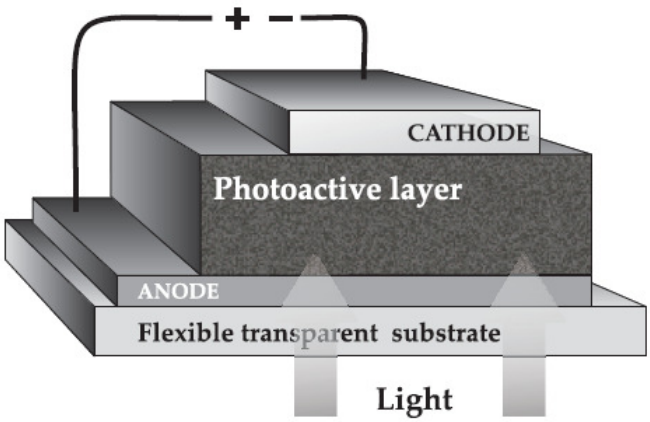

Figure 1.1. Schematic layout of an organic solar cell.

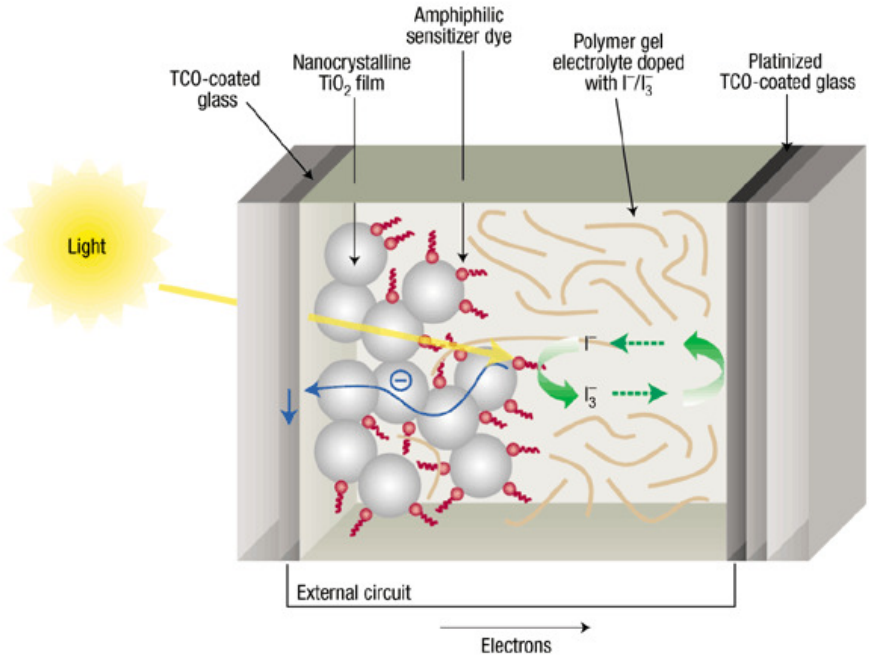

Figure 1.2. Schematic layout of a dye-sensitized cell.

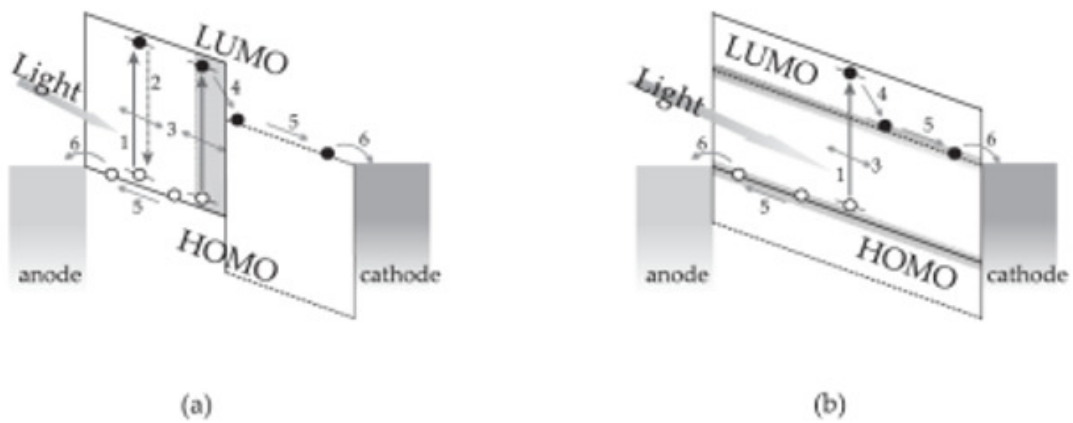

Figure 1.3. Schematic band diagram of a bilayer device (a) and a bulk hetero-junction (b). The numbers refer to the operation processes explained in the text. The dashed line represents the energy levels of the acceptor, while the full lines indicate the energy level of the donor in the solar cell.

transported (5) with the aid of the internal electric field, caused by the use of electrodes with different work functions, towards the cathode (anode) where they are collected by the electrodes (6) and driven into the external circuit. However, the excitons can decay (2), yielding luminescence if they are generated far from the interface. Thus, the excitons should be formed within the diffusion length of the interface. Since the exciton diffusion lengths in organic materials are much shorter than the absorption depth of the film, these limit the width of effective light-harvesting layer.

1.2.3 Bulk hetero-junction solar cells

A revolutionary development in organic solar cells came in the mid-90s [19] with the introduction of the dispersive (or bulk) hetero-junction, where the donor and acceptor material are blended together. If the length scale of the blend is similar to the exciton diffusion length, the exciton decay process (2) is dramatically reduced since in the proximity of every generated exciton there is an interface with an acceptor where fast dissociation takes place (4). Hence, charge generation takes place everywhere in the active layer, as is schematically represented in Figure 1.3(b). Provided that continuous pathways exist in each material from the interface to the respective electrodes, the photon-to-electron conversion efficiency and, hence, the photosensitivity is dramatically increased. The observation of improved device performance using bulk hetero-junctions represents the departure from the device physics of conventional inorganic solar cells and has led to designs of devices and materials. Nowadays, the bulk hetero-junction is the most promising concept for all-organic solar cells.

1.3 Organic solar cell characterization

In order to investigate the photovoltaic performance of a cell, as well as its electric behavior, the current density-voltage (J-V) characteristics in the dark and under illumination are considered. Figure 1.4 shows a typical J-V curve of a solar cell in the dark (dashed line) and under illumination (solid line). When the cell is illuminated, the J-V curve is shifted down by the amount of photocurrent (J_{ph}) generated. The open-circuit voltage, V_{OC}, is the maximum photovoltage that can be generated in the cell and corresponds to the voltage where current under illumination is zero. The maximum current that can run through the cell at zero applied voltage is called the short-circuit current, J_{SC}. The maximum of the obtained electrical power P_{max} is located in the fourth quadrant where the product of current density J and voltage V reached its maximum value ($J_{max} \times V_{max}$); as seen in Figure 1.4. It is also observed from Figure 1.4 that P_{max} is bigger when the J-V curve

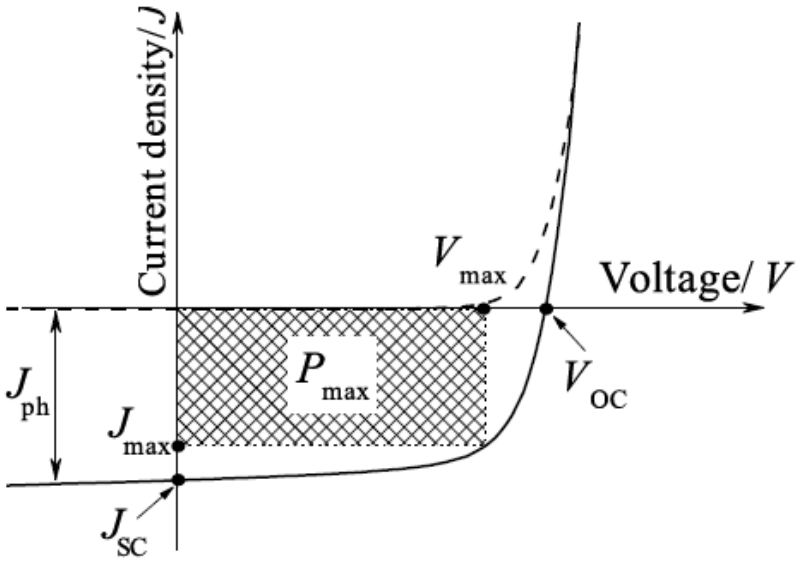

Figure 1.4. Typical J-V characteristics of an organic solar cell in the dark (dashed line) and illumination (solid line) conditions. The short-circuit current density (J_{SC}) and open-circuit voltage (V_{OC}) are shown. The maximum output power (P_{max}) is given by the rectangle $J_{max} \times V_{max}$.

resembles a rectangle with area $J_{max} \times V_{max}$. The ratio between (the rectangle of) P_{max} and the product of (or a rectangle defined by) J_{SC} and V_{OC} measures the quality of the shape of the J-V characteristics, and is defined as the fill factor (FF)

$$FF = \frac{(J.V)_{max}}{J_{SC}V_{OC}} \tag{1.1}$$

Thus $P_{max} = J_{SC} \times V_{OC} \times FF$. The power conversion efficiency η of a solar cell is the ratio between the maximum output power P_{max} and the power of the incident light P_0:

$$\eta = FF\frac{J_{SC}V_{OC}}{P_0} \tag{1.2}$$

Among the parameters that determine the efficiency of the solar cell are the V_{oc} open voltage circuit, the J_{SC} short circuit current and the fill factor FF. In order to improve the device efficiency, it is critical to understand the physics of the device.

1.4 Outline

In molecular electronics, the basic questions regarding the resistance of a single molecule and the transport through a single and an aggregate of molecules remain up for debate. While a lot of insight has been gained over the past decade on the fabrication process of bulk hetero-junction photovoltaic, very little progress has been made towards understanding the underlying physics. In this dissertation we would like to answer questions such as: what is the single molecule resistance? What kind of mechanisms govern the transport through a single molecule as well as an aggregate of conducting molecules? What physical parameters in an organic solar cell fabrication can lead to an enhanced efficiency? What is the origin of the open voltage circuit?

In Chapter 2 of this dissertation we will present all the experimental techniques used. Chapter 3 will show experimental results and discussion on the optical and electrical studies of single molecules as well as aggregate of molecules. We shall also present in Chapter 3 our results regarding what is required at the fabrication stage in order to achieve a high efficiency bulk hetero-junction solar cell. We will also study the origin of the open circuit voltage and its difference from the built-in voltage. In Chapter 4 we will propose a method for increasing the efficiency of bulk hetero-junction solar cells.

CHAPTER 2

EXPERIMENTAL TECHNIQUES

In this chapter, we shall briefly introduce most of the experimental techniques used in this dissertation. We shall present the different experiments performed in the study of single molecule transport in the first part and then proceed to those performed in the study of organic photovoltaic devices.

2.1 Single molecule transport study experiments

First we would like to introduce the self-assembly technique, present our actual device fabrication and then conclude this section with the experiments performed on these devices.

2.1.1 Self-assembled monolayer (SAM) growth

The important elements to consider for SAM preparation are the molecules, substrates, chemistry between the molecule and the substrate, the resulting or desired structure and the kinetics of the growth process.

2.1.1.1 The molecules

The molecules used for SAM growth in this dissertation are part of a group of molecules dubbed alkanethiols and alkanedithiols. Alkanethiols can be described as carbohydrates $[CH_3]_n$ with a thiol$[S-H]$ head group, whereas alkanedithiols are exactly like the latter with the addition of a thiol end group (Figure 2.1).

Generally speaking, molecules used for SAM are made of three essential parts:

- The headgroup; the part of the molecule that has chemical affinity with the substrate, i.e., that can form a bond with the atoms of the substrate. In the case of alkanethiol it would be the thiol part of the molecule.

- The methylene spacer, basically the carbohydrate or alkane part of the molecule.

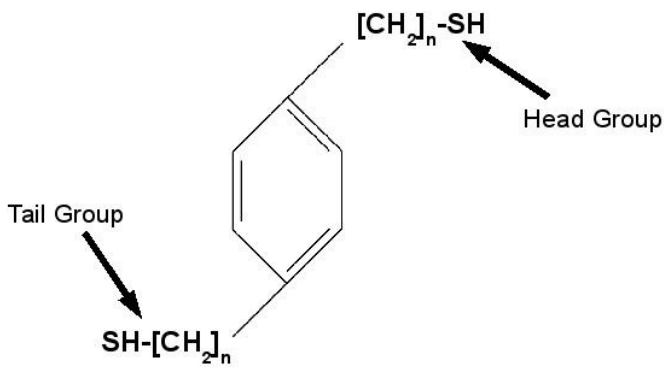

Figure 2.1. Structure of SAM molecule

- The tailgroup which is the end thiol group which has the ability to bond just like the headgroup to any metal that can be evaporated on top of the formed SAM. In the case of alkanethiol, the tailgroup is the last $[CH_3]$ on the methylene spacer.

2.1.1.2 The substrate

The molecules headgroup must be able to form a chemical bond with the substrate. Most metals at ambient temperature have a native oxide layer on their surface. This makes them unsuitable for SAM as breaking the metal-oxygen bond is energetically demanding thus making it difficult to form SAM on these types of substrates. Gold, however, is special because it is stable and inert at ambient conditions; this makes it an ideal candidate for SAM substrate. In addition, it has also been shown that the gold sulfur bond is very stable.

2.1.1.3 SAM growth chemistry

The mechanism for the bond formation between the molecule and substrate is still a subject of debate. It is however widely accepted that the $[S-H]$ bond breaks and is replaced by an $S-Au$ bond. How the $[S-H]$ group gets broken and where the H in $[S-H]$ goes is still unknown.

The simplest unproven model that is accepted regarding the fate of the H in the $[S-H]$ is that of a release of $[H_2]$ during the SAM process such that we have:

$$RSH + Au \rightarrow RSAu + \frac{1}{2}H_2 \tag{2.1}$$

From Karpovich et al. the energetics of this process lead to an overall free energy $\Delta G_{ads} \approx -5.5 kcal/mol$. Using the enthalpy of adsorption for alkanethiol on gold $\Delta H_{ads} \approx 20 kcal/mol$ and using the formulae:

$$\Delta G_{ads} = \Delta H_{ads} - T\Delta S_{ads} \tag{2.2}$$

at room temperature we derive an entropy ΔS_{ads} of $-48calmol^{-1}T^{-1}$. This relatively large magnitude and negative entropy value implies a great degree of ordering as the molecules arrange themselves on the substrate, thus justifying how we get a $2D$ crystalline-like lattice on the substrate.

2.1.1.4 The structure of SAM

Using the Low Energy Atomic Diffraction (LEAD) method, Chidsey et al. [20]. established that the SAM molecules are close packed in a hexagonal arrangement that exhibits a $(\sqrt{3} \bullet \sqrt{3})R30°$ registry with the underlying $Au(111)$ surface. This corresponds to a lattice spacing of $5\mathring{A}$. This implies that the molecules headgroup sit in the three-fold hollow sites of the $Au(111)$ lattice.

Additional experiments by Ulman [21] in 1998 and Schreiber in 2000 [22] revealed the existence of a $C(4 \times 2)$ superlattice of the $(\sqrt{3} \bullet \sqrt{3})R30°$ overlayer structure. This superlattice comes from the presence of distinct orientation of the alkyl chains within the unit cell. These studies also show that the alkyl chains are trans-extended and tilted $30°$ from the normal to the surface, to maintain a stabilizing interchain Van Der Waals distance of $4.2\mathring{A}$

2.1.1.5 SAM growth kinetics

SAM growth kinetics has been the subject of many study groups among which we mention the work of Bain et al. [23]. (1989), Karpovich et al. [21]. (1998) and Shreiber et al. [22]. (2000). All of these studies tend to agree on one thing: SAM growth is in two phases. One phase called "the fast regime" that take takes place for a few seconds to a few minutes and leads to 80 to 90% of the total film formation. This is followed by a "slow regime" ranging from minutes to several hours during which the contact angle and thickness reach their optimum values.

2.1.1.5.1 Kinetics of the fast regime. Most studies done to understand this regime are carried out in situ due to the fact that even though the film is almost completely formed, it is still undergoing changes and stopping the process might actually cause harm to what has already grown. Tools such as Surface plasmid resonance spectroscopy (SPR), Quartz crystal microbalance (QCM) and Second harmonic generation (SGH) are used to probe the samples at this stage. Results of the kinetics are then fitted using models that have been developed previously or in case no model fits the results new models developed. The earliest and simplest model proposed to explain this slow process is the Langmuir adsorption model [24]. This model states that:

$$\theta = 1 - exp(-cK_L t) \tag{2.3}$$

where θ is the fraction of available adsorption sites, K_L is the growth rate and c is the solution concentration. However, this model has been subject to a lot of revisions, as it does not quite fit experimental results. This is essentially due to the fact that some thiol groups can impinge to islands of thiols that are already chemisorpbed onto the surface and will have to either incorporate the island or just desorbs. This assumption has led to the development of the following equation:

$$\frac{d\theta}{dt} = cK_L(1-\theta)(1+K_E\theta) \tag{2.4}$$

with K_E representing the adsorption rate on island of already adsorbed thiols. Thus:

$$\theta = \frac{exp[(1+K_E)cK_L t - 1]}{exp[(1+K_E)cK_L t - K_E]} \tag{2.5}$$

This model is also called the "modified Langmuir model" [25]. Chronologically, in this fast phase, first the thiol molecules are adsorbed onto the gold surface with their alkyl chain lying parallel to the surface. Then a transition phase occurs where the alkyl chains stand up perpendicularly to the surface and form islands of thiolate. These islands then continue to grow by incorporation of other thiol moieties thereby forming larger domains.

2.1.1.5.2 Kinetics of the slow regime. Himmelhaus et al. in 2000 [26] studied this regime by IR-visible sum frequency spectroscopy, which allowed them to follow the conformational ordering of the $C-H$ stretching modes as a function of time. They were able to identify the fast regime and noted that in this regime the alkyl chains had a large number of gauche defects. In the slow regime, the alkyl chains get ordered at a rate that is four times slower than in the fast regime. In this slow regime, the film thickness grows due to the change in conformation of the alkyl chains from kinky to trans-extended. After this occurs the reorientation of the terminal group at a pace that is 35 times slower than the conformation rate.

2.1.2 Device fabrication

We shall chronologically describe how the devices were fabricated. The entire fabrication process has been summarized schematically in Figure 2.2.

2.1.2.1 Substrate preparation

We started with a silicon wafer coated with silicon dioxide. The wafer was cut in such a way that it could fit on the shadow mask that was going to be used for evaporation. After cutting, the substrates were then cleaned first with acetone, then with isopropyl

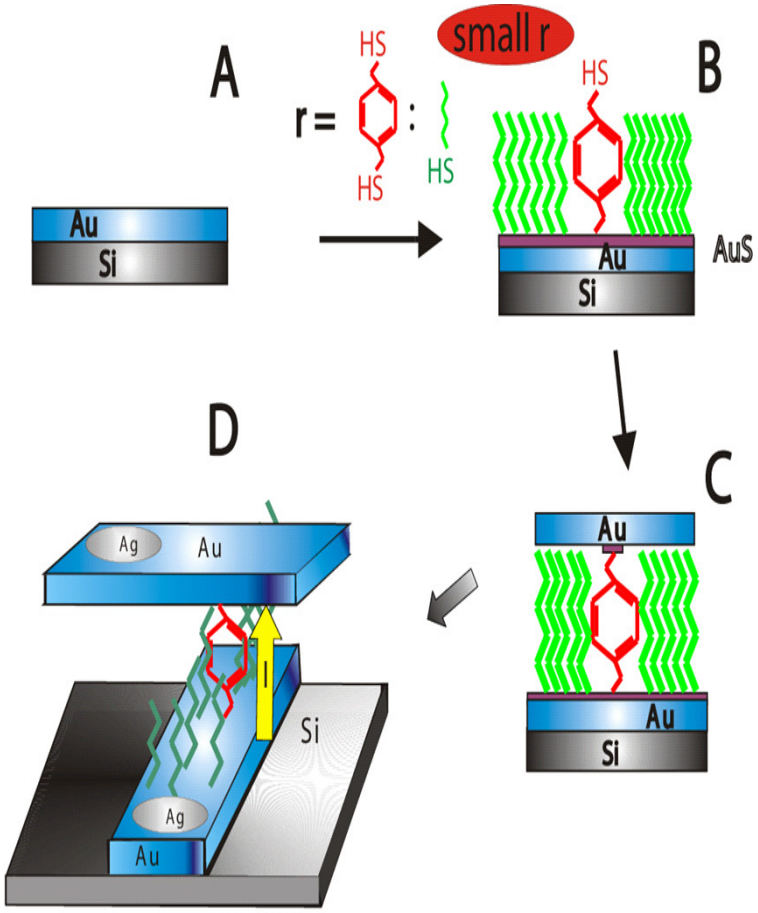

Figure 2.2. The fabrication process (schematic) of SAM SSM diodes at small ratio r of molecular wire (Me-BDT in red) to molecular insulator (PT in green). A: evaporation of an Au base electrode; B: SAM growth of the appropriate molecule mixture on the bottom Au film; C: evaporation of the upper Au electrode; D: I-V measurement set-up, where the contacts are made using silver paint.

alcohol. Following the cleaning process, the substrates are dried with "dry air" and kept in a desiccator prior to usage.

As mentioned above, the substrates used are cut to the size of a shadow mask that is used for evaporation. The metals used as electrodes in this study are gold, aluminium and cobalt. For our devices, the electrodes are evaporated in a cross pattern. So the bottom electrode is first evaporated in one direction and then for the upper electrode, the substrate is placed on the shadow mask in such a way that the upper electrode is perpendicular to the bottom.

The evaporation is done using a DV-SJ/20C Denton Vacuum e-gun. First the e-gun chamber is mechanically pumped until the pressure is below a certain value which is around $20mtorr$. Once that value is reached, the Turbo pump is switched on automatically. For aluminium evaporation, the electron beam is started once the pressure is below $3.10^{-6}mtorr$. In the case of gold or cobalt, we usually wait until the pressure is around $1.10^{-7}mtorr$. During evaporation, the substrate is kept at $65^{0}C$ and the evaporated thickness is usually around 20 to $30nm$ for both the upper and the bottom electrodes.

2.1.2.2 Self-assembling process

First our samples (substrate with metal on top) plus a stir bar placed on a glassy sample holder are inserted into the shlenk line which is lying on a stirring and heating plate; then the shlenk line (Figure 2.3) is pumped both by a mechanical pump then by a diffusion pump which are both attached to the shlenk line. After a high vacuum is obtained, the shlenk line is then filled with argon and pumped again to high vacuum. This is done three times to ensure all traces of oxygen and water vapor are removed from the system. At the end of this stage, the shlenk line is pressurized with argon. At this point, using a syringe, the solution (toluene + molecule) is introduced into the shlenk line via a rubber cap placed at one of the inlets of the shlenk line. After this, the rubber cap is removed and replaced by a glassy cap that is tightened to insure no inward flow of oxygen. To start the process, the stirring plate is turned on so the solution is stirred during the entire self-assembling process. The system is left for 24 hours for the self-assembling to take place.

After 24 hours, the stirring plate is turned off, using a syringe, the solution is extracted from the shlenk line, and the samples are rinsed three times under argon with distilled toluene. The samples are then removed from the shlenk line and placed in a vacuum oven for 1 hour. For storage, we use a desiccator or the samples are immediately taken to the evaporator for top electrode evaporation.

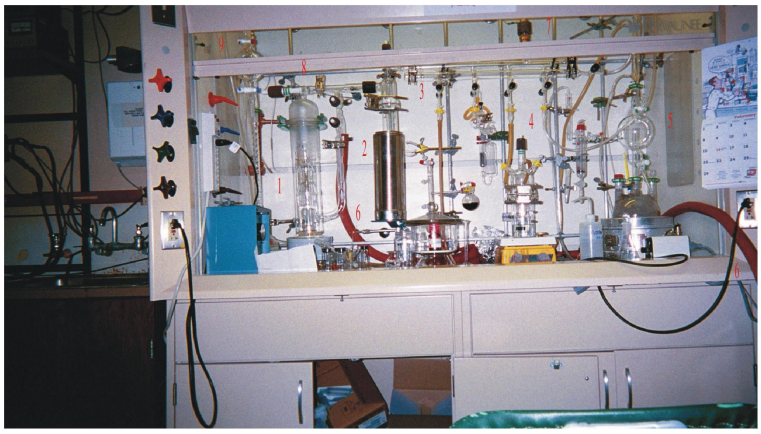

Figure 2.3. The home-made high vacuum based Shlenk line and reactive vessel. The Shlenk line consists of 9 stages: glass diffusion pump (1); LN2 trap (2); vacuum and Ar gas line (3); reactive vessel (4); distillation toluene system (5); rough pump line (6); high vacuum gauge (7); low pressure gauge (8); and distillation PT system (9). The reactive vessel (4) has connection to the Shlenk line through a vacuum tube. The two input ports are for: (a) washing the reactive vessel by vapor of distilled toluene that is delivered through the supply line, and (b) input/output of the reactive precursors in solution form and (c) washing excess reagents from the reactive vessel.

2.1.3 Device characterization

2.1.3.1 (I-V)characteristics measurements

There are essentially two ways of obtaining the current-voltage characteristics of a device. One can use a two-probe system or a four-probe system, as shown in Figure 2.4(a). The essential difference between these two measuring methods is that in the four-probe system, one gets rid of the contact resistance. So in systems where the contact resistance is of any concern, in order to obtain an accurate current-voltage characteristic of the device itself, a four-probe system is the one to use; otherwise a two-probe can also be used.

Another issue that one must be careful with in current-voltage characteristics measurements is the leads resistance. In case our device resistance is smaller or comparable to the leads resistance then these resistances must be accounted for. Fortunately in most of our measurements we used BNC cables for which the resistance does not exceed $50 Ohm$s and our devices' resistances are in general very high compared to this.

In this work, we measured the IV-characteristics at various temperatures using a cryostat to which is attached a Lakeshore temperature controller which helps in reading and setting the temperature. A heater is also attached to the temperature controller such that temperature can be ramped in both directions.

Also attached to the cryostat, is a Keithley 236 that is used for both voltage supply and current measurement. The Keithley is attached via a GPIB card to a computer on which a labview program is used for the IV measurements. For the systems that we have studied in this work, namely, devices made with polymers or molecules, we expect to measure a nonlinear current-voltage characteristic.

The polymer or the molecule can be considered in the first approximation as an insulator. This approximation comes from the relative low mobility of carriers in these systems. So a device made of the polymer or a molecule between two electrodes can be viewed as a Metal insulator metal system (MIM). This configuration has been extensively studied in the literature. The transport is essentially by tunneling so we expect a rectification behavior in the current-voltage characteristics of these systems. As shown in Figure 2.4(b) whether we are studying a single molecule device or an organic solar cell, the transport is essentially nonohmic, i.e., nonlinear as expected.

2.1.3.2 Conductance vs. voltage

From the current-voltage characteristics (example given in Figure 2.5), we can obtain the conductance vs voltage. In a single molecule system, the conductance vs. voltage may provide the value of the conductivity gap. In a metal-molecule-metal system, the transport

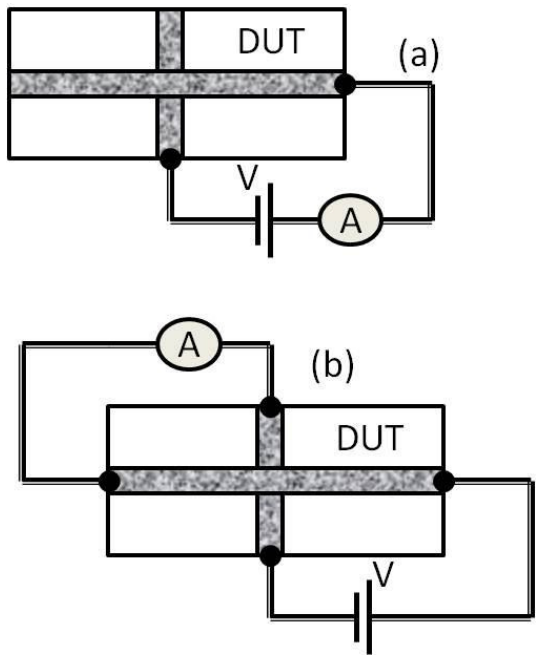

Figure 2.4. I-V device characteristic measurement configurations (a) Two probes and (b) four probes.

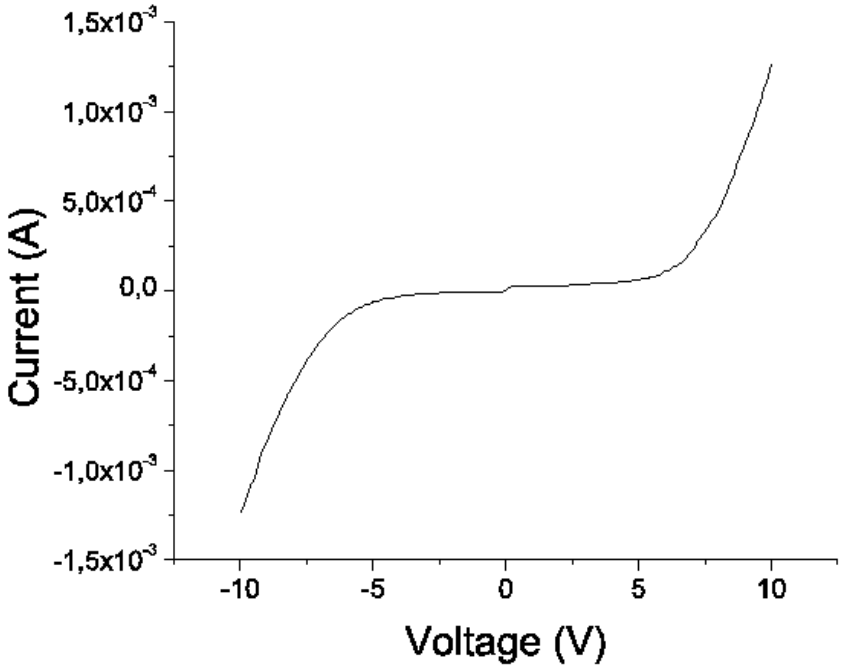

Figure 2.5. Example of I-V characteristic obtained from characterization of a SAM device at 150K.

type is basically resonance tunneling; namely, when the Fermi level is aligned with a state in the molecule energy gap, an increase in the current is registered; otherwise, it is just a tunneling current that is observed. So as the voltage is ramped, one basically scans the energy states of the molecule. Therefore from the conductance vs. voltage response, one can obtain the energy interval between the metal's Fermi level and the different energy states that are encountered as the voltage is scanned. The conductivity gap can also provide us with the position of the metal's Fermi level with respect to the HOMO-LUMO gap. This is one of the major issues that one faces when trying to model these systems.

2.2 Organic photovoltaic device fabrication and characterization

2.2.1 Sample preparation

The photophysics of PCPs is determined by intrachain and interchain interactions. Because interchain interaction is greatly affected by sample preparation and solvent used, it is thus necessary to understand how the sample characteristic behavior changes under different preparation conditions, such as solvent used, annealing procedures, etc. In this section we will summarize the main processes necessary in getting photovoltaic cells with large power conversion efficiency.

2.2.1.1 Polymer and molecules used

The active layer in bulk hetero-junction solar cells (BOPV) is a blend of an acceptor molecule and a donor polymer.

2.2.1.1.1 PCBM. PCBM (Figure 2.6), also known as 6-1-(3-(methoxycarbonyl) (propyl)-5-1-phenyl-[6,6]-C61, is used as the acceptor molecule. It is capable of accepting up to 6 electrons; this makes it one of the best acceptor molecules presently on the market. PCBM is a soluble version of C_{60} and this is made possible by the addition of methyl-esther group to C_{60}. Another reason for the wide use of this molecule in OPV is its high electron mobility. Field effect mobility of evaporated C_{60} was reported [27] to be $8.10^{-5}m^2/V.S$; C_{60} single crystal grown from vapor phase revealed a time of flight mobility of $5.10^{-5}m^2/V.S$ [28]. PCBM hole mobility was reported by Mahailetchi et al. [29] to be only $2.10^{-7}m^2/V.S$; much less than the electron mobility; they also determined the HOMO and LUMO of PCBM to be, respectively, $6.1eV$ and $3.7eV$.

2.2.1.1.2 Regio regular poly(3-hexylthiophene) (RRP3HT). Following its first synthesis in 1993 [30], RRP3HT (Figure 2.7) has attracted a lot of interest for application in solar cell and field effect transistors. This interest is attributed to its enhanced hole mobility

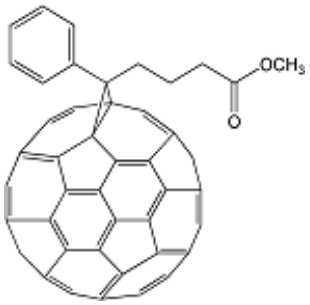

Figure 2.6. Molecular structure of PCBM.

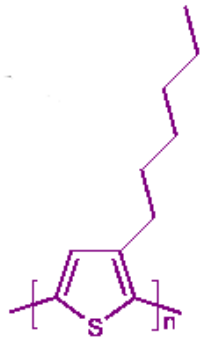

Figure 2.7. Molecular structure of P3HT.

and its extended light absorption (up to 600 nm). RRP3HT chains arrange themselves into lamellae oriented perpendicular to the substrate [31]. The higher the regio regularity the closer the lamellae and consequently the higher the interchain interaction. This can be observed through optical [31] or electrical excitations. The interchain interactions are responsible for the distinct shoulder in the absorption spectrum observed at long-wavelength, as well as the large field effect mobility. In this work, we used other polythiophene polymers different from the above mentioned by the length side group. We also used some PPV derivatives such as MEHPPV and MDMOPPV polymers.

2.2.1.1.3 PEDOT:PSS. In order to prevent electrons from being collected by the anode ITO and thereby causing recombination at the interface with the active layer, it is recommended to have an electron blocking layer. This layer should also allow a smooth collection and transport of hole to the ITO electrode. The best candidate for this is Poly (3,4ethylenedioxythiophene) poly (styrene sulfonate) (PEDOT:PSS) (Figure 2.8), which is a mixture of sodium polystyrene sulfonate which is a sulfonated polystyrene and poly(3 ,4ethylenedioxythiophene) or PEDOT which is a conjugated polymer based on polythiophene. Together, these two polymers form one of the best hole conducting polymers that is commercially available. It is commercialized by H.C Stark and comes in two forms. The first is highly diluted, has a low conductivity and is suitable for OLEDs while the other is less diluted, highly conductive and is suitable for OPVs.

2.2.1.1.4 The solvent effect. The commonly used solvents for preparing spin casted PCPs films are toluene, THF, chloroform, chlorobenzene and ortho-dichlorobezene. The polarity of the organic solvents, the interaction between the solvents and PCP chains, and the vaporization speed of the solvents all have strong effects on the film nanomorphology, and consequently also affect the photophysical properties of the organic active layer. For strongly aggregated PCPs, highly vaporized solvents such as THF and chloroform are best for getting a neat film. Thus slowly vaporized toluene is usually selected for spin-cast films for OPV. PCP films made from toluene solution have more aggregate properties, which manifest themselves in red shifted PL band, and stronger polaron PA, compared to that casted from chloroform solutions.

2.2.1.1.5 The spin coating process. Spin coating is used to form thin, uniform films for the OPV devices. The thickness of the uniform films can be measured with a profile-meter such as Tancor P-10 at the HEDCO lab or by AFM. Spin coating reduces the interchain congregation during the solvent evaporating process, and therefore reduces the intensity of the optical effect caused by interchain interaction. For example, polaron

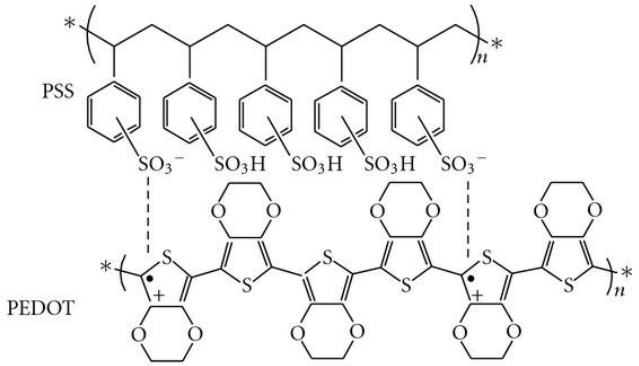

Figure 2.8. Molecular structure of PEDOT:PSS.

generation is strongly dependent on interchain interaction; therefore the polaron PA band will be reduced in a spin-coated film compared to a drop-casted film.

2.2.1.1.6 The drop casting process. Drop casting is used to make thick films when the solution is dilute and strict film quality is not required. Drop casting increases the interchain interaction and aggregate formation.

2.2.1.1.7 The annealing process. Annealing of the deposited films is done in inert gas at elevated temperatures, and is used to eliminate the used solvent, water, and other evaporated unintentional dopants. Sometimes annealing is also used to reconstruct the film nanomorphology, because at elevated temperature, PCP chains can realign and form new phases. Most commonly, annealing enhances the interchain interaction and this increases the charged polaron photogeneration.

2.2.1.2 The fabrication process of bulk heterojunction OPV

The fabrication process involves the steps listed and explained below. These steps must be carefully followed in order to garranty the device functionality and reproducibility.

2.2.1.2.1 Substrate selection. One side of the OPV cell must be transparent in order to be able to illuminate the device. Transparent and conductive Indium Tin Oxide (ITO) is most commonly used; usually glass coated with ITO is used. Surface roughness, which is defined as peak-to-peak height, has profound influence on carrier injection and consequently also on the device performance. When very thin film devices are fabricated, polished ITO substrates are preferred over unpolished ones. The ITO substrates are bought from Delta Technologies LTD. The substrates are patterned in the following way: first the part of the substrate where we want to use ITO as an electrode is covered with nail polish, which is known to be passive to HCL. After that, the substrates are etched by dipping the substrate in a 2% solution of HCL for 10 minutes. The pattern substrates are depicted schematically in Figure 2.9(a). With this pattern of the substrate, we cut the substrate to the desired dimensions as in Figure 2.9(b).

2.2.1.2.2 Substrate cleaning. Acetone, micro soap, deionized water, and methanol were all used consecutively in supersonic baths for more than 20 minutes each to remove organic and inorganic dirt on the substrate. Finally the substrate is blow-dried with nitrogen gas.

2.2.1.2.3 Plasma cleaning. Plasma cleaning completes the cleaning process by removing any residual organic impurities from the substrates. It is widely believed that oxygen ions react with ITO surface inert compounds and increase the hole injection efficiency of the

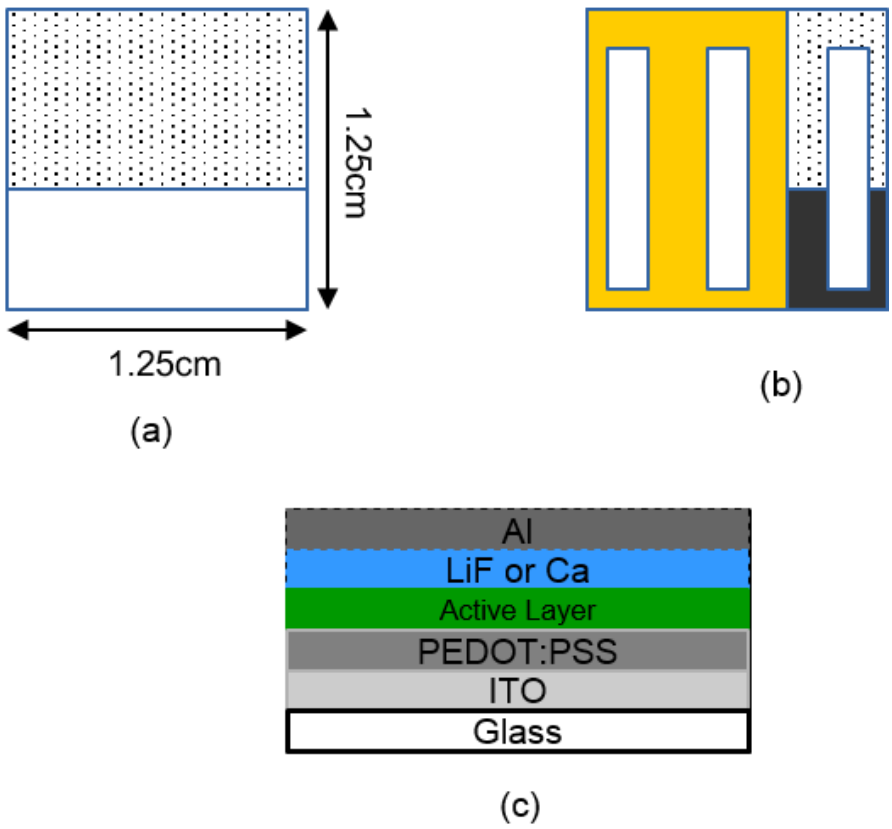

Figure 2.9. Pattern on the substrate after ITO etching: the grey pattern represents ITO (a), the device top view after all steps: white strips represent Al, yellow represents the spin-coated active layer and the black area represents the glass while the pattern represents ITO (b) and cross section view of the completed device (c).

anode. The plasma cleaning is done for not more than 10 minutes. Cleaning for a longer time can alter the ITO conductivity.

2.2.1.2.4 Hole transport layer. A PEDOT/PSS 70:30 composite water solution from Bayer was used as the hole transport layer (HTL). This layer not only smooths the rough ITO surface, but also has a profound effect on adjusting the hole transport. PEDOT:PSS is spin coated onto the substrate at 3500 rpm on a home made spin-coater. This gives a film thickness of about 50 -100 nm.

2.2.1.2.5 Substrate baking. After spin-coating the HTL, the substrate is baked at ambient, in vacuum or in nitrogen at 120 °C for 1 hour for dehydration. Water can greatly lower the performance and life time of a device.

2.2.1.2.6 Coating of PCP active layer. The samples are introduced in a glove box with oxygen level <10ppm where the rest of the device fabrication is made. PCP is the active layer of the OPV. The layer is spin-coated at a thickness of about 80-120 nm. Toluene, chlorobenzene and OCDB are usually selected as the PCP solution. The choice of the solvent is specific to the PCP used as some PCPs have better solubility in some particular solvents. Also the film nanomorphology is greatly determined by the solvent used as can be seen from [32].

2.2.1.2.7 Electron transport layer. After the substrate is degassed, in case we want an ohmic contact between the active layer and the electron transport layer (ETL), we use a low work-function metal such as calcium, and lithium fluoride. The thickness of this layer is generally around 7 to 13nm. It has been shown in [33] that a LiF layer, when evaporated prior to the Al layer, lowers its work function and thus induces ohmic contact with the active layer.

2.2.1.2.8 Aluminum protection. An aluminum overlayer is thereafter evaporated on top of the ETL metal, and serves as both cathode layer and protection layer against outer layer penetration. The thickness of this layer is usually of several hundred nanometers. We also found that this thickness is sufficient to give large reflectivity, and this helps the absorption process in the active layer.

2.2.1.2.9 Encapsulation. UV cured glue is commonly used as a protection layer against device surface friction, water and oxygen penetration. Encapsulation can significantly increase the lifetime of the OPV device when working at ambient or vacuum atmosphere at room temperature. For measurement at low temperatures, however, the device may be destroyed due to the thermal expansion coefficient difference between the UV cured glue and the glass substrate. Therefore, for low temperature measurements

encapsulation is not needed, but instead inert gas flow is required to minimize oxidization of the electrode.

2.2.2 OPV characterization

Once an OPV device is ready there are certain measurements that are needed in order to determine the performance of the device for energy conversion: how well the device absorbs the available photon flux in solar spectrum and transforms it into electrical power. In this section we describe some of the experiments that are conducted in order to achieve this characterization.

2.2.2.1 I-V characterization in the dark

Measurement of I-V characteristics in the dark is done using a two-probe measurement system. All light sources in the room are turned off and the sample is attached to a comb like clip. The clip is then connected to a Keithley 236. The measurement setup is computer interfaced with a labview program from which the I-V is obtained.

2.2.2.2 I-V characterization under illumination

In order to simulate sunlight, a xenon incandescent lamp (Oriel) is used as the light source. The light beam is then sent to an Oriel air mass filter that simulates air mass 1.5 global. To calibrate the light source, a silicon diode was bought from Hamamatsu and sent to NREL for calibration. The calibration data received from NREL contain the value of the short circuit current I_{sc} 100 mW/cm2 and also the deviation from linearity of Isc with respect to the illumination intensity. With this information in hand, we were able to calibrate our optical setup. We thus set the illumination to$100mW/cm_2$ that was impinging on our sample while the I-V characteristic is measured. Figure 2.10(a) shows the measurement setup, while Figure 2.11 shows a typical I-V characteristic under illumination. With the obtained I-V characteristic, we calculate the external efficiency $\nu\eta$ according the following formulae:

$$\eta = FF\frac{I_{SC}V_{OC}}{P_0} \tag{2.6}$$

where $I_{sc}(A/cm^2)$ is the short circuit current, $V_{OC}(V)$ is the open circuit voltage and $P_0(W/cm^2)$ is the input illumination power. FF is dubbed the fill factor and is given by:

$$FF = \frac{(I.V)_{max}}{I_{SC}V_{OC}} \tag{2.7}$$

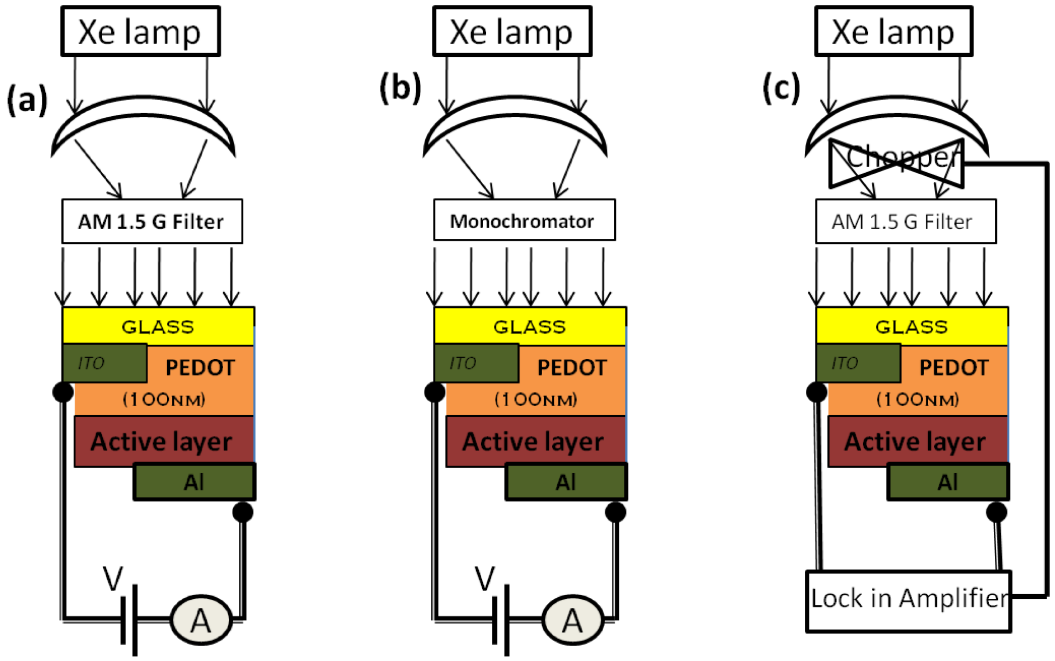

Figure 2.10. OPV I-V measurement setup (a), Monochromatic I-V measurement (b) and IPCE measurement setup (c).

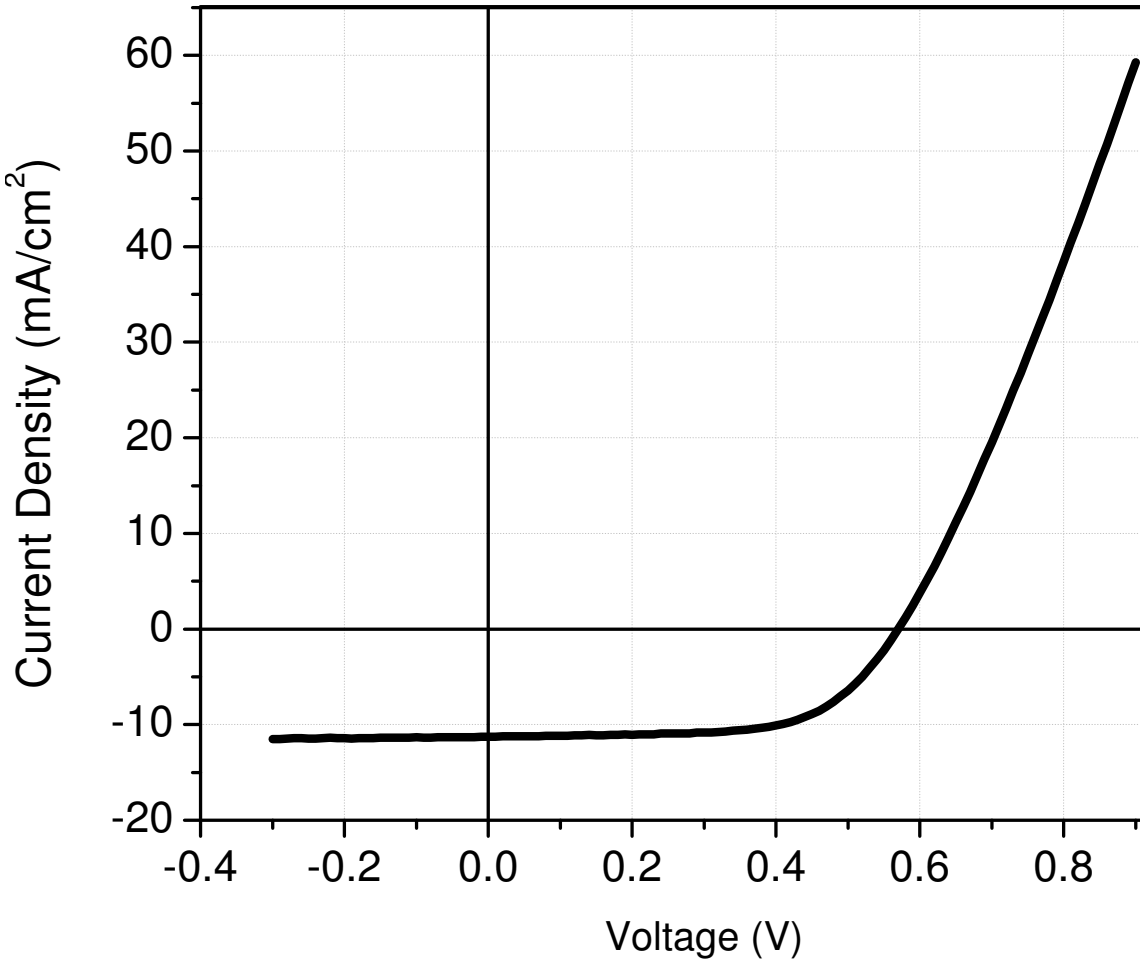

Figure 2.11. Example of OPV I-V under AM 1.5 illumination

2.2.2.3 Monochromatic I-V characterization

I-V characterization under monochromatic illumination is done the same way as in the previous section. The only difference is that here we do not use the AM 1.5 filter since the illumination is monochromatic. Instead, we either add a monochromator which helps in the selection of the desired wavelength or we use a laser beam. In either case, we determine the illumination power with a power meter that has a calibrated silicon photo-diode. We correct the value obtained from the power meter by the responsivity of the silicon photodiode. Figure 2.10(b) represents the setup for this type of measurement.

2.2.2.4 Photocurrent action spectrum or incident photons to collected electrons (IPCE) efficiency

The photocurrent action spectrum is basically the current generated at each wavelength, normalized to the absorbed or impinging power. The setup used for this measurement is represented by Figure 2.10(c). The source here is the xenon lamp incandescent light, where the monochromator is used to select the wavelength. The beam coming from the monochromator is amplitude modulated and sent to the sample, which is hooked to a lock-in amplifier that is frequency and phase locked. The lock-in amplifier can be used in the current mode or in the voltage mode. In case it is used in the voltage mode, a $1K\Omega$ resistor is attached between the sample's electrodes. To get the normalized photocurrent, it is important to measure the input spectrum. This is done using a silicon photodiode as a detector. So in lieu of our sample, the silicon detector is placed and connected to a preamplifier and then to the lock-in amplifier in the same way as our OPV device. The measurements obtained with the silicon detector are corrected with its reponsivity. Thus the normalized photocurrent is derived following the equation:

$$IPCE(\lambda)(\%) = \frac{1240I(\lambda)}{\lambda P_{input}(\lambda)} \tag{2.8}$$

2.2.3 Optical measurement

2.2.3.1 Absorption measurements using the Cary17 monochromator

For the purpose of determining the optical density of our samples and devices, absorption measurements have been used intensively in this work. Depending on the range of interest, we used a commercial spectrometer CARY17 from Olig Co. which probes the optical absorption from 200nm to 2400nm. For infrared and far infrared spectral ranges, an FTIR spectrometer was used. In case the sample structure or device structure is capped by a layer of metal, the optical absorption of the films was measured by reflectivity, for a

semiconductor's electrons in the valence band absorb light and consequently are promoted to a higher energy level. The absorption spectrum, $\alpha(\omega)$ in general gives information about the electron occupied energy levels and the corresponding absorption strengths. The material compound, molecular structure, and dynamics of electronic excited states, can be generally revealed from $\alpha(\omega)$.

Absorption can readily be measured by available commercial spectrometers, such as CARY17 from Olig Co., the one we used in this work. First of all, background transmittance, T_0, which includes the substrate's absorption and the system's response, is measured as a function of wavelength λ. Subsequently, the substrate is replaced by a sample deposited on the same substrate and the transmittance, T_1, through the sample is measured again. The absorbance, A, is then calculated as following,

$$A = \log\left(T_0/T_1\right) \tag{2.9}$$

The absorbance is proportional to the thickness d of the sample (film), and the absorption coefficient α via the relation $A = \alpha d \log(e)$ using

$$T_1 = T_0 \exp(-\alpha d) \tag{2.10}$$

The obtained absorption constant uncertainty is limited by the sensitivity of the spectrometer and the sample film/solution quantity. If the sample consists of a limited few layers of atoms, the traditional measurement will not work. The use of a phase sensitive detection scheme may increase the sensitivity up to 10^{-3}. Thus temperature variation induced absorption changes can be readily measured as in the case of polyacetylene thick films.

2.2.3.2 Photoinduced absorption frequency dependence

Photoinduced absorption (PA) studies the absorption change caused by long-lived photoexcitations that are generated by light absorption. The PA is primarily limited to the subgap energy region because the spectral range that corresponds to the inter-band $\pi - \pi^*$ absorption is prone to various artifacts such as electro-absorption, thermal absorption created by the laser, etc. Also, the subgap states are usually long lived, having a relatively large optical cross section thus, making the measurement relatively straightforward.

The experimental setup for the PA measurements is shown in Figure 2.12. Two light beams are needed for the PA experiments. One beam, usually a CW laser, is used to excite the material, whereas the other beam, usually a continuous light beam from an incandescent

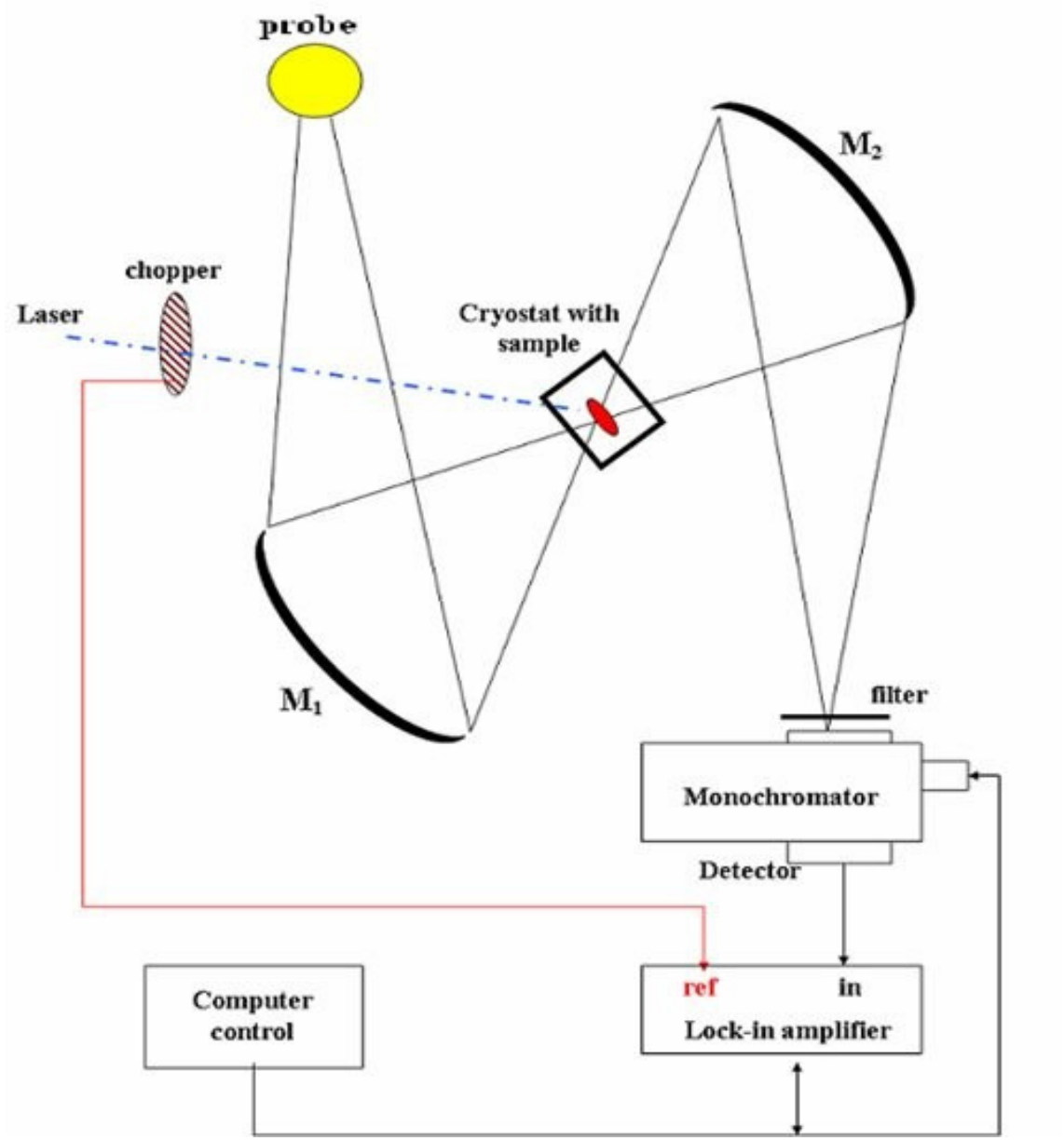

Figure 2.12. CW PA and PL setup.

light source, from a halogen tungsten lamp or an infrared glowbar lamp, is used to probe the absorption characteristic of the long-lived excited subgap states.

As shown in Figure 2.12, the transmitted light is spectrally resolved by a monochro-meter and detected by Si, Ge, InSb or MCT detectors with a corresponding preamplifier, long-pass filter and grating set depending on the wavelength probed. The amplified signal is then fed into a lock-in amplifier together with the phase reference of the modulated laser beam. The change of transmittance ($\Delta T/T$) is obtained using phase-sensitive technique.

$$\frac{\Delta T}{T} = (T_{pumpon} - T_{pumpoff}) \tag{2.11}$$

To obtain the frequency dependence, the modulation frequency is changed from 100 HZ to 100KHZ. To cover this range of frequency, an acoustic modulation is used. This measurement permits us to obtain the recombination time of the excitons in the sample. In the actual measurement, ΔT also depends on PCP system response via the steady state density of the photoexcitations, because N_{Ex} is a dynamic function of the generation and recombination rates. For example a monomolecular recombination kinetics has the following rate equation,

$$\frac{dN(t)}{dt} = G(1 + cos(\omega_0 t)) - \frac{N(t)}{\tau_{eff}} \tag{2.12}$$

The solution to this equation is given by

$$N = \frac{G(1+K)\tau_{eff}}{1 + i\omega\tau_{eff}} \tag{2.13}$$

where

$$K = \sqrt{2\pi}\frac{\delta(\omega - \omega_0) + \delta(\omega + \omega_0)}{2} \tag{2.14}$$

The in phase and the quadrature components of equation 2.13 can be written as follows:

$$N_{inphase} = \frac{G\tau_{eff}(1+K)}{1 + \omega^2\tau_{eff}^2} \tag{2.15}$$

$$N_{outphase} = G\tau_{eff}(1+K)\frac{\omega\tau_{eff}}{1 + \omega^2\tau_{eff}^2} \tag{2.16}$$

It is obvious that the crossing point of the in phase and the quadrature is at $\omega = \frac{1}{\tau}$ (Figure 2.13).

2.2.4 Admittance spectroscopy

Admittance spectroscopy is a tool commonly used to determine the dielectric relaxation of material [34]. Recently, Marten et al. [35] discovered that this tool can actually be used to measure carrier mobility. Traditionally, tools such as Time of Flight [TOF] [36],

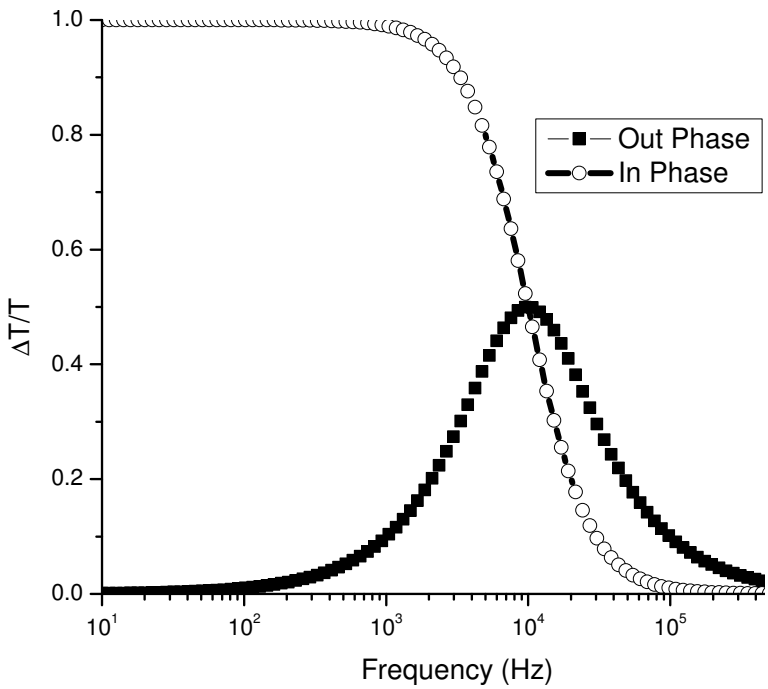

Figure 2.13. Simulation of frequency dependent photoinduced absorption with a $\tau_{eff} = 1ms$.

temperature dependent I-V characteristic [29] and Field effect transistor [37] have been used for carrier mobility measurement. However, each of these measurements presents some obstacles that are not easy to overcome. The TOF method requires a micron or several microns thick sample; this means that the samples are not trap free. Hence there is a chance of having impurity that can affect carrier mobility. Measuring mobility by monitoring the temperature dependence of the I-V is an indirect method that requires a perfect knowledge of the transport mechanism in the device [36]. Lastly, the field effect measurement is an excellent method to extract carrier mobility, but as we know, it requires the active layer to be several microns or hundreds of microns wide, which presents the same disadvantage as the Time flight method. In addition there is also a geometrical issue involved. For example materials such as P3HT do not have an isotropic mobility. Thus in a field effect configuration, the obtained mobility is that for transport parallel to the substrate, while in a solar cell we desire the mobility in the direction perpendicular to the substrate.

In the admittance spectroscopy method, we apply to the device, an AC voltage as well as a DC voltage while measuring the capacitance as a function of the AC voltage's frequency. With this method one can obtain the transit time of carriers, i.e., the time it takes a carrier to go from the active layer to the electrode. It is obvious that all other characteristic times such as the time constant of the circuit must be much longer than the transit time which is related to the carrier's mobility. Generally, the impedance of a device is given by:

$$Z(\omega) = \frac{I_{AC}}{V_{AC}} = \frac{1}{R_s} + i\omega C_p \tag{2.17}$$

where I_{AC}, V_{AC}, R_s and C_p are, respectively, the AC current going through the device, the AC voltage applied to the device, the resistance of the device and the capacitance of the device. The last two are respectively the inverse of the real part of the impedance $Z(\omega$ and the imaginary part of the impedance. The inverse of the impedance $\frac{1}{Z(\omega)}$ is called the admittance.

2.2.4.1 Device geometry

In order to detect the hole mobility in the polymers or polymer blends, we built a hole only device made with the following geometry: ITO/PEDOT/Activelayer/Au. The active layer in the device represents any polymer we want to study. In this case the work-function of the Gold and ITO electrodes are about equal and large, thus electron injection from the cathode is negligibly small.

2.2.4.2 Single carrier space charge limited current

For the hole-only device as described above, the carrier transport is best modeled in the framework of space charge limited current [38].

As expected from our device configuration, ohmic contact on a space charge limited current device yields a nonlinear I-V characteristic since increasing voltage leads to an increase in electric field and injected carriers in the active layer. From Ohms Law we know that the current density is given by:

$$J = en(E)\mu_{DC}E \tag{2.18}$$

where e is the elementary charge (electron or hole), $n(E)$ is the mobile carrier density, μ_{DC} is the carrier drift mobility and E is the electric field's strength in the active layer. $n(E)$ can also be considered as the density of injected carriers because for organic semiconductors where the band-gap energy is above or equal $2eV$ thermally generated carriers are very few compare to injected carriers, and impurities act more as traps than actual carriers sources [39]. From Poisson relation:

$$n(E) = \frac{\epsilon\epsilon_0}{e}\frac{dE}{dx} \tag{2.19}$$

with ϵ_0 and ϵ being, respectively, the free space and the relative permittivity. This equation yields:

$$J = \epsilon\epsilon_0\mu_{DC}E(x)\frac{dE}{dx} \tag{2.20}$$

Using $E(x = 0) = 0$ as boundary condition, we get:

$$E(x) = \sqrt{\frac{2J}{\epsilon\epsilon_0\mu_{DC}}x} \tag{2.21}$$

Considering the device thickness to be d, we can integrate the equation above and obtain $V(x)$ as:

$$V = \sqrt{\frac{8J}{9\epsilon\epsilon_0\mu_{DC}}}d^{3/2} \tag{2.22}$$

From this we get the I-V characteristics as:

$$J = \frac{9}{8}\epsilon\epsilon_0\mu_{DC}\frac{V^2}{d^3} \tag{2.23}$$

This is the Mott-Gurney square law also known as the Child's law for solid [39]. Combining equation (2.23) and equation (2.21), we can get the electric field's strength distribution in the device as a function of the applied voltage.

$$E(x) = \frac{3V}{2d}\sqrt{\frac{x}{d}} \tag{2.24}$$

Knowing the electric field distribution in the device allows one to determine the carriers' transit time, i.e., the time it takes the carriers to go from one electrode to the other. The velocity of moving carriers in the device under an electric field is

$$v(x) = \mu_{DC} E(x) \tag{2.25}$$

The transit time τ_{DC} is thus obtained:

$$\tau_{DC} = \int_0^d \frac{1}{v(x)} dx = \frac{1}{\mu_{DC}} \int_0^d \frac{1}{E(x)} \tag{2.26}$$

Equation (2.24) and equation (2.26) give us the expression of the transit time of holes in our device, namely:

$$\tau_{DC} = \frac{4d^2}{3\mu_{DC} V} \tag{2.27}$$

In case of asymmetric electrodes, or in case there is a built-in voltage in the active layer, the actual voltage in the device when applying an external voltage V is $V - V_{int}$. Thus the real expression for τ_{DC} is:

$$\tau_{DC} = \frac{4d^2}{3\mu_{DC}(V - V_{int})} \tag{2.28}$$

2.2.4.3 Admittance of trap free space charge current limited (SLCL) diodes

Description of SLCL for alternating fields requires the addition to equation (2.18) of a displacement term.

$$J = en(x,t)\tilde{\mu} E(x,t) + \epsilon\epsilon_0 \frac{\partial E(x,t)}{\partial t} \tag{2.29}$$

where $\tilde{\mu}$ is the normalized mobility which is used to account for possible dependence of the mobility on time or frequency, namely:

$$\mu(\tilde{\omega}) = \frac{\mu(\omega)}{\mu_{DC}} \tag{2.30}$$

If there are no traps in the device, $\tilde{\mu}(\omega) = 1$ as the mobility in the device has no frequency dependence. Theoretical description of single carrier SCLC devices has been well studied in the sixties and seventies [40, 41]. They introduced a model for frequency dependent admittance of single carrier space charge limited current devices with no traps. For this derivation, they considered a small AC voltage superimposed with a large DC bias, such that the total voltage applied to the devices is:

$$V(x,t) = V_{AC}(x,t) + V_{DC}(x) = V_{DC}(x) + V_{AC}(x)e^{i\omega t}, \mid V_{AC} \mid \ll \mid V_{DC} \mid \tag{2.31}$$

So according to [39] the complex admittance $Y(\omega) = \frac{I_{AC}}{V_{AC}}$ obtained from the above considerations is:

$$Y(\omega) = \frac{C_{geo}}{\tau_t}\left\{\frac{(\Omega\tau_t)^3}{2i\tilde{\mu}^2[1-exp(-i\Omega\tau_t/\tilde{\mu})]+2\tilde{\mu}\Omega\tau_t - i(\Omega\tau_t)^2}\right\} \tag{2.32}$$

If the device is trap free, i.e., $\tilde{\mu}(\omega) = 1$, one can rewrite equation (2.31) into the sum of a real and imaginary part so it becomes:

$$Y(\omega) = \frac{C_{geo}}{2\tau_t}\Omega^3\left\{\frac{\Omega - sin\Omega}{(\Omega - sin\Omega)^2 + (1 - cos\Omega - \Omega^2/2)^2} - i\frac{1 - cos\Omega - \Omega^2/2}{(\Omega - sin\Omega)^2 + (1 - cos\Omega - \Omega^2/2)^2}\right\} \tag{2.33}$$

where $\Omega = \omega\tau_{DC}$ is the normalized frequency and $C_{geo} = \epsilon A/d$ is the geometric capacitance of the device. Rewriting $Y(\Omega)$ in terms of conductance and capacitance, i.e.,

$$Y(\Omega) = G(\Omega) + i\Omega C \tag{2.34}$$

we can deduce that:

$$G(\Omega) = \frac{G_0 6^3}{\Omega}\left\{\frac{\Omega - sin\Omega}{(\Omega - sin\Omega)^2 + (1 - cos\Omega - \Omega^2/2)^2}\right\} \tag{2.35}$$

with $G_0 = G(0) = \frac{3C_{geo}}{\tau_{DC}} = \frac{9\epsilon\mu_{DC}AV}{4d^3}$

$$C(\omega) = \frac{C_{geo}}{2}\Omega^2\left\{\frac{\Omega^2/2 + cos\Omega - 1}{(\Omega - sin\Omega)^2 + (1 - cos\Omega - \Omega^2/2)^2}\right\} \tag{2.36}$$

At low frequencies, $\Omega << 1$, $G(\omega)$ approaches G_0 and $C(\omega)$ approaches $(3/4)C_{geo}$. At high frequencies, $\Omega >> 1$, $G(\omega) = (2/3)G_0$ and $C(\omega) = C_{geo}$. A simulation of equation (2.35) is given in Figure 2.14. From this figure, it is clear that for trap free space limited current devices, the only parameter that influences the capacitance is the transit time τ_{DC} of the injected charge carriers. In fact, when $f \ll (\tau_{DC})^{-1}$, there is an increase in current as the number of carriers transiting the device is high which implies that there are fewer carriers in the device at a given time. For high frequencies, the current is low because the injected carriers do not have enough time to go across the device, thus an increase in capacitance.

2.2.4.4 Admittance of space charge current limited (SLCL) diodes with dispersive transport

The case studied above is unrealistic in the framework of organic electronics. Most organic semiconductors are full of traps, and thus carriers in these materials are trapped and released many times in their transit from one electrode to the other. This trap and release mechanism induces some relaxation processes in the devices. Hence the transit time cannot be the only influence on the capacitance spectrum. Martens et al. [35] took this into consideration to develop a more complete model for space charge limited current in organic

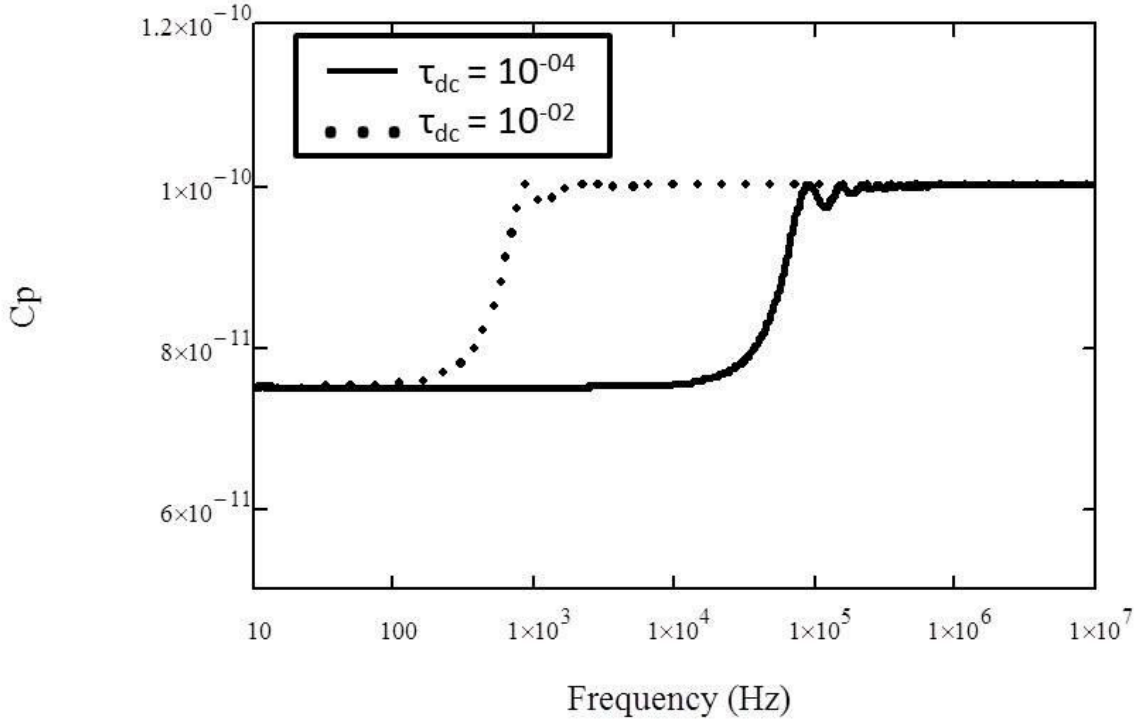

Figure 2.14. Simulation of the capacitance spectrum of a trap free space charge limited current device with $C_{geo} = 0.1nF$ and $\tau_{DC} = 10^{-2}$, 10^{-4} .

diodes. In this model, instead of considering the normalized mobility $\tilde{\mu}$ equal to 1, they assumed the following form:

$$\tilde{\mu}(\omega) = \frac{\mu(\omega)}{\mu_{DC}} = 1 + M(i\omega\tau_{DC})^{1-\gamma} \tag{2.37}$$

where M and γ represent the dispersivity of the sample, with M going from 0 to high values and γ from 0 to 1. High values of M and low values of γ represent high dispersivity. Given the new definition of $\tilde{\mu}$ equation 2.31 can be rewritten and simulation performed for $M = 0, 0.01, 0.1$ and 0.3; with τ_{DC} and C_{geo} kept constant respectively at 10^{-4} and 1. These simulations are given in Figure 2.15

2.2.4.5 Experimental setup and mobility extraction

The capacitance versus frequency can be measured using an impedance analyzer HP4284A. The measurement setup is represented in Figure 2.16. From Figure 2.15, it is obvious that it is necessary to fit the data obtained from the measurement in order to get the transit time. From just plotting the capacitance spectrum the transit time is not easily seen as is the case in trap free systems. So we fit the data with the function given by equation 2.32 and obtain the parameters C_{geo}, τ_{DC}, M and γ. Having obtained τ_{DC}, we can use equation 2.28 to extract the mobility.

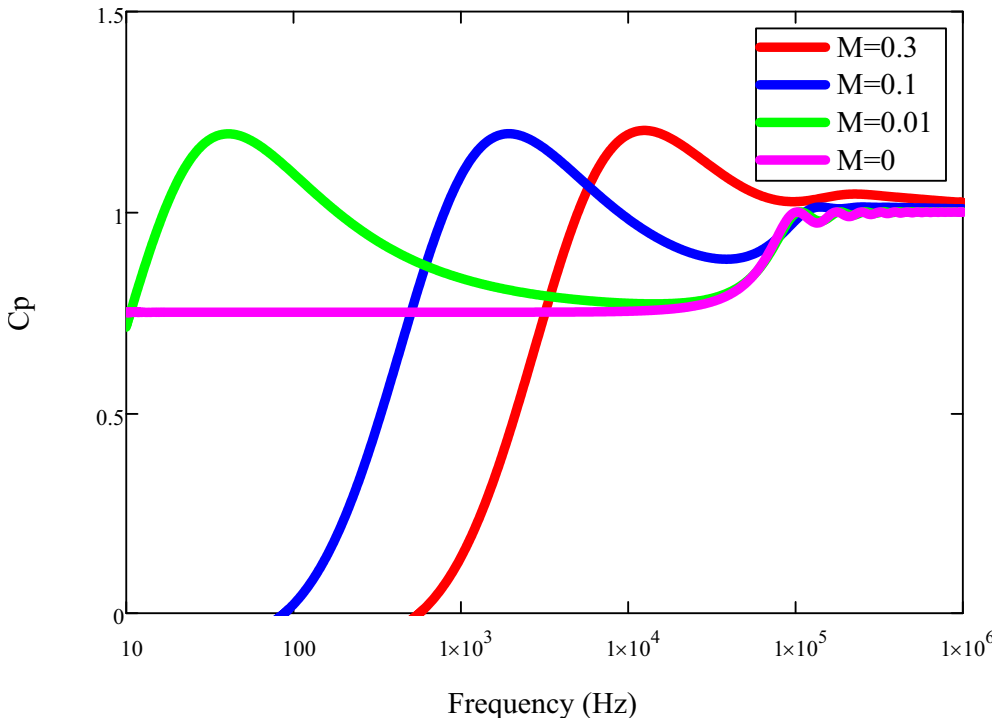

Figure 2.15. Simulation of the capacitance spectrum of a dispersive space charge limited current device with $C_{geo} = 1F$, $\tau_{DC} = 10^{-4}$ and M=0,0.01,0.01,0.3.

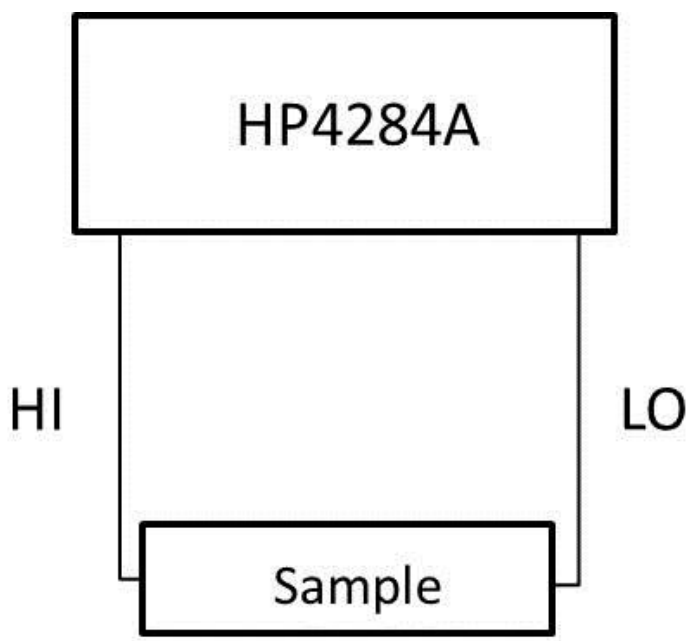

Figure 2.16. Admittance spectroscopy setup.

CHAPTER 3

TRANSPORT STUDIES OF SELF-ASSEMBLED MONOLAYERS

The geometry of organic molecules with an extended aromatic electronic shell that contains carbon bond dimerization makes them natural quasi one-dimensional (1D) systems for studying electrical transport. These organic molecules have been dubbed "molecular wires"due to the low value of the electron wave function decay constant associated with large intramolecular electron transmission along the molecular principal axis. Starting with the first "single molecule"electronic device [42], Molecular Electronics in low dimension using such wire molecules has remained a domain of active research in recent years. Currently, the most popular approaches used in fabricating such 1D molecular diodes are mechanical break-junction, electromigration break junction, nano-pore method, nano-particle bridged junction, and a broad range of devices that involve STM or AFM tips as upper electrode.

In two-dimensional (2D) macromolecular systems, on the contrary, an additional dimension is formed due to in-plane charge delocalization in a direction perpendicular to that of the 1D intramolecular transport. Such a situation exists, for example in casted films of regio-regular poly(3-alkyl-thiophene) in which self-assembled lamella are formed perpendicular to the film substrate, and in molecular layer epitaxy structures [8, 9]. Other ordered organic molecular systems also show delocalization perpendicular to the principal molecular direction, for example, single wall carbon nanotubes sheets, polyacetylene microcrystalline fibers, and even DNA double helix molecules. Currently there is a fragmental insight of charge and energy transport in 2D organics that originates mostly from the fields of conjugated polymers and biophysics. However despite the tremendous advance in fabricating molecular diodes, reproducibility is still considered a challenge for experimentalists.

It is therefore appealing to have a molecular engineering tool that enables fabrication of organic solid-state mixture (SSM) with controllable dimensionality, which may mainly influence electrical transport. The development of such a molecular engineering approach would enable systematic transport studies of molecular organic devices with tunable dimen-

sionality. This may be analogous to inorganic structures, in which the dimensionality is well controlled from 3D (crystals) to 1D (quantum wires). We have recently introduced such a molecular engineering approach of SSM of self-assembled monolayer (SAM) devices.

3.1 Evidence for SAM device formation

3.1.1 Conductive and nonconductive molecules

Molecular electronics is the field of electronics which has the goal of replacing the conventional electronic devices with devices made out of molecules. Work is being done to replace electronic devices such as diodes, transistors and photovoltaic cells with their molecular counterparts. This is made possible with the discovery that some organic materials behave like semiconductors; they are called organic semiconductors. This divides organic materials into two categories: saturated molecules and unsaturated molecules

- Unsaturated molecules: an unsaturated hydrocarbon (or other organic molecule) contains double or triple bonds between certain atoms. These bonds may be broken and new atoms attached without disrupting the existing skeleton of the hydrocarbon.

  Unsaturated molecules were mostly studied after a serendipitous discovery of metallic-like properties of doped polyacetylene films: upon doping the film with iodine, the conductivity increased by a factor of 10 million [43, 44]. Polyacetylene is an example of a special group of unsaturated polymers, namely conjugated molecules and polymers. In conjugated polymers single and double bonds alternate in the main chain. The presence of the alternating single and double bonds is responsible for the interesting properties of this class of polymers. Take for example polyacetylene: each carbon atom in the chain has one unpaired electron (electron configuration sp^2pz^1). These unpaired electrons give rise to π-bonds in the conjugated polymer. The mutual overlap of the π-orbitals on neighboring atoms in the polymer chain causes the wave functions to delocalize over the conjugated polymer. The unpaired electrons form a half-filled band. However, the half-filled band does not give the material metal-like properties: all pristine conjugated polymers, including polyacetylene, have absorption gaps that fall in the range from $1 - 4eV$. The presence of the gap may be explained by either a strong electron-electron interaction, or by a structural rearrangement of the polymer backbone, or by a combination of both effects. If the system has strong electron-electron interactions, the gap may be explained by a so-called Mott-Hubbard insulator [45]. If structural rearrangements are important, then the system may be subject to a lattice instability: the system lowers its energy by creating alternating single

and double bonds. The lattice distortion is known as Peierls instability [46]. In the Su-Schrieffer-Heeger (SSH) theory the interaction between electrons and the molecular geometry is explicitly described (by an electron-phonon coupling constant), and the interaction between electrons is neglected [47, 19].

- Saturated molecules: a saturated hydrocarbon (or other organic molecule) has utilized all of its bonding electrons to make single bonds to other atoms. It cannot make additional bonds without cutting off part of the existing molecule. All electrons are therefore localized and thus these molecules are nonconductive.

In this work we used as the conductive molecules 1,4-methane-benzenedithiol [Me-BDT] also called molecular wire (MW). Each of the "thiol"parts of the molecule represents the head and the tail group that permits attachment to the electrode. The nonconductive molecule here is a saturated molecule also called molecular spacer (MS)1-pentanethiol [PT] with only one thiol group that enables the attachment to the bottom electrode. The nonconductive molecule has only thiol groups in order to decrease the tunneling probability and thereby reduce even further the conductivity of this channel in a device configuration. We define:

$$r = \frac{N_{MW}}{N_{MS}} \tag{3.1}$$

as a ratio of the molar concentration of molecular wire by the molar concentration of molecular spacers.

3.1.2 Monolayer formation

The step-by-step growth of the organic monolayers was characterized by contact angle changes, ex situ ellipsometry, and UV-visible reflectance spectroscopy; these are briefly summarized in Figure 3.1. After step A in Figure 2.2, the contact angle changed from 17° to 45°, and the UV-Vis reflectivity spectrum of the film grown on the Au/Si substrate showed a $261\,nm$ peak characteristic of the highest occupied molecular-orbital to lowest unoccupied molecular-orbital (HOMO-LUMO) transition of the Me-BDT molecule (Figure 3.1).

Variable angle spectroscopic ellipsometry (Woollam Co.) was used to verify the monolayer growth in the device structure (Figure 3.2). This method measures the optical spectra with $5\,nm$ wavelength resolution in the spectral range of $300 - 600\,nm$. The structural model for fitting the ex situ ellipsometry data uses the collected data from three different incident angles, namely, 165°, 70°, and 75°. The obtained and fitted ellipsometric spectra for the structures containing Si/SiO2, Au, and Me-BDT/PT monolayers exhibit molecular

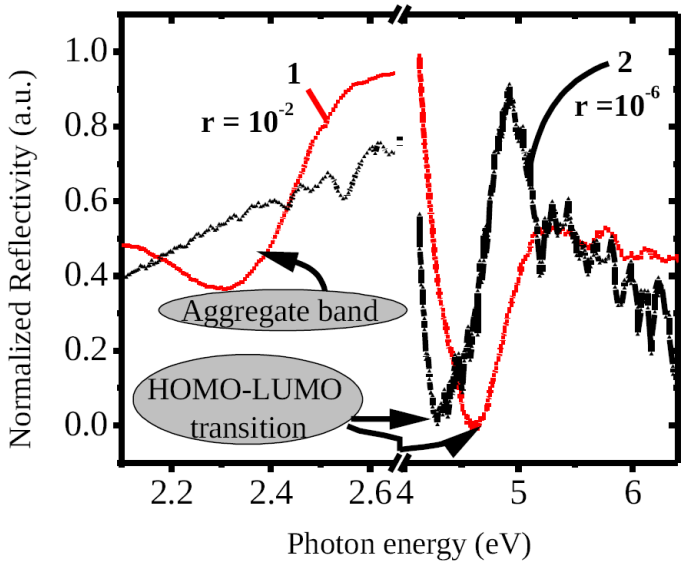

Figure 3.1. Basic optical measurements of the fabricated SAM devices. (a) The optical reflectivity spectrum of SAM films with $r = 10^{-2}$ (red dashed line, 1), and $r = 10^{-6}$ (black solid line, 2) that show a prominent feature at the HOMO-LUMO transition of the Me-BDT molecule at about $5\,eV$. For $r = 10^{-2}$ there is another optical feature in the visible spectral range associated with Me-BDT aggregates.

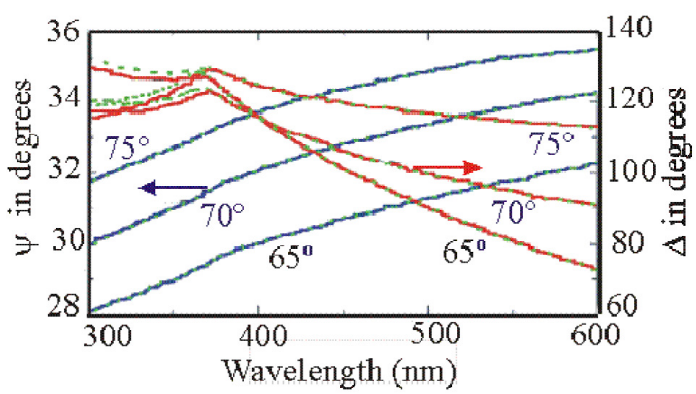

Figure 3.2. Ellipsometry spectra of two optical constants: ψ (dashed line) and Δ (dot line) that were measured at three different angles, from which a film thickness of $\sim 1\,nm$ was derived. The solid lines through the data points are model fittings.

c-axis interplanar spacing of $30.2\,nm$ for the bottom Au film, and $10\,\AA$ for the monolayer of Me-BDT/PT SSM; this indicates that single monolayer growth has been achieved.

3.1.3 Electrode connectivity

The theory of SAM formation has been explored in Chapter 2. So as far as connectivity with the bottom electrode is concerned, we will redirect the reader to this chapter for proof. To address the formation of covalent bonds between the Me-BDT molecules in the SAM devices and the upper electrodes, we fabricated a SAM structure comprised of iodopropyl-trimethoxysilane self-assembled on a SiO2/Si film. This was followed by chemisorption of either an Me-BDT monolayer, or a PT monolayer that was used as a control structure. For studying the sulfur-metal bonding of the upper electrode we used the silane matrix as a template layer for SAM, thus avoiding the contribution of the bottom sulfur-metal bonding to the absorption spectra in the infrared (IR). The silane matrix is semitransparent in the mid-IR spectral range allowing absorption spectroscopy study of the upper surface vibrational modes. We studied the stretching vibration frequency of the C-S-metal bond for Au and Co electrodes in addition to Al.

Upon deposition of the upper electrode, we were able to detect the formation of Au-S bonds, since the frequency of the ir-active Au-S stretching vibration is different from that of the original C-S stretching vibration (before metal deposition) (Figure 3.3). In fact the ir-active vibration frequency shifts from $\sim 798\,cm^{-1}$ (Figure 3.3, black line) for the C-S stretching mode to $\sim 614\,cm^{-1}$ (Figure 3.3, orange line) for the AuS-C mode. This red shifted ir-active vibrational mode was absent in the control device that contained only PT molecules. Cobalt is lighter than gold leading to a smaller red shift. Indeed we found that the ir-active Co-S-C stretching vibrational mode shifts to $671\,cm^{-1}$ (Figure 3.3, red line) while Al-S-C stretching vibrational mode shifts to $770\,cm^{-1}$ (Figure 3.3, blue line). This justified by the fact that Aluminium is lighter than Cobalt. So as expected, the shifts obtained from these are $28\,cm^{-1}$ for Al, $127\,cm^{-1}$ for Co and $184\,cm^{-1}$ for Au.

3.1.4 From single molecule to aggregated molecules

In this work, we introduced a unique approach in which a conducting molecule is introduced in a matrix of nonconductive molecules. Both molecules are then self-assembled on a substrate for transport studies. It was discovered that by varying the concentration of the conducting molecules with respect to the nonconductive ones, we could actually go from one-dimensional transport to a two-dimensional transport. It is self-evident that at very low concentration, MW are essentially isolated from one another and increasing

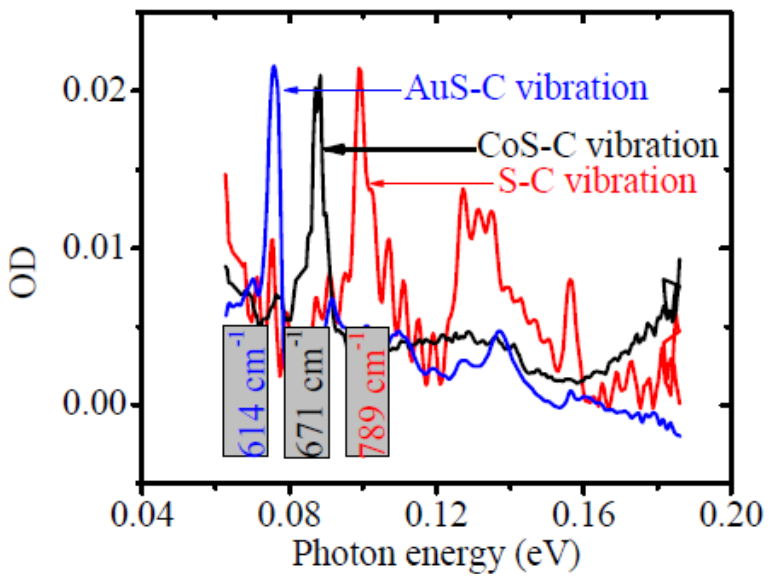

Figure 3.3. FTIR absorption spectra of the Me-BDT molecule bonded to the upper electrode that shows an ir-active AuS-C stretching vibration (blue line), CoS-C stretching vibration (black line) compared with a reference film that shows the ir-active S-C stretching vibration (red line).

this concentration should bring them closer and closer and at some point there could be interaction between these molecules. This intermolecule interaction should be visible in the transport and possibly in the optical properties of the devices.

In the UV-visible reflectance measurements (Figure 3.1), we note that HOMO-LUMO transition for the molecular aggregates is blue shifted by $\sim 20nm$ with respect to that of the isolated Me-BDT molecules. Moreover the visible part of the optical reflectivity spectrum reveals a new characteristic transition of Me-BDT molecular aggregates, which are present at large r-values. This was taken as evidence that Me-BDT molecules form aggregates for r-values in the range $r > 10^{-3}$.

Wavelength dependant ellipsometry spectra look very different for molecular aggregates compared to isolated molecular wires. While ellipsometry spectrum of isolated molecular wires (Figure 3.2) resembled structure of film grown on Si substrate, which is transparent in the visible spectral range, ellipsometry spectrum of molecular aggregates (Figure 3.4) has pronounced spectroscopic features in the visible spectral range.

3.2 Single molecule transport

Following the fabrication of SAM SSM diodes on gold electrodes we measured the I-V characteristics of the diodes at different r-values and temperatures. At small r-values in the range $r < 10-4$ we expect the conducting Me-BDT molecules to be isolated in the otherwise insulating PT matrix. This could be directly verified from optical reflectivity measurements that show a peak of the isolated Me-BDT molecule at about $4.2\,eV$ (Figure 3.1(a), solid line$\neq$1) and absence of any peaks in the visible spectral range that are associated with the formation of Me-BDT molecular aggregates (Figure 3.1(a), dashed line$\neq$ 2).

3.2.1 Devices with $r = 0$

For reference, we shall first discuss the conductivity measurements of devices having $r = 0$; these are composed of only molecular spacers (PT molecules). It should be noted that all temperature dependent conductivity measurements were performed under a dynamic vacuum. The I-V curves of one of such devices measured at different temperatures are shown in Figure 3.5(a); the detailed I-V curves in a smaller voltage interval are shown in Figure 3.5(b). The I-V curves are nonlinear showing that the PT SAM device does not contain a substantial amount of pinholes; otherwise we would have observed a linear, ohmic behavior. In addition, the I-V response curves show a dramatic temperature dependence which is indicative of charge injection (or extraction) via thermionic emission. In Figure 3.5(c) the temperature dependent transport data are presented in terms of differential

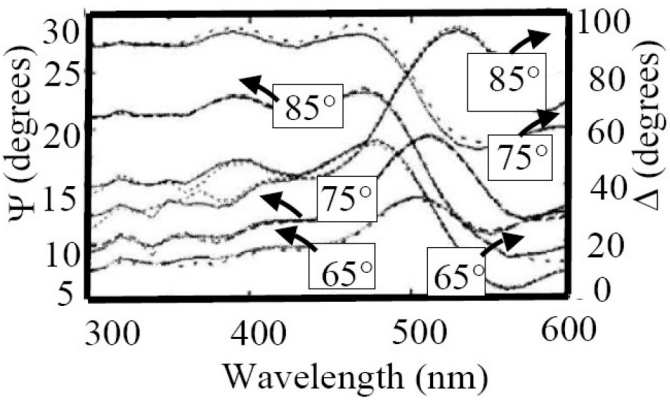

Figure 3.4. Ellipsometry spectra of two optical constants: ψ (dashed line) and Δ (dotted line) that were measured at three different angles, from which a film thickness of $\sim 1\,nm$ was derived. The solid lines through the data points are model fittings.

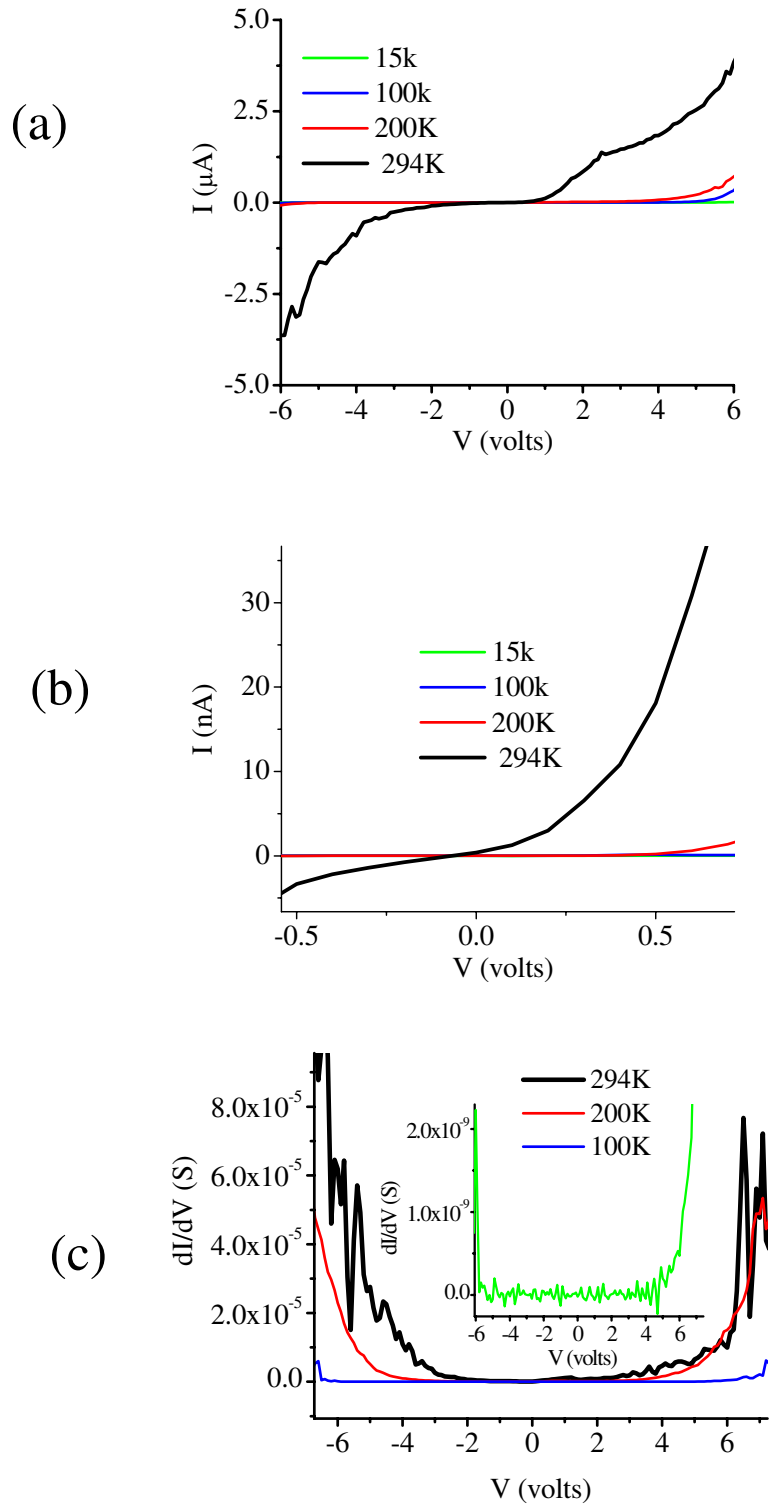

Figure 3.5. Electrical transport studies of a SAM device made of PT ($r = 0$) at various temperatures. (a) and (b) show the measured I-V characteristics; (c) shows the differential conductivity spectra obtained from (a). The inset in (c) is dI/dV vs. V at 15 K.

conductance spectra (DCS = dI/dV vs. V); the inset is the DCS at 15K, where the contribution of thermionic emission is negligibly small. There is a dramatic increase in conductance of (∼four orders of magnitude) when the temperature changes from 100K to 300K. However below about 100K the conductance does not change as much. This is well revealed in the Arrhenius plot of $ln(I) vs. 1000/T$ for various voltages, as shown in Figure 3.6(a). The estimated activation energy for this device at $V = 0$ is $\sim 0.7\,eV$; however at higher bias voltages the activation energy decreases substantially. This is expected as there is no connection or bonding between the molecules and the top electrode. The DCS at all temperatures show an exponential increase (Figure 3.5(c)) starting from a certain voltage V(on). If we assume that at low temperature, the transport mechanism is dominated by the resonant tunneling through the PT molecule and the spatial gap between the PT molecule and Au electrode, it is thus safe to conclude that at 15K the DCS maps the electronic density of states of the charged molecule. Applying voltage to the device will essentially raise the Fermi level of the electrode E_F until it is in resonance with the HOMO (or LUMO) level of the molecule. This happens when the voltage $V(on) = 2\Delta/e$, where Δ is the energy difference between E_F and the molecular HOMO (LUMO) level. By looking at the DCS at 15K we get $V(on) = 5\,V$ which gives $\Delta = 2.5\,eV$. This value of Δ obtained is smaller than the reported value of the HOMO-LUMO gap of the molecule [42]. The implication of this is that the Fermi level of the metal lies in the gap of the molecule.

3.2.2 Devices with $10^{-7} < r < 10^{-4}$

A similar analysis was also conducted for SAM SSM devices with various r-values in the range $10^{-7} < r < 10^{-4}$, where the Me-BDT molecules are isolated in the PT matrix. From the I-V curve of PT devices ($r = 0$) at room temperature (Figure 3.5(b)) we estimated the minimum r-value at which the conductivity is dominated by the isolated Me-BDT molecules. The conductivity, $G = I/V$ is traditionally measured at small $V \sim 0.1V$.

From Figure 3.5(b) we get $G_0 = 2.10^{-8}\,\Omega^{-1}$. Any SAM SSM device having $G > 10G_0$, may then be regarded as dominated by transport through the isolated molecular wires in the device. The I-V curves of SAM SSM devices with $r = 10^{-7}$, 10^{-6} and 10^{-5} are shown, respectively, in Figure 3.7 and Figure 3.8. G at 0.1 V for the SAM device with the smallest r-value, namely $r = 10^{-7}$ is $2.10^{-6}\,\Omega^{-1}$; this is about two orders higher than G_0 and is thus dominated by the molecular wires in the device.

In addition, G increases linearly with r for the other measured SSM devices, as shown in Figure 3.9. We thus conclude that the lower limit r-value for which the SAM SSM devices are still dominated by transport through isolated Me-BDT molecules is $r \approx 10^{-8}$.

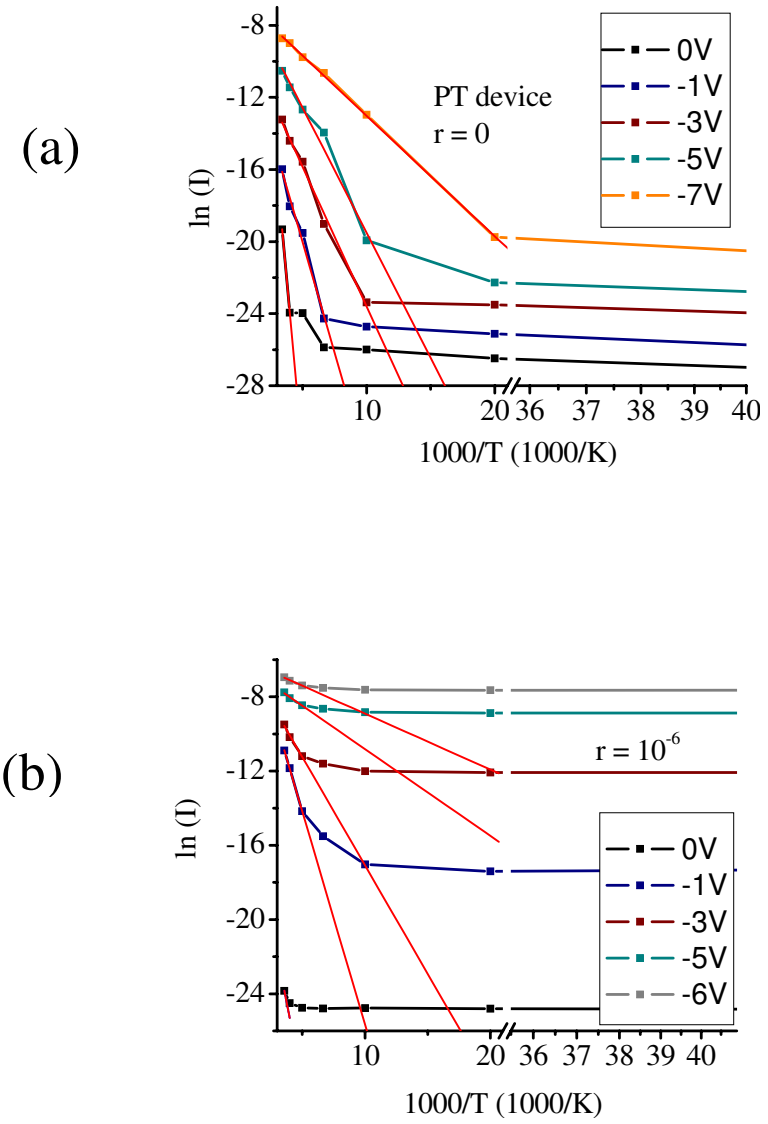

Figure 3.6. Arrhenius plots of the current at different biasing voltages for the SAM device of PT (a), and SSM SAM device with $r = 10^{-6}$ (b). Red lines are linear fits for ln(I) rise at high temperatures.

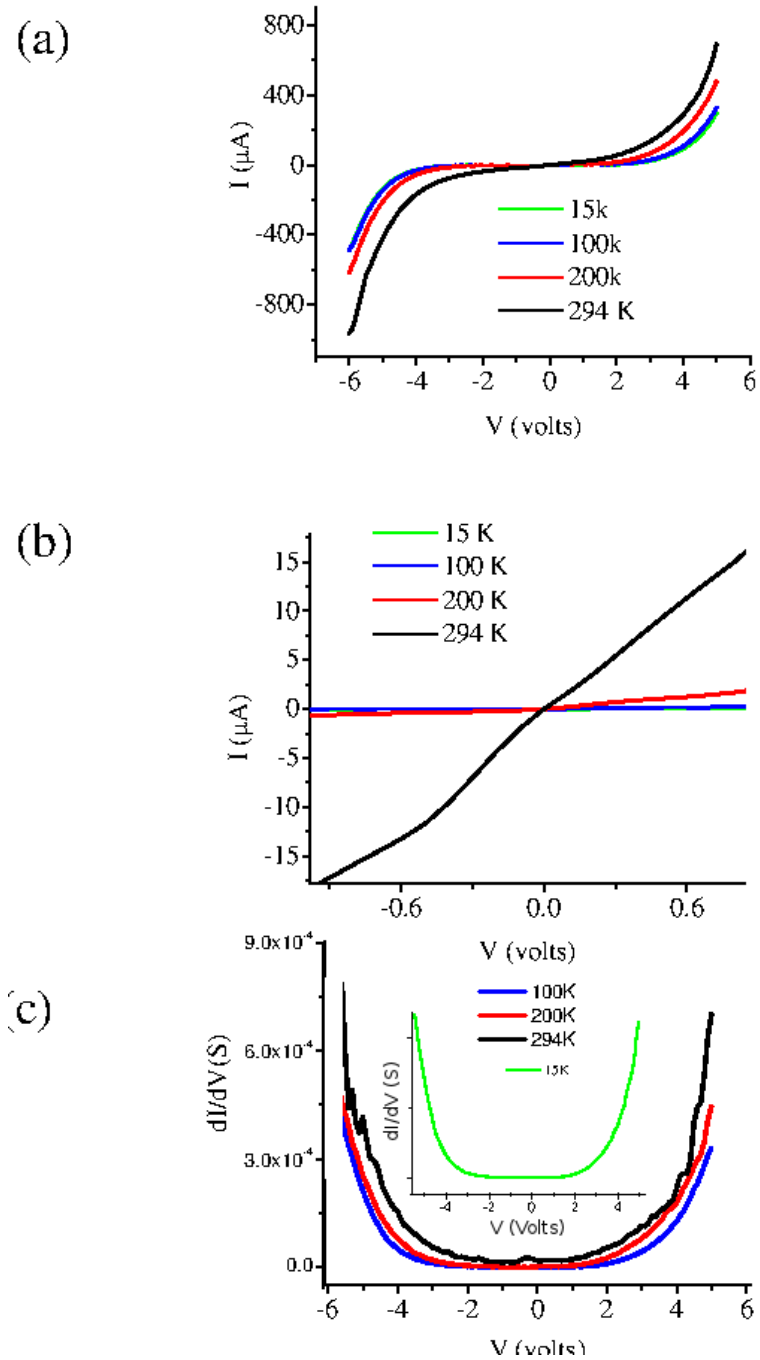

Figure 3.7. Electrical transport studies of a SAM device made of SSM with $r = 10^{-6}$ at various temperatures. (a) and (b) show the measured I-V characteristics at different voltage ranges; (c) shows the differential conductivity spectra , dI/dV vs. V obtained from (a). The inset in (c) is dI/dV vs. V at 15 K.

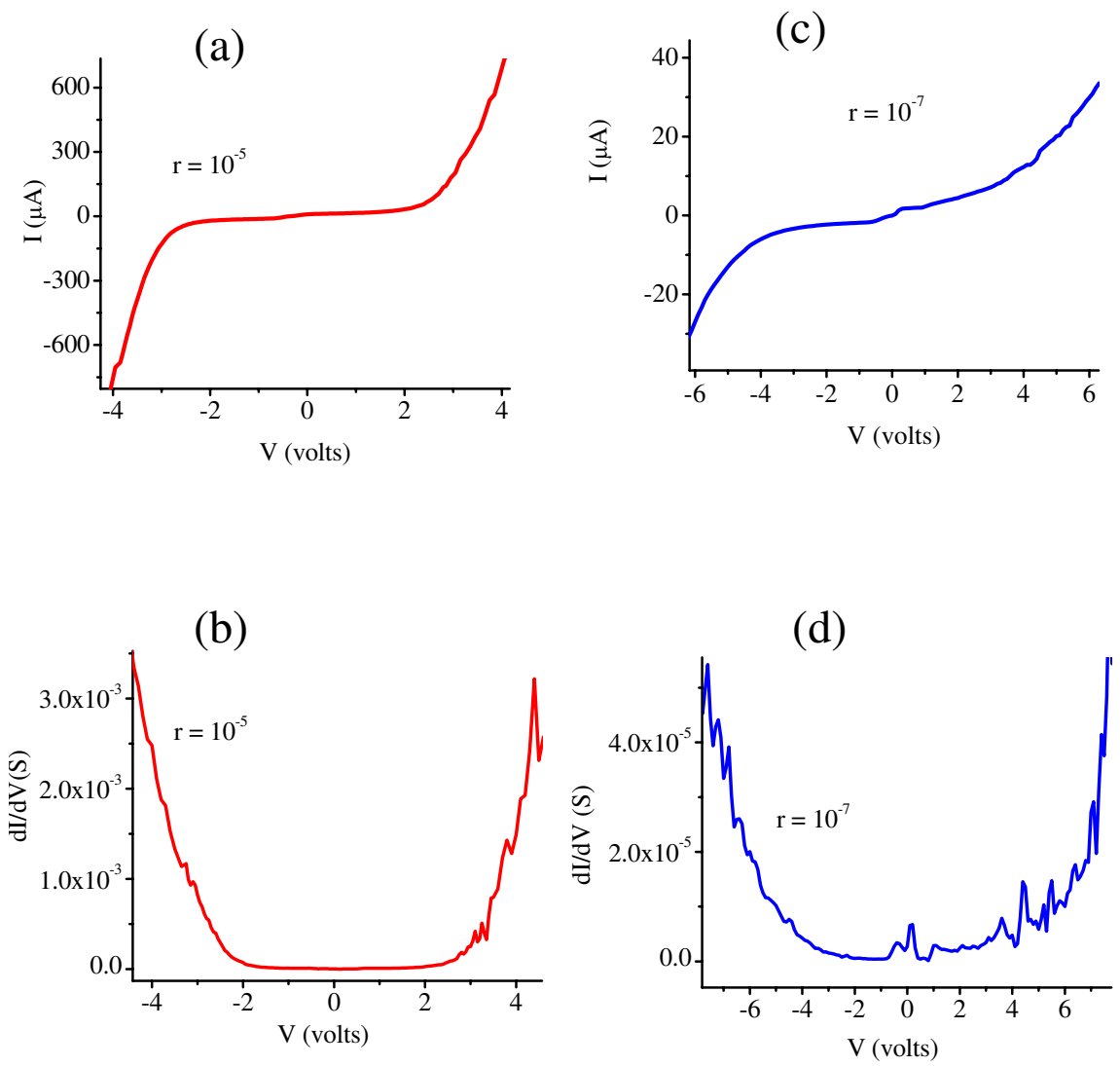

Figure 3.8. SSM SAM devices at room temperature with $r = 10^{-5}$ (a) and (b); and $r = 10^{-7}$ (c) and (d).

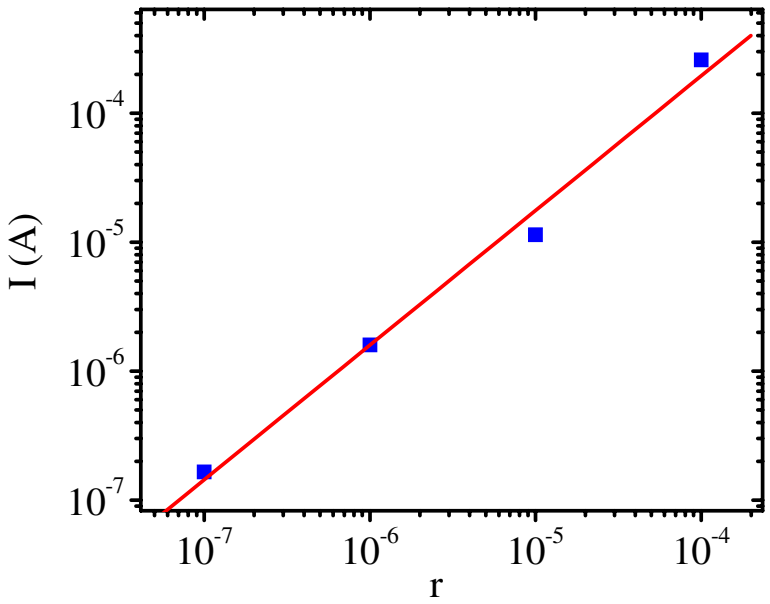

Figure 3.9. Room temperature current of SSM SAM devices fabricated with various r-values vs. r. A linear line through the data points is also shown indicating the dominant role of the isolated Me-BDT conductivity superposition.

The conductance of the fabricated SSM device with $r = 10^{-6}$ is analyzed in more detail in Figure 3.7. Figure 3.7(a) shows that the nonlinear I-V characteristic is only weakly temperature dependent in contrast to the PT device (Figure 3.5). This can be also concluded from the Arrhenius plots in Figure 3.6(b). The activation energy that may be extracted at intermediate biasing voltage is $\sim 50\,meV$, which is about an order of magnitude smaller than that of the PT device (Figure 3.6(a)). Since the Me-BDT molecule is bonded to the Au atoms of the two opposite electrodes, this small activation energy cannot be due to thermionic emission over a barrier caused by a vacuum gap, as in the case of the "PT only"device discussed above. The obtained weak temperature dependence may reflect the temperature dependence of Δ_{BDT} between $E_F(Au)$ and Me-BDT HOMO level; it is conceivable that this energy depends on the temperature, similar to many inorganic semiconductors. The weak temperature dependence may also reflect the effective molecular length, which plays an important role if the transport occurs via tunneling. In this case tunneling may be influenced by twists and/or rotation around the principal axis of the molecule, which are formed at high temperatures and thus contribute to the temperature dependence.

A better understanding of the weak temperature dependence is provided in Figure 3.7(d), where the DCS are plotted at four different temperatures. From the 15K data that should not contain any thermionic emission contribution, it is apparent that there is an abrupt onset voltage, V(on) for the increase in conductance at $\sim 3\,eV$. As for the PT device discussed above, we can thus estimate Δ_{BDT} from V(on) using the relation $V(on) = 2\Delta_{BDT}/e$; we get $\Delta_{BDT} \sim 1.5\,eV$. Figure 3.7(c) also shows that V(on) decreases with the temperature indicating that indeed Δ_{BDT} depends weakly on the temperature, as assumed above.

In Figure 3.8 (a) and (c), the I-V is highly nonlinear showing an abrupt increase at $V(on) \sim 3\,eV$, similar to the device with $r = 10^{-6}$ discussed above. This shows that the transport mechanism for these two devices is basically the same. Moreover the symmetry between positive and negative biasing voltages is maintained almost perfectly in all SSM devices, whereas it is less symmetric for the PT device (Figure 3.5). This is in agreement with the symmetry of the fabricated SSM devices and Me-BDT molecule. In the case of devices with only PT molecules, the gap between the molecule and the upper Au electrode may also contribute to the lack of symmetry in the I-V. In Figure 3.8(b) and (d), the gap in conductance is maintained up to $\sim 3\,eV$, where there is an abrupt increase in the conductance. This may show that E_F(Au) reaches the HOMO level at this biasing voltage.

The SSM device with $r = 10^{-7}$ shows a larger gap, which may be due to the PT

contribution to the conductance mechanism of this device. We also evaluated the room temperature conductance of the SSM SAM devices at $V = 0.1\,V$, as depicted in Figure 3.9. The linear dependence of G with r shows that the transport processes of the SSM devices in this r-value range are shared by all devices up to $r = 10^{-4}$, where the conductivity scales with the density of the molecular wires. We therefore conclude that charge transport in these devices is dominated by the conductance through isolated Me-BDT molecules.

3.2.3 Single molecule resistance

The additive law of molecular devices should occur for molecular wires in parallel configuration [48, 49]. As the conductivity of the SSM diodes scales with the number of Me-BDT molecules in the device, we can extract the resistance, R_M, of a single molecular wire from Figure 3.8. If the wires are isolated in the device then the device conductance is simply given by $\sigma = N\sigma_M$, where σ_M is the conductance of single molecules, assuming all molecules have equal conductance. We may then write:

$$R = \frac{R_M}{N} \tag{3.2}$$

where R is the device resistance and N is the number of active molecular wires in the device. From Figure 3.8 and using equation 3.2 we thus obtained the average R_M value to be $6(\pm 3) \bullet 10^9\,\Omega$. This value is in excellent agreement with that obtained using STM measurements $R_M = 4.5 \bullet 10^9\,\Omega$[,7,46]. However in contrast to STM measurements, our SSM SAM method used here can in principle be used for device application, and also enables us to perform electrical measurements at low temperatures with relative ease.

3.2.4 Modelization

To rationalize the measured molecular resistance R_M we employed the Landauer formula for linear electrical conductance G to calculate the electrode-molecule-electrode junction resistance. In this model G is given by the relation:

$$G = \frac{2(e^2 \times T)}{h} \tag{3.3}$$

where h is the Planck constant, and T is the electron transmission efficiency from one contact to the other, which is a function of the applied voltage, V. T can be divided into the following three components:

$$T = T_L \times T_R \times T_M \tag{3.4}$$

where T_L and T_R give the charge transport efficiency across the left and right contacts, respectively, and T_M is the electron transmission through the molecule itself. We may

approximate T_M by the coherent, nonresonant tunneling through a rectangular barrier. In this case T_M is given by

$$T_M = e(-\beta L) \tag{3.5}$$

where L is the potential barrier width, i.e. the effective molecule length, and β is the tunneling decay parameter given by:

$$\beta = \frac{\sqrt{2m * \alpha(\Phi - eV/2)}}{\hbar} \tag{3.6}$$

where $\hbar$ is $h/2\pi$,Φ is the barrier height for tunneling through the HOMO level, which is equivalent to the energy difference Δ_{BDT} between E_F(Au) and Me-BDT HOMO (LUMO) level, m^* is the effective electron mass given in terms of m_0 (the free electron mass), V is the applied voltage across the molecule, and α is a parameter that describes the asymmetry in the potential profile across the electrode-molecule-electrode junction [42].

We may estimate the electron transmission T_M through the molecule using equation 3.5. The left and right electron transmission, however, are more difficult to calculate. They may be negligibly small in our case since there is no charge injection barrier into the molecular channel, as indicated by the weak temperature dependent transport in our devices. The value m^*/m_0 in equation 3.6 ranges from 0.16 for conjugated molecules, to 1.0 for saturated molecules [42]. Me-BDT has a single aromatic ring and two saturated methyl spacers, so that the value m^*/m_0 should be intermediate between completely conjugated and completely saturated molecules. Thus we take $m^* = 0.58$ for the Me-BDT molecule. The asymmetry parameters α should be close to 1 since the Me-BDT molecule is symmetric. Furthermore in equation 3.6 we take $V = 0.1\,V$ and $L = 10\,\AA$ (the estimated Me-BDT effective molecule length), and the tunneling barrier height $\Phi = \Delta_{BDT} = 1.5\,eV$ (Figure 3.7). Using equation 3.3 - 3.6 with the Me-BDT parameters as determined above, and neglecting the transmissions at the left and right interfaces, we obtain $R_M \simeq 10^9\Omega$ for the molecular resistance. This is about six times smaller than the measured R_M value, but in the young field of Molecular Electronics is considered to be an excellent agreement with the experiment. The very good agreement between the experimental and calculated R_M values points out that thermionic emission is a negligible small contribution for the Au/Me-BDT junction at room temperature; this is consistent with the weak temperature dependent transport that we have measured.

3.3 Transport studies of aggregated molecules

3.3.1 Transport studies of Au/SAM/Au diodes

We studied the transport properties of the fabricated molecular diodes at various temperatures by measuring the characteristic current-voltage ((I-V) dependence and the differential conductance vs. the applied voltage, V. For devices with r-values in the range of $r < 10^{-4}$ we previously found that the molecular wires (Me-BDT) are isolated in the otherwise insulator PT matrix, and thus the device electrical conduction is dominated by the isolated molecular wires down to $r = 5 \bullet 10^{-8}$ [42]. In the current contribution we report on studies of 2D systems using the same SAM SSM method but at higher molecular wire concentration in the range of $10^{-3} < r < 1$.

We found that molecular wire aggregates are formed for devices having $r > 10^{-3}$. For such SAM devices we observed a new transport channel (Figure 3.10(a) and (b)) as well as novel optical (Figure 3.11) features, which are related to formation of new states in the Me-BDT HOMO-LUMO gap. When Me-BDT aggregates are formed in the SAM, then an additional transport channel is available, where the injected charges may move in-plane in addition to the preferred direction along the molecular axis. As is apparent in Figure 3.10(a) the I-V response of such a device is much steeper at low V compare to that of devices with isolated Me-BDT molecules and also shows much higher conductivity. Moreover a new feature appears in the DCS spectrum at $V < 0.8\,V$, in addition to the DCS tunneling features characteristic of the isolated Me-BDT molecules seen at higher V (at $\sim 3\,eV$). Specifically, the I-V response at $V < 0.8\,V$ appears to be linear, with some nonlinearity in the vicinity of $V = 0$ (Figure 3.10(a)). This feature in I-V gives rise to a peak in the DCS spectrum at low temperature for $V < 0.8\,V$ (Figure 3.10(b)). For V larger than $\sim 1\,V$ the additional DCS aggregate-related band diminishes, and turns back to that of typical tunneling through SAM molecules seen in isolated molecule devices at high V (Figure 3.12(a)).

3.3.2 The formation of gap states in aggregated Au/SAM/Au devices

To explain the novel DCS feature around $V = 0\,V$ in aggregated SAM devices we consider that a narrow continuum band (COB) of molecular orbitals is formed due to the in-plane π -electron stacking. This is analogous to the well-known narrow impurity band formed in heavily doped semiconductors due to overlapping nearest-neighbor orbitals, for example, phosphorous impurity band in heavily n-type silicon doping. If the molecular COB lies close to E_F(Au) then an abundance of dense molecular levels are available for electron

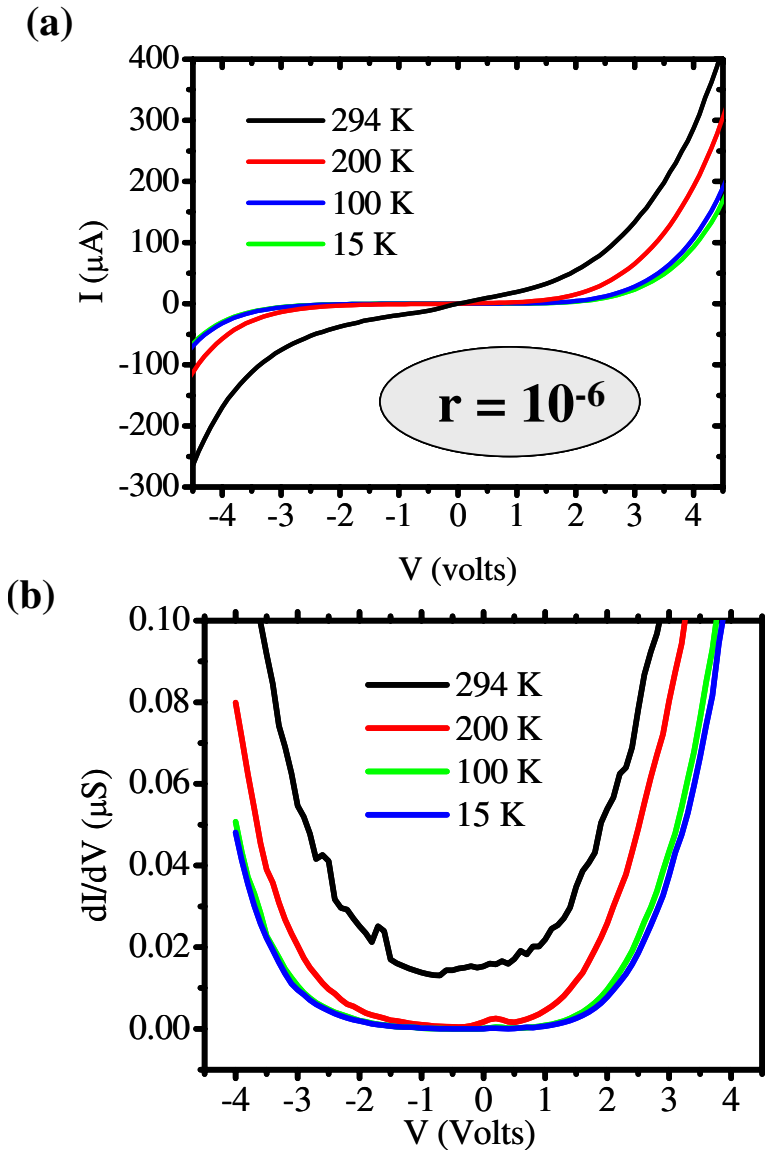

Figure 3.10. Room temperature current of SSM SAM devices fabricated with various r-values vs. r. A linear line through the data points is also shown indicating the dominant role of the isolated Me-BDT conductivity superposition.

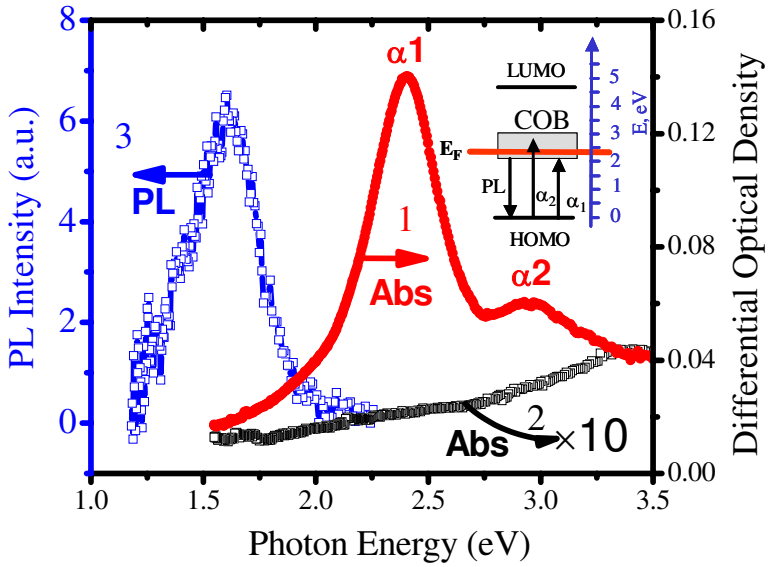

Figure 3.11. Normalized optical reflectivity spectra of SAM films on Au and Al electrodes, respectively, at two r-values: (i) $r = 10^{-6}$ for isolated Me-BDT; and (ii) $r = 10^{-2}$ for molecular aggregates. The Me-BDT HOMO-LUMO transition at $\sim 4.5\,eV$, and the optical transition related to Me-BDT aggregates at $\sim 2.3\,eV$ are assigned.

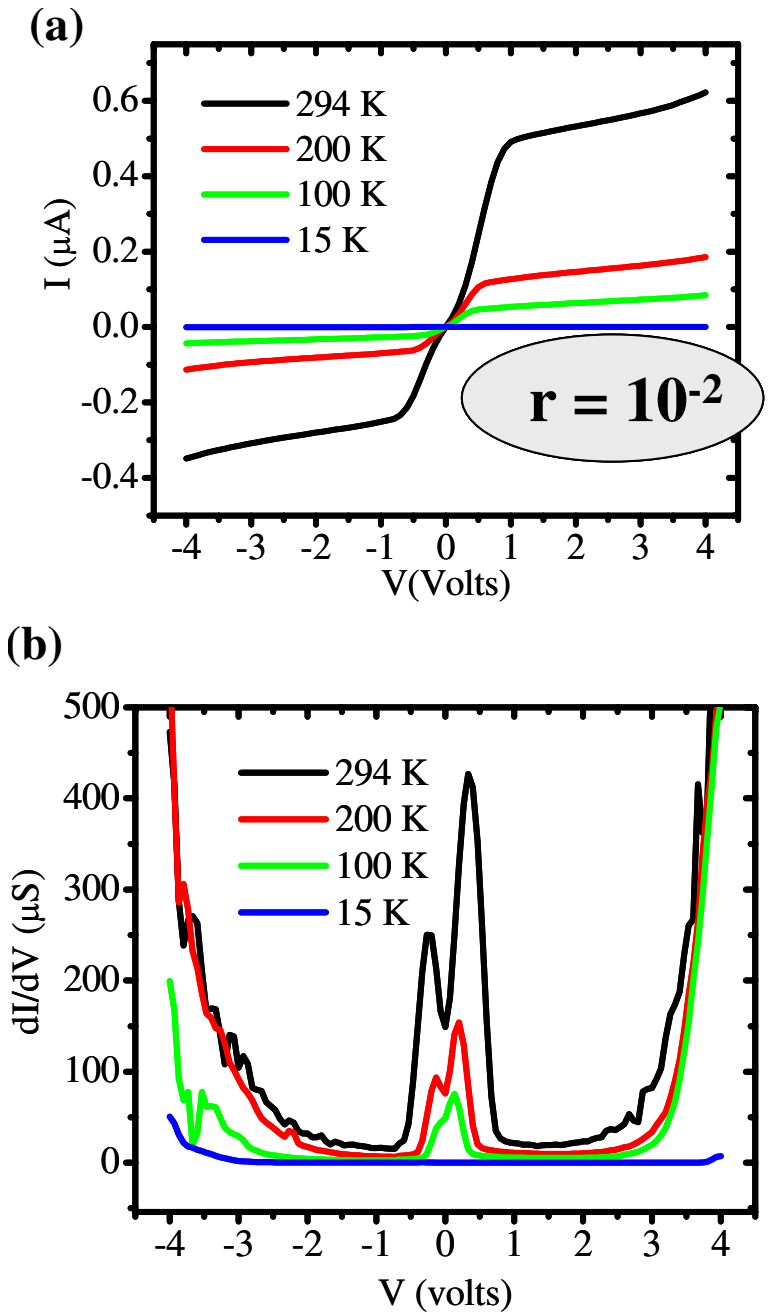

Figure 3.12. Electrical transport measurements of SAM diodes with $r = 10^{-6}$ at various temperatures, showing isolated Me-BDT behavior. (a) I-V characteristics; (b) differential conductance spectrum obtained from (a).

transport, and consequently this would dramatically enhance the electrical conductivity (Figure 3.11 insert). In this case a low interface barrier potential would form between the metal electrode and the aggregate-related COB, similar to the case of metal/heavily-doped-semiconductor interface in metal/SEC/metal devices.

Taking into account this simple model we can explain the transport properties obtained in aggregated SAM devices. We infer the existence of a very efficient transport mechanism in the voltage range in which E_F(Au) is aligned with the molecular COB. In this model both I-V and DCS at low bias voltage are dominated by carrier injection into the molecular COB. The in-gap COB is scanned upon ramping the applied voltage, and at$V = V_{max} \sim 0.8\,V$ E_F(Au) is no longer aligned with the COB band in the gap because the aggregate-related COB is narrow. Then the I-V and DCS spectra for $V > V_{max}$ again exhibit the usual tunneling features typical for isolated molecular wires; specifically the conductivity increases again when E_F(Au) becomes aligned with the Me-BDT molecular HOMO level, as in SAM devices with $r < 10^{-4}$.

During the SAM growth (step A in Figure 2.2) the UV-Vis reflectivity spectrum shows a strong 286 nm band characteristic of the HOMO-LUMO optical transition for the isolated Me-BDT molecules (Figure 3.11). Whereas the visible part of the optical reflectivity spectrum is featureless for devices with isolated molecular wires, a new optical transition at $\sim 2.5\,eV$ is observed in aggregated devices at large r-values ($r > 10^{-2}$; Figure 3.11). Moreover this new band was found to be optically active, and gives rise to a PL emission band with maximum at $\sim 1.6\,eV$, upon excitation at $2.5\,eV$. This is taken as evidence that the Me-BDT molecules are indeed aggregated in the 2D SAM devices for $r > 10^{-3}$. The two shoulders α_1 and α_2 (Figure 3.11) may actually probe the bottom and upper limits of the COB density of states in the gap. Remarkably the COB detected by optics (Figure 3.11) has the same width ($\sim 0.5eV$) as the DCS band around $V = 0$ detected by transport (Figure 3.10(b)).

3.3.3 Gap states in Al/SAM/Al devices

3.3.3.1 Optical studies

We measured the optical reflectivity spectra of SAM films on Al electrode with the same r-values as were used for devices with Au substrates (Figure 3.1(a)). In particular for SAM with $r > 10^{-6}$ self-assembled molecular wires on Au (Figure 3.13 red curve) shows a prominent spectral feature at $\sim 280\,nm$ that corresponds to the HOMO-LUMO transition of the isolated Me-BDT molecules on Au substrates. Self-assembled wire molecules on Al substrates, however (Figure 3.13 olive curve), exhibit a blue shift of the HOMO-LUMO

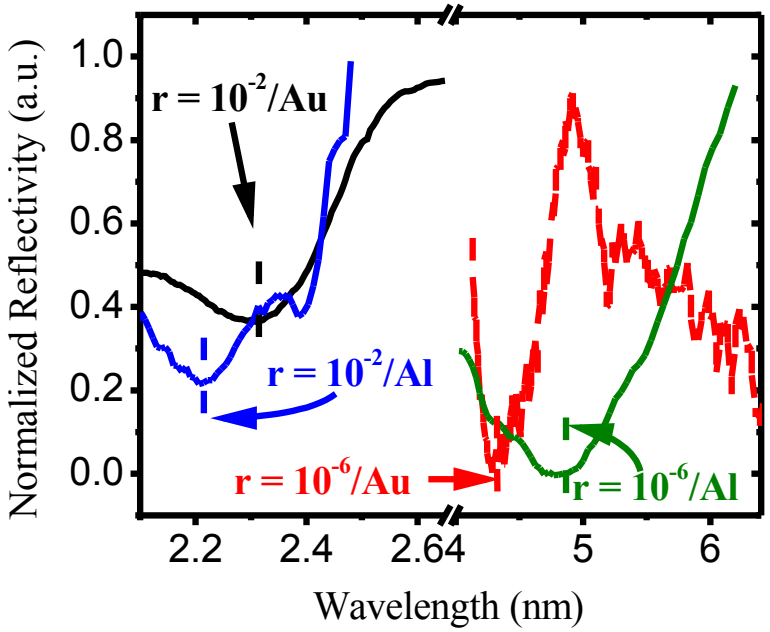

Figure 3.13. Normalized optical reflectivity spectra of SAM films on Au and Al electrodes, respectively, at two r-values: (i) $r = 10^{-6}$ for isolated Me-BDT; and (ii) $r = 10^{-2}$ for molecular aggregates. The Me-BDT HOMO-LUMO transition at $\sim 4.5eV$, and the optical transition related to Me-BDT aggregates at $\sim 2.3\,eV$ are assigned.

transition to $\sim 260\,nm$. This blue shift might be explained by different electrostatic environment for different metallic substrates. SAM films with $r > 10^{-2}$ on Al substrates (Figure 3.13, blue curve) also show a new aggregate-related spectral feature $\sim 560nm$ in the visible spectral range, similar to that on Au substrates. This peak is absent in self-assembled isolated wires on Al substrates. This band is red shifted compared to that of aggregated SAM on Au substrates, which occurs at $\sim 525nm$. We attribute the shift of the aggregate-related band to different macroscopic structure of SAM on these two metallic surfaces. The aggregates may form larger and broader domain and lower energy band on the Al substrates. It is well known that SAM of similar molecules on different substrates may result in different packing [21]. UV and inverse photoemission spectroscopies, as well as XPS studies, would be required to determine the reason for the spectroscopic differences between aggregated SAM on Au and Al electrodes. However we take these experimental facts as an indication of aggregate formation in concentrated SSM on Al substrates, similar to aggregate formation on Au substrates at large r-values.

3.3.3.2 Transport studies

The I-V and dI/dV-V characteristics of the aggregated Al/SAM/Al and Au/SAM/Al diodes at $r > 10^{-2}$ at different temperatures are summarized in Figure 3.14 and Figure 3.15, respectively. All temperature dependent conductivity measurements were performed under a dynamic vacuum to protect against oxidation. Remarkably the I-V curves of aggregated Al/SAM/Al diodes at large r-value (Figure 3.14(a)) seem to be similar to the I-V curves of isolated wires Au/SAM/Au devices seen at small r-value in that the DSC spectra do not reveal a new band at low V (Figure 3.14(b)). This is despite the fact that spectroscopic data do show the existence of aggregate-related COB in the gap. We argue that this seeming paradox is due to the shift of E_F(Al) respect to the COB energy in the aggregates.

It is known from the electrode work function studies that E_F(Al) is shifted respect to E_F(Au) by about $1\,eV$. The energy alignment of Al and COB is depicted in Figure 3.11 inset. It is seen that E_F(Al) is therefore not aligned with the aggregate-related COB in the gap at $V = 0$. As a matter of fact E_F(Al) is above the COB in Me-BDT aggregates. Then ramping V does not result in $E_F(Al) - COB$ crossing at V smaller than that of $HOMO - E_F$ barrier. This situation is similar to textbook examples of transport features seen in inorganic semiconductor structures, when transport is suppressed at some V-range due to lack of available electronic states in the structure at some energy interval, which may lead to negative resistance or negative conductivity devices.

For a control experiment we also compare the transport of aggregated Al/SAM/Al with

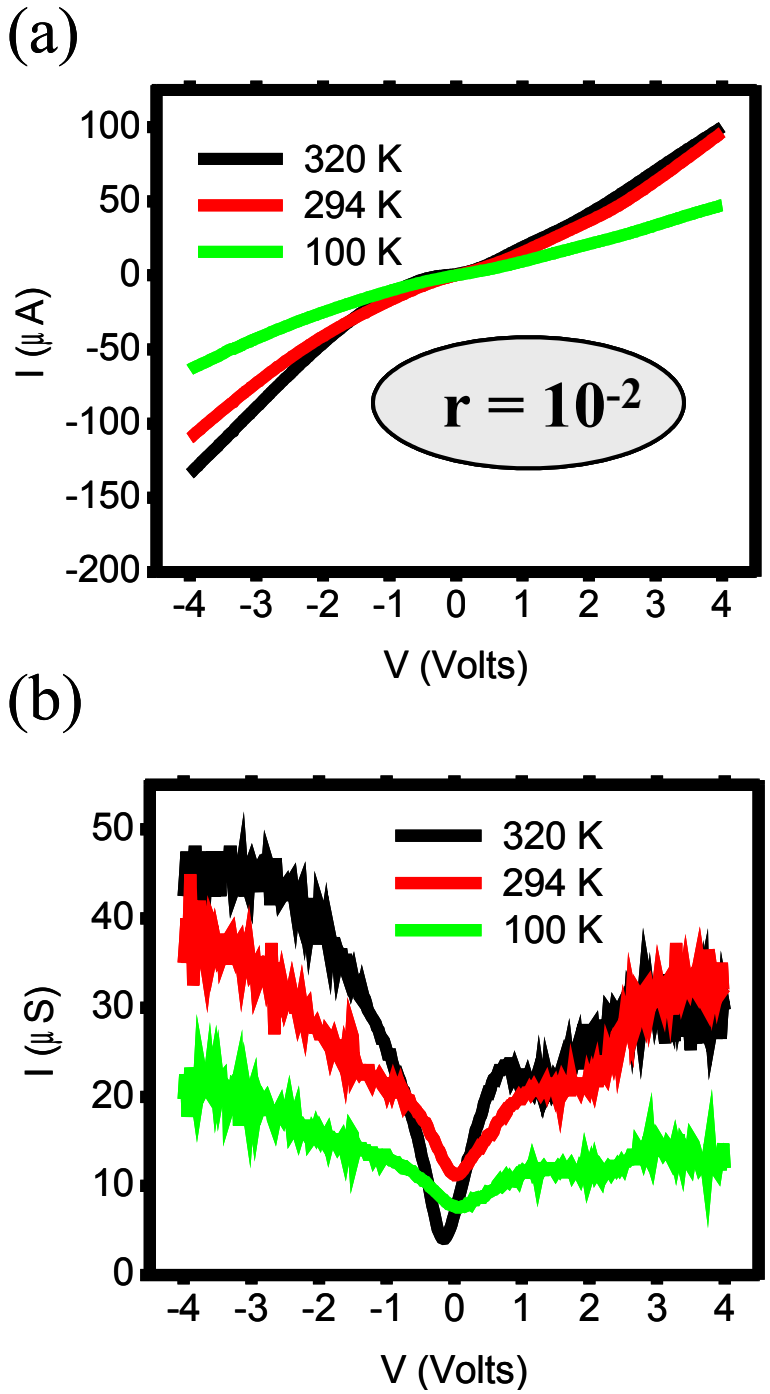

Figure 3.14. Electrical transport measurements of aggregated SAM diodes with $r = 10^{-2}$ with Al electrodes (Al-SAM-Al) at various temperatures. (a) I-V characteristics; (b) differential conductance spectrum obtained from (a).

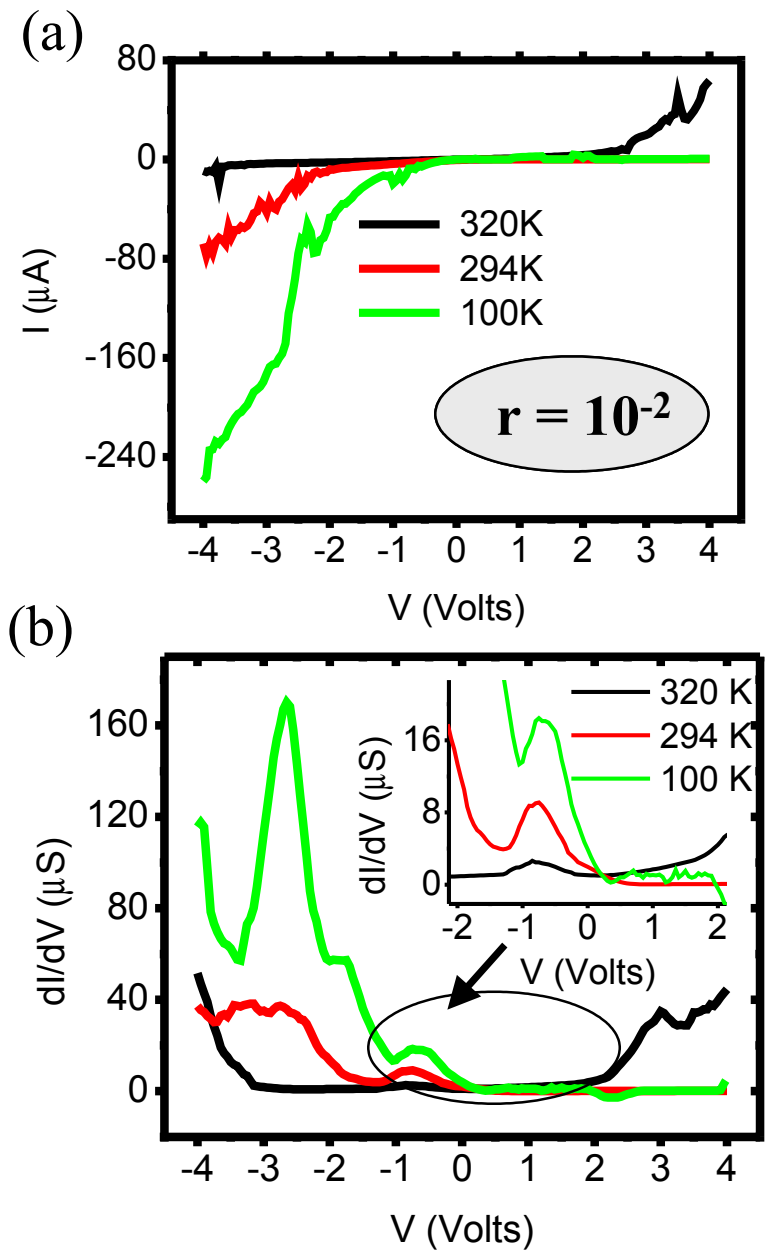

Figure 3.15. SAM diode with bottom Al and upper Au electrodes (Au-SAM-Al). The insert in (b) shows a zoom at low bias

Au(upper)/SAM/Al(bottom) diodes (Figure 3.15). Based on our model above we expect that E_F(Au) would be aligned with COB, whereas E_F(Al) would not. Due to the electrodes' work-function difference we expect a built-in potential of $\sim 1\,eV$ in such molecular diodes. We indeed obtained such asymmetry of the aggregated Au(upper)/SAM/Al(bottom) I-V curve (Figure 3.15(a)) with a "zero shift"of $\sim 1\,V$ with respect to the Au/SAM/Au device. We also obtained a low-energy band in the DCS (Figure 3.15(b)) that is characteristic of COB in aggregated devices when current is injected from the Au electrode ($V < 0$). At the same time we did not obtain such a feature when current is injected from the Al electrode ($V > 0$). This control experiment may serve as evidence that our working model is indeed viable.

3.4 Conclusion

We explored a new molecular engineering approach for fabricating molecular devices based on isolated conducting molecules embedded in a nonconducting molecule SAM matrix. The devices employed a solid-state solution of SAM incorporating both conducting Me-BDT and insulating PT molecules, sandwiched between two Au opposite electrodes. In this configuration the Me-BDT molecules bond to both electrodes, whereas the PT molecules bond only to the bottom electrode, thereby dramatically decreasing their electrical conductivity. Following methods used in Surface Science we employed new tools to confirm connectivity of the Me-BDT with the upper Au electrode, and counted the number of isolated molecular wires in the devices. We expect these methods to be applicable to a wide range of molecular engineering problems.

The electrical transport characteristics of SSM SAM diodes fabricated with different r-values of Me-BDT/PT molecule densities were studied at different temperatures. We found that a potential barrier caused by the connectivity gap between the PT molecules and the upper Au electrode dominates the transport properties of the pure PT SAM diode ($r = 0$). Conversely the transport properties of SSM SAM diodes having r-values in the range $10^{-8} < r < 10^{-4}$ were dominated by the conductance of isolated Me-BDT molecules in the device. The lower limit in this r-value range is determined by the finite conductance of the PT SAM matrix, whereas the upper limit is governed by the formation of Me-BDT molecular aggregates. We found that the temperature dependence of SSM SAM devices is much weaker than that of the PT SAM device, indicating the importance of molecule bonding to both electrodes. From the DCS of the various devices, we found that the energy difference, Δ between the gold electrode Fermi-level and the Me-BDT HOMO (or LUMO)

level is $\sim 1.5\,eV$, compared to $\sim 2.5\,eV$ which we found for the device based on the PT molecules. The smaller Δ value may contribute to the superior conductance of the Me-BDT molecules. We explained the weak temperature dependence of the SSM SAM devices as reflecting the weak temperature dependence of Δ.

We found that the conductance of the fabricated SSM SAM devices scales linearly with r, showing that the isolated Me-BDT molecules simply add together in determining the overall device conductance. Based on this superposition, and the obtained number of active Me-BDT wire molecules in the device we determine the single molecule resistance of Me-BDT to be $R_M = 6 \times 10^9 \Omega$. This value is in good agreement with other measurements using single molecule contact by STM spectroscopy. A simple model for calculating R_M, where the transport is governed by electron tunneling through the Me-BDT molecule using the WKB approximation is in good agreement with the experimental data, and thus validates the protocol followed in the present studies.

We also studied SAM diodes based on two-component solid-state mixtures of molecular wires (Me-BDT) and insulators (PT) at various molar ratio, r. This approach enabled fabrication of molecular devices with 1D response at low r-values ($r < 10^{-4}$) where the isolated molecular wires dominate transport [48]; along with devices based on 2D response at higher r-values ($r < 10^{-3}$), where the Me-BDT molecules form SAM aggregates. The electrical transport characteristics of SAM diodes fabricated with various electrodes were investigated via I-V and DCS dependencies on V, at various temperatures, and by optics, including UV-Vis absorption and PL emission spectra.

The transport characteristics properties of 2D molecular diodes at high r-value are modeled within the weak charge delocalization approach. We postulate the existence of new gap states in the Me-BDT HOMO-LUMO gap that form a continuum of band (COB) due to the aggregation, at $\sim 2\,eV$ above the HOMO level. The aggregate-related COB is formed in the gap in the vicinity of the gold Fermi level. This model explains the low energy features in the I-V and dI/dV-V spectra of Au/SAM/Au diodes, as well as the new absorption bands and PL emission band.

To verify our working hypothesis we also studied SAM diodes based on Al and Al-Au electrodes combination. The difference in the work-function values between Au and Al metals is $\sim 1\,eV$, and thus it is expected that a corresponding difference in E_F between these two metal electrodes with respect to COB should influence the device transport response. We indeed found that the transport features that were attributed to COB in Me-BDT aggregates in Au/SAM/Au diodes disappear in Al/SAM/Al diodes, but the optical

features related to the Me-BDT aggregates still remain. Transport properties of the mixed Au/SAM/Al devices at large r-values also show the low voltage I-V and DCS features, which are characteristic for COB in the gap only when current is injected from the Au electrode, but are not seen when the current is injected from the Al electrode. We believe that E_F(Al), being higher than E_F(Au) does not cross the aggregate-related COB in the gap when the bias voltage is ramped up, and this explains the puzzle in the transport properties of Al/SAM/Al devices. We note that the low voltage aggregate-related response in SAM diodes is not unique to Au electrodes. In fact we obtained similar transport response also in Co/SAM/Co diodes, in which $E_F(\mathrm{Co}) \sim E_F(\mathrm{Au})$.

CHAPTER 4

BULK HETERO-JUNCTION ORGANIC PHOTOVOLTAIC DEVICE PHYSICS

In this chapter, we will be examining the underlying physics in bulk hetero-junction Organic photovoltaic devices (B-OPV). We shall present our input on one of the controversies in the field, namely, the origin of open voltage circuit (V_{oc}).

4.1 B-OPV I-V characteristics

4.1.1 General mechanisms in B-OPV

4.1.1.1 Absorption of solar radiation

Upon illumination of an OPV, photons are absorbed in the active layer both by the donors and acceptors; these absorbed photons are the ones responsible for the generation of carriers. This implies that for high photon absorption, it is not only imperative that the blend's absorption spectrum matches the solar spectrum, but also there is a need for a high optical density for these materials at all ranges of the spectrum. Figure 4.1 shows the absorption of the P3HT:PCBM blend compared with the solar illumination, AM 1.5. Based on the match between the blend and the solar spectrum, it is possible to calculate the highest possible efficiency achievable with B-OPVs as presented below. If we consider the sun as a blackbody, we know from Planck's law that the energy density in an elementary region of the spectrum $d\lambda$ is given by:

$$E_\lambda = \frac{C_1}{\lambda^5[exp(C_2/\lambda T) - 1]} \tag{4.1}$$

where C_1 and C_2 are, respectively, the first and second Planck's radiation constant with values $C_1 = 3.74 \times 10^{-16} m^2 W$, $C_2 = 0.0144 mK$. T is the absolute temperature of the blackbody. The total energy emitted by this blackbody is thus given by the integral of equation 4.1

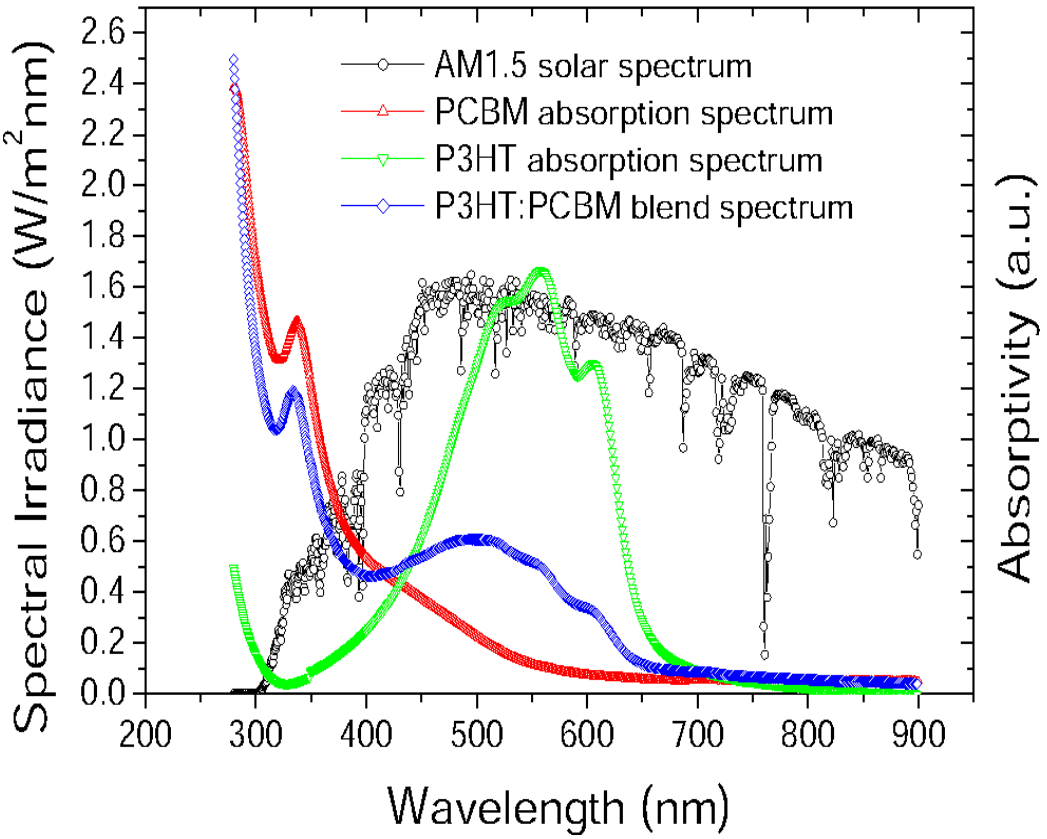

Figure 4.1. Comparison of the absorption spectra of the active components with the AM1.5 solar spectrum.

$$E_{0-\lambda} = \int_0^{\lambda} E_{\lambda} d\lambda \tag{4.2}$$

This can be transformed to:

$$E_{0-\lambda} = \int_0^{\lambda T} \frac{C_1 d(\lambda T)}{\sigma(\lambda T)^5 [exp(C_2/\lambda T) - 1]} \tag{4.3}$$

where σ is the Boltzmann constant. The value of this integral is the fraction of the blackbody energy between zero and λT, and has been calculated by [50] for convenient intervals, as presented by Duffie and Beckman [51]. If the sun is assumed to be a blackbody at 5777 K, the fraction of energy between zero and the red edge of the visible spectrum $\lambda T = 0.78\mu m \times 5777K = 4506\mu mK$ is 56%. In a P3HT:PCBM blend, as seen from Figure 4.1, P3HT's absorption edge is at about $0.68\mu m$. The fraction of energy in the absorption range is therefore about 46%. PCBM has no appreciable absorption above $0.55\mu m$, and the fraction capable of generating electron-hole pairs is therefore about 32%. Hence, the maximum possible power efficiency achievable for a P3HT:PCBM blend is about 46%. It should be noted however that this is obtained with the assumption that the absorbance is 100% at all wavelengths, which is hardly the case.

4.1.1.2 Exciton generation

Only photons with energy greater than or equal to the band gap of the blend's material can excite an electron across the gap. Photons with energy smaller than the band gap are just transmitted through and do not count towards the generation of electron-hole pairs (EHPs) in the device. We assume that each photon absorption leads to the generation of only one electron hole pair. Even though multiple exciton generation from just one photon has been reported in some materials, it is very unlikely in the polymer blends studied here that one photon absorption leads to the generation of several electron hole pairs. For this to take place, it is necessary that the photon's energy be more than twice the band-gap energy. Photons with energy higher than the band-gap in our systems after absorption generally lead to energy dissipation in the lattice, leading to an increase in temperature of the OPV device.

4.1.1.3 Separation of electrons from holes

Once the exciton is created, there is a need for it to separate in order to have free electrons and holes. For this, the exciton diffuses to the interface between the donors and the acceptors. It is critical for this to happen because exciton separation in the donor or the acceptor is negligible, as the small exciton will most likely recombine. At the interface,

the electron would reside on the acceptor and the hole on the donor. It is still not clear what causes the exciton separation at the interface; some believe the exciton dissociation is caused by the dipole-dipole interaction between the donor and the acceptor, and others believe it is due to $V_{built-in}$ caused by the difference in work function between the two electrodes. It is important to note that the majority of excitons generated in the blend are singlet excitons with lifetime of the order of few nanoseconds. This implies that the exciton diffusion length $L = \sqrt{D\tau}$ is small compared to triplet excitons who have a lifetime of the order of a microsecond. So for effective carriers generation, it is important to work with materials with a larger exciton diffusion length. In the case of a blend or a B-OPV, the optimization of the exciton diffusion comes from the high level of intermixing of the donor and the acceptor, as this leads to higher interfaces.

4.1.1.4 Electron-hole transport

Once the excitons are separated into electrons and holes, they need to be transported to the electrode. At this stage, the carrier mobility is critical. The higher the mobility, the better the transport. It is however important to strike a balance between the high mobility and recombination. Once the carriers are separated, they can only recombine by means of a bimolecular process or a langevin type recombination. In this framework, Braun[52] proposed that the recombination rate is given by:

$$k_r = \frac{q}{\langle \varepsilon \rangle} \langle \mu_n + \mu_p \rangle \tag{4.4}$$

As could be seen in Equation 4.4, with increasing mobility, the recombination rate is increased as well. Thus higher mobility leads to faster recombination; in this case, phase separation between electron and hole is very important.

4.1.2 Loss mechanisms in B-OPV

4.1.2.1 Optical losses

Some of the photons that impact the device are lost via a number of processes:

4.1.2.1.1 Reflection losses. When illuminating the device, part of the light beam can be reflected by the electrode. While reflection from the bottom electrode will lead to "double absorption by the device", reflection from the upper electrode is detrimental. For this reason the electrode is chosen to be as transparent as possible in order to minimize this type of losses. This also accounts for why the bottom electrode should be as thick as possible to allow for double absorption. It is possible as well to have some reflection at the interface organic-metal, especially the upper electrode interface with the organic. If this

electrode is ITO as is usually the case, then the reflection is mainly due to the refractive index mismatch between air and the organic. However, the organic refractive index being higher than the air's, there is therefore no critical angle and thus very little Fresnel losses.

4.1.2.1.2 Unabsorbed photons. There are two possible losses at this level:

- Losses due to the mismatch between the solar spectrum and the band structure of our active layer. Photons with energies higher than the HOMO-LUMO gap of the active layer will see their excess energy go to thermalization of the hot carriers as stated in the previous section. Photons with energy lower than the HOMO-LUMO gap will not be absorbed at all.

- Due to inappropriate active layer thickness, it is possible to lose some photons. The active layer can be too thin such that some photons will just go through the device unabsorbed. However, an active layer that is too thick can also be detrimental as we will see below; this can induce a high series resistance or can increase the distance an exciton will have to travel before getting to the interface.

4.1.2.2 Exciton diffusion and dissociation

Exciton can diffuse in two ways in the active layer as seen in Figure 4.2. The Dexter type transfer is a short range (0 to $2nm$) transfer that occurs when there is an overlapping of the electron cloud between two molecules of the same type. The only physical parameter conserved in this transfer is the spin; the transfer decays exponentially with the distance. The other transfer type is the Förster transfer type. This transfer is due to dipole-dipole interaction between adjacent molecules of the same kind and spin is conserved under the condition imposed by the allowed dipole transition between the molecules. This transfer is long range (3 to $10nm$).

Each of these transfer processes is limited by bimolecular recombination that can reduce the exciton diffusion yield. Molecules in bulk hetero-junction generally form aggregates which lead to a formation of new allowed and forbidden transitions. There are two kinds of aggregates of molecular systems as shown in Figure 4.3: J aggregates and H aggregates. In J aggregates, the dipole alignment is top to bottom resulting in summation of the dimers moments leading to an allowed transition towards the lower level with exciton formation. This aggregate can also lead to a forbidden transition towards the higher level with exciton formation; this is the result of the dimer moments zeroing each order.

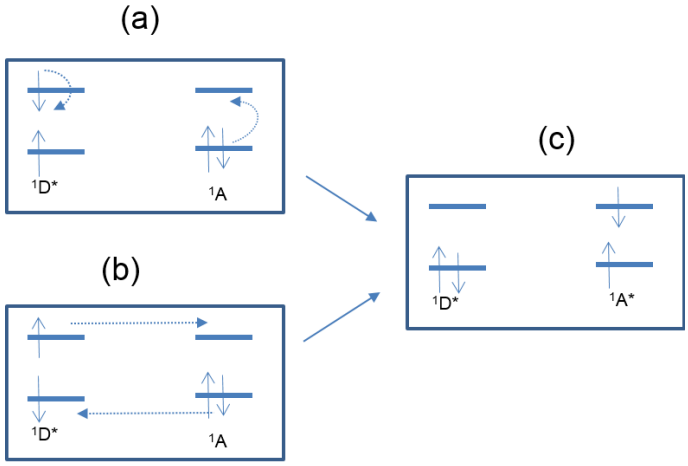

Figure 4.2. Schematic description of Dexter exciton transfer (a), Förster exciton transfer (b) and the result of exciton transfer.

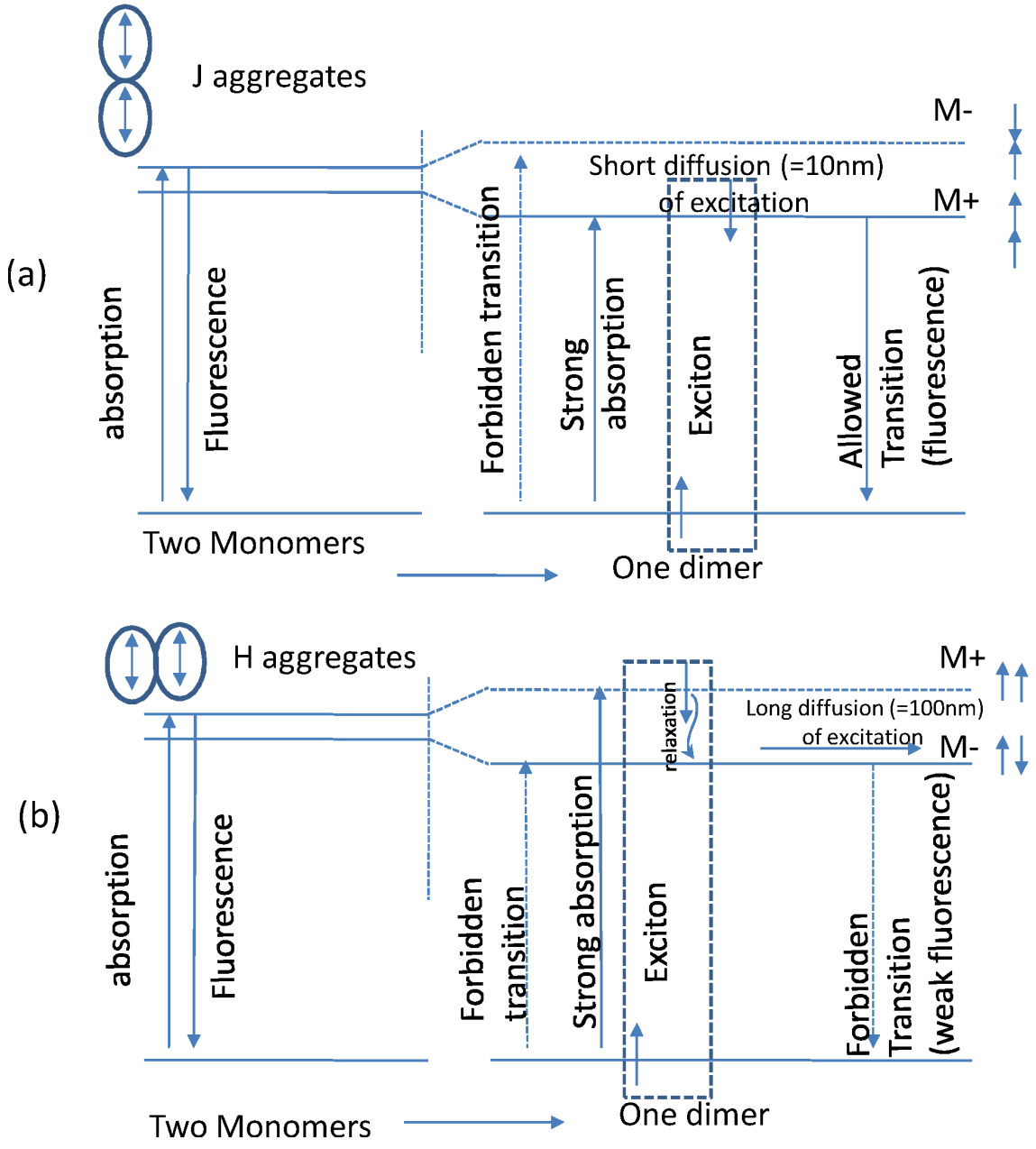

Figure 4.3. Aggregates configuration and their respective allowed and forbidden transitions (a) J aggregate (b) H aggregate.

The H aggregates, on the other hand, result from the dipoles being parallel to each other. They differ from the J aggregate in that the allowed transition is now the high level and the forbidden the lower level.

Consequently, in J aggregates, transition to the ground state is allowed, which leads to high luminescence throughput thus easy exciton recombination. Here the exciton diffusion length is small and so not suitable for the photovoltaic effect. In the H aggregate, however, following relaxation from the high level to the lower one, luminescence becomes weak as the transition to the ground state is now forbidden. In this system, the exciton diffusion length is around $100nm$, which is advantageous for the photovoltaic effect.

For charge transfer or exciton dissociation to occur in bulk hetero-junction, it is imperative that the difference between the donor ionization potential (I_{PD}) and the acceptor electron affinity (χ_A) be greater than the exciton energy $I_{PD} - \chi_A\ E_{ex}$. The efficiency for charge transfer is $\sim$ 100% as the exciton dissociation occurs within a few hundred femtoseconds.

4.1.2.3 Electrical losses

The electron and hole that are generated in the donors and acceptors need to be transported to the respective electrodes (anode for the hole and cathode for the electron). This transport can be hindered by the presence of traps in the blend. Shallow traps can affect the carriers' mobility while deep traps can affect the number of carriers collected at the electrodes. Consequently, the current will be reduced by the presence of traps in the blend.

It is critical to have a match between the electron, and the hole mobility as a mismatch can lead to the creation of an internal electric field that may counter the driving electric field and thereby reduce the overall current. An ohmic contact is equally critical for carrier collection by the electrodes. A nonohmic contact can increase carrier accumulation in the device, thereby increasing the series resistance, which in turn can increase recombination in the device.

4.1.3 I-V characteristics of B-OPV

4.1.3.1 Modeling the dark current

The I(V) characteristics in the dark are the result of the superposition of bulk transport mechanisms with electrical properties of the organic electrode interface. In general, the I-V characteristics are interface dependent at low voltage and bulk dependant at high voltages. In the bulk, as derived in Chapter 2, we are in the framework of space charge limited current

(SCLC), where the current is given by the Mott-Gurney law, yielding a current proportional to V^2d^3. More precisely, the presence of trap in the system puts us in the trap space charge limited current, which leads to the current being proportional to $V^{m+1}d^{(2m+1)}$, where m is a parameter which characterizes trap distribution. Figure 4.4 represents what should be expected from the dark current in a B-OPV with the different transport regimes.

The I-V characteristic in the dark can be derived in a macroscopic way, treating the active layer as a diode. From Figure 4.5(a) we can see that in series with the diode, there is a resistance R_s which can be regarded as the sum of the resistance of the active layer and the other layers in the devices. R_{sh} is the shunt resistance representing all leakage sources in the device. These sources can be illumination dependent like recombination. In the dark, we have carriers injection into the device, so recombination of injected carriers could be different from photo-generated carriers. Based on the equivalent circuit in Figure 4.5(a) we get the dark current as:

$$I_{dark} = I_0[exp(\frac{eV}{nkT}) - 1] - \frac{V - R_sI}{R_{sh}} \tag{4.5}$$

where V is the applied voltage, n is the ideality factor.

4.1.3.2 IV characteristic under illumination

Under illumination the equivalent circuit can be modified by adding a current source $I_{photo-generated}$ (Figure 4.5 (b)). The I-V is thus given by:

$$I_{dark} = I_0[exp(\frac{eV}{nkT}) - 1] - \frac{V - R_sI}{R_{sh}} - I_{photo-generated} \tag{4.6}$$

This expression however presents a problem as pointed out by C. Waldauf [53, 54]. There are some discrepancies while fitting the above I-V characteristics to experimental data. In fact in order to fit the I-V under variable illumination, it was necessary to change the value of I_0 even though the only parameter that is changed under variable illumination is $I_{photo-generated}$ (Figure 4.6).

In the analysis, it was noted that at V = O, the carrier's drift length in the device is given by:

$$d_{drift} = \mu\tau\frac{V_{bi}}{L} \tag{4.7}$$

where μ is the carrier's mobility, τ carrier's recombination time, $V_{built-in}$ is the built-in voltage, and L is the device thickness. If the drift length is smaller than the thickness of the sample, just the fraction $\frac{d_{drift}}{L}$ will reach the contacts and can be extracted from the device. The above equation suggests that $I_{photo-generated}$ in equation 4.6 should be considered as voltage dependent.

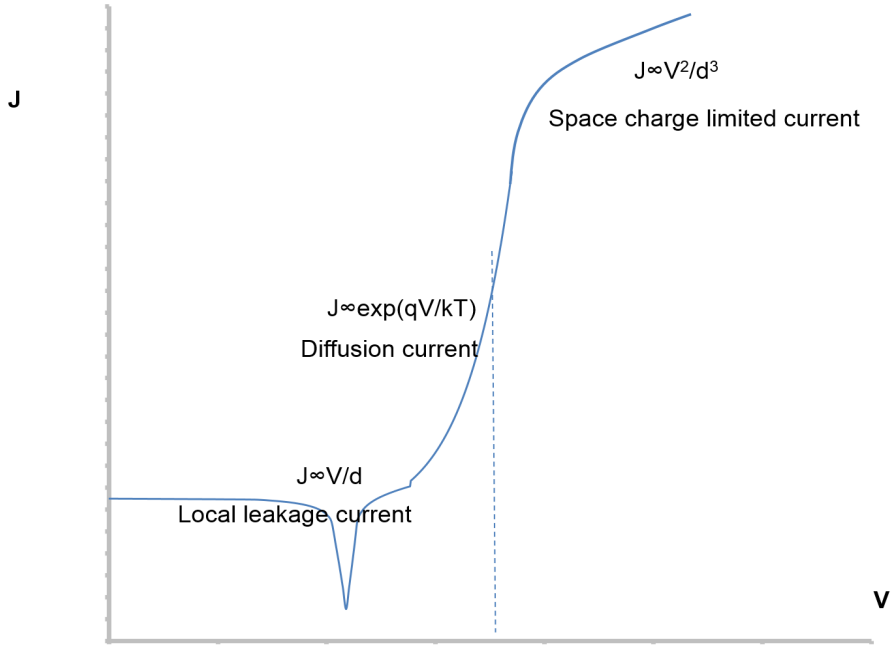

Figure 4.4. I-V in the dark with the different transport regimes.

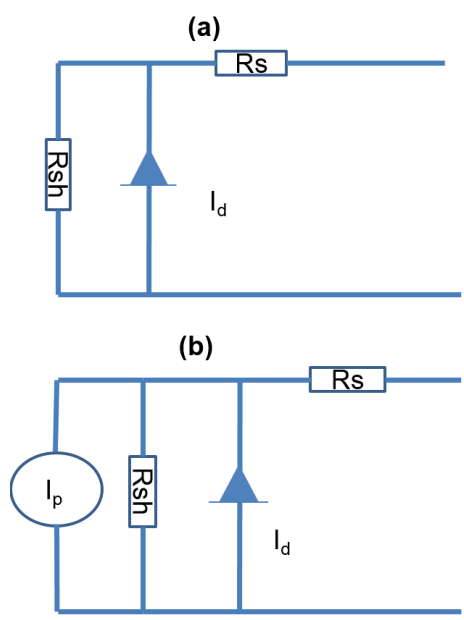

Figure 4.5. Equivalent circuit (a) In the dark (b) Under illumination.

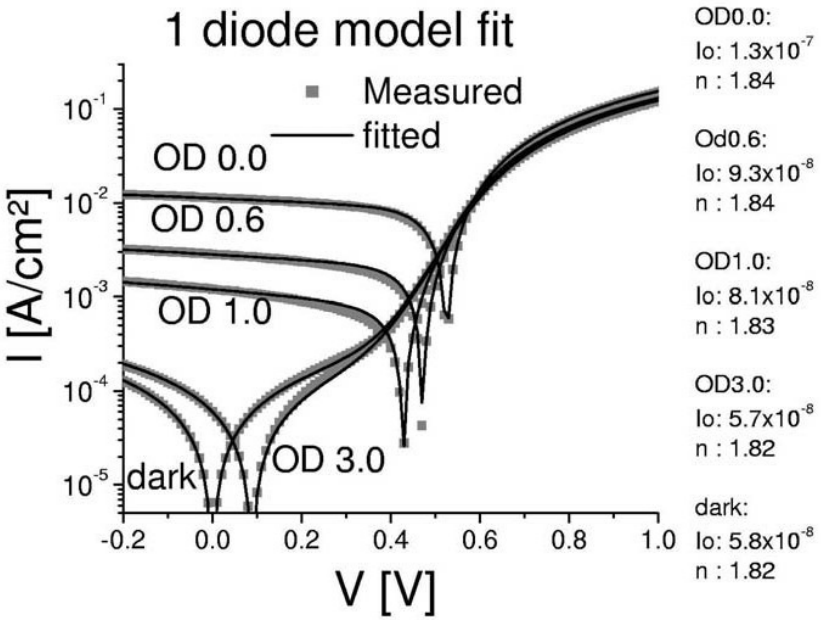

Figure 4.6. IV- curves of a bulk hetero-junction solar cell measured under different illumination intensities (boxes) with fitted curves using the standard 1-diode-model (lines). Values for the parameters n and I_0 are given for each light intensity in the legend. The light intensity is given by the value of the optical density (OD) of the various grey filters and the light intensity of 110 $mWcm^2$ at $OD = 0$.

Assuming a homogeneous generation of carriers through the entire bulk, and a constant mobility and recombination time for all carriers, the photo-generated current is then rewritten:

$$I_{photo-generated} = \begin{cases} -|I_{sc}| & if\ (V_{bi} - V) > 0\ and\ \mu\tau\frac{V_{bi}-V}{L} > L \\ |I_{sc}| & if\ (V - V_{bi}) > 0\ and\ \mu\tau\frac{V-V_{bi}}{L} > L \\ I_{sc} \times \mu\tau\frac{V_{bi}-V}{L^2} & if\ \mu\tau\frac{|V-V_{bi}|}{L} > L \end{cases} \tag{4.8}$$

As can be seen from this equation, the photo-generated current is voltage dependent and takes into consideration the change in drift length as the bias voltage is changed. Figures 4.7 and 4.8 show the experimental data fitted using this model. Remarkably, there is no need to readjust I_0 for every illumination.

The most critical feature of Equation 4.8 is that it is impossible for the photogenerated current to be independent of the applied voltage. This is because the carrier drift length is not voltage independent.

From Equation 4.8, it is obvious the I-V characteristic can be influenced by parameters such as the active layer thickness (L), the product mobility and recombination time ($\mu \times \tau$), the illumination intensity which is proportional to the shut circuit current (I_{sc}),etc.

4.1.3.3 Active layer thickness influence on I-V under illumination

Figure 4.9(a) is a simulation based on Equation 4.8 that shows the influence of the device thickness on the I-V characteristics. As expected, the short circuit current varies with the thickness; this is due to the fact that by increasing the thickness of the active layer, we reduce the amount of carrier collected at the electrode as the transit time becomes longer than the recombination time. Figure 4.9(b) shows that the fill factor also does not remain constant; it decreases due to the reason given above. The shunt resistance can also be perceived as the slope of the IV when the bias voltage is close to zero. This is a measurement of the current leakage in the device; thus it is a measurement of carriers recombination and deep trapping. An increase in shunt resistance represents a decrease in recombination. With this in mind it becomes clear why the fill factor decreases with increasing thickness. Since the drift length is inversely proportional to the device thickness $d_{drift} = \mu\tau\frac{V_{bi}}{L}$, an increase of the thickness will therefore mean a decrease of the drift length. It becomes difficult for carriers to reach the electrode since recombination takes over. This leads to a decrease in shunt resistance which means a decrease in fill factor. The effect on the open circuit voltage will be examined in section 4.3

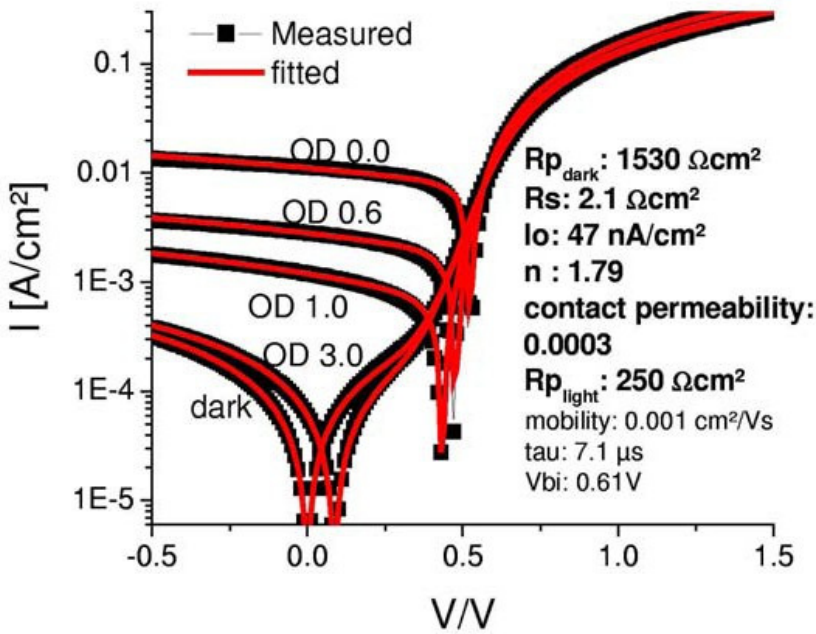

Figure 4.7. I-V under various illumination intensities fitted with the corrected model.

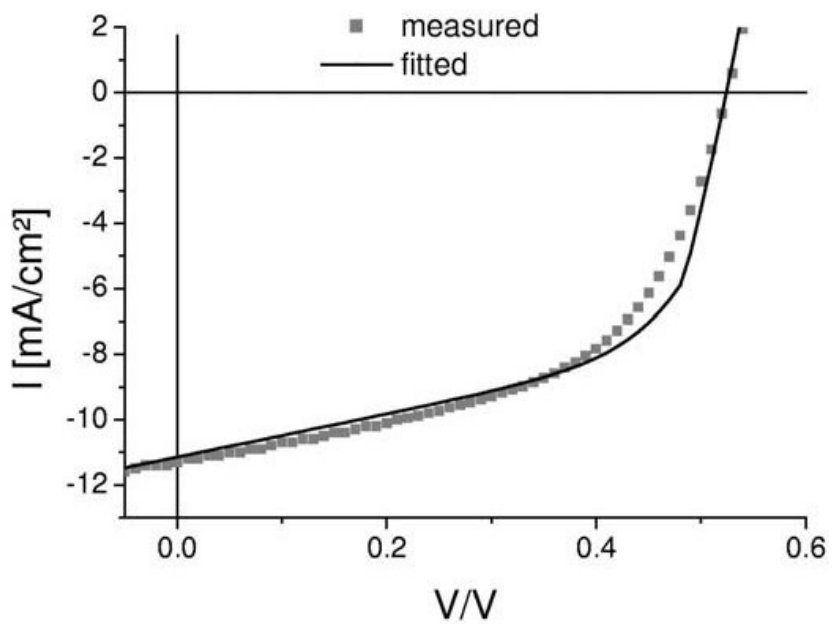

Figure 4.8. I-V under illumination fitted with the corrected model.

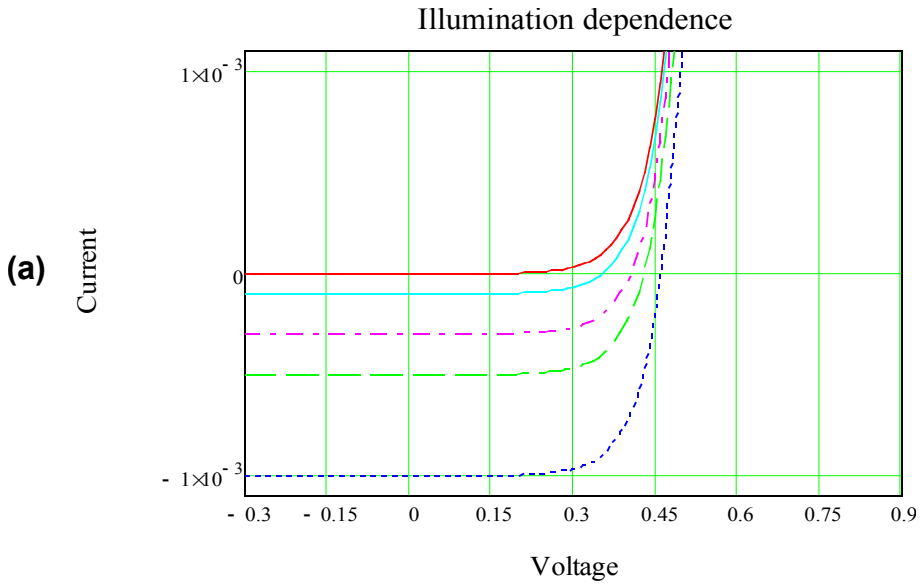

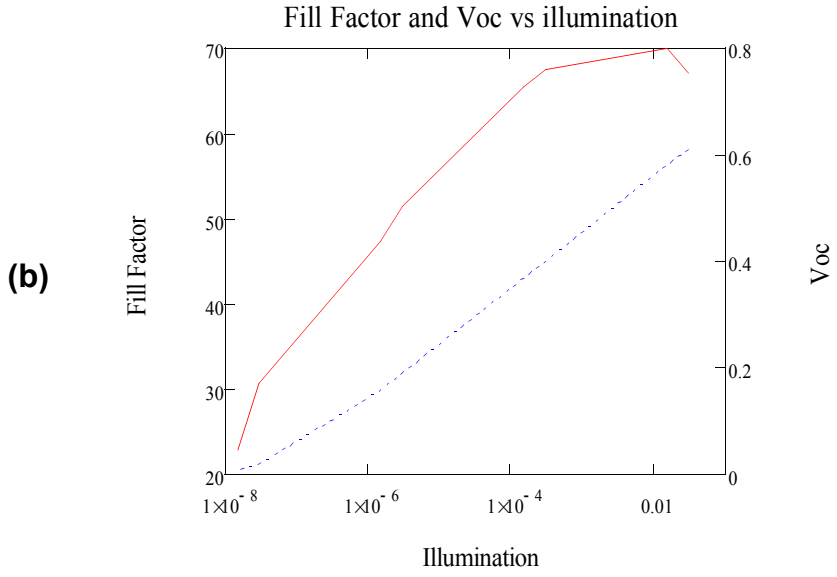

Figure 4.9. Simulation of active layer thickness influence on I-V under illumination (a) I-V characteristic (b) FF and V_{oc} as a function of active layer thickness.

4.1.3.4 $\mu \times \tau$influence on I-V

We could increase the drift length by increasing the product $\mu \times \tau$. However this will only become noticeable on the fill factor once the drift length becomes higher than the device thickness. Figure 4.10(a) shows how the I-V changes by varying the product $\mu \times \tau$. In this simulation the active layer thickness was taken to be $100nm$ and we can see from Figure 4.10(b) that a drastic increase in FF occurs when the product $\mu \times \tau$ becomes larger than L as expected.

4.1.3.5 Illumination intensity effect on I-V

Figure 4.11(a)represents the illumination intensity effect on the I-V characteristics; Figure 4.11(b) shows its influence on the fill factor. While the fill factor is constant at low illumination power, its value decreases drastically once we go past a certain value. In the framework of space charge limited current, this is understandable as an increase in illumination means an increase in injection rate. When the injection rate goes beyond the transit or extraction rate, we start having carriers accumulation in the device which leads to an increase in the recombination rate, thus the decrease of the fill factor.

4.2 Towards a high efficiency B-OPV

To achieve a high efficiency B-OPV device, we examined the effect of several important parameters.

4.2.1 Series resistance optimization

The device series resistance is a summation of the resistance of each layer that makes up our device. Apart from the active layer, the other layer that has some critical effect on the series resistance is the PEDOT layer. As seen in Chapter 2, PEDOT is commercialized in two forms by H.C Stark, high conductive form and a low conductive form. The low conductivity form of PEDOT is suitable for OLED where carriers extraction is not necessary, while the high conductivity PEDOT is made for solar cell applications. We anticipate that the high conductivity PEDOT should yield a higher device efficiency while the low conductivity should show a lower efficiency. This effect was studied by fabricating OPVs with each of these PEDOT layers. Figure 4.12 summarizes what was observed. As expected, PEDOT conductivity mainly has an effect on the series resistance of the device. From the observed change in I_{sc} and fill factor, we deduce that the series resistance is not independent from the shunt resistance. This is because an increase in series resistance will lead to carriers

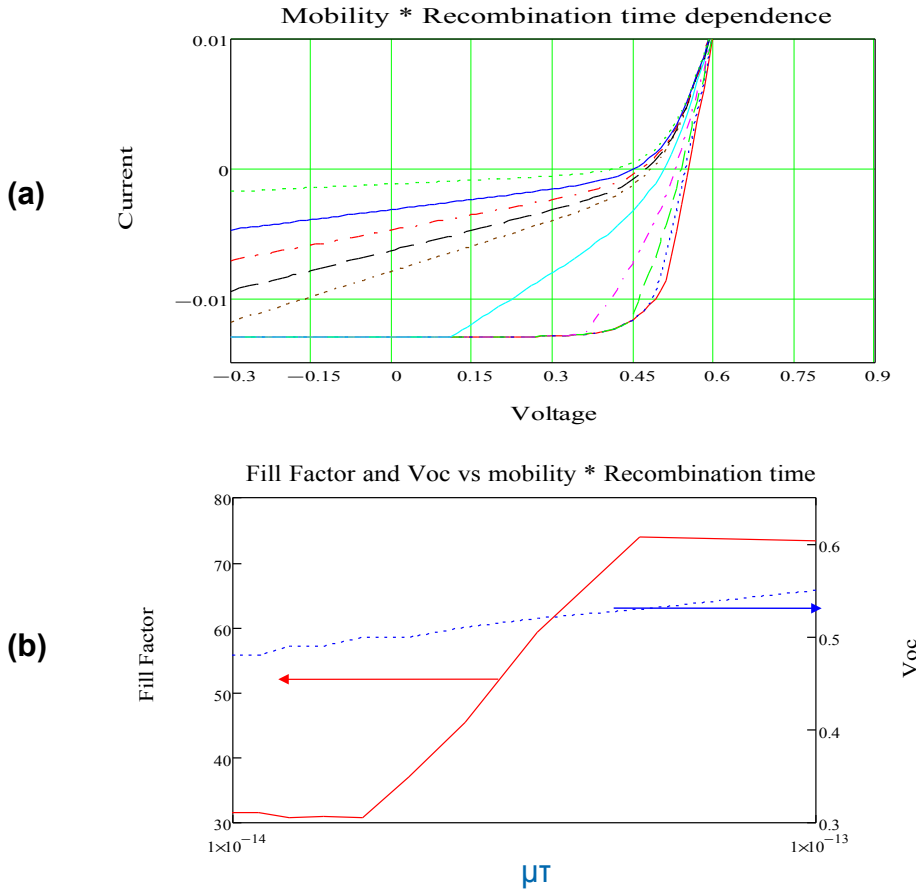

Figure 4.10. Simulation of $\mu \times \tau$ influence on I-V (a)I-V characteristic (b) FF and V_{oc} as a function of $\mu \times \tau$.

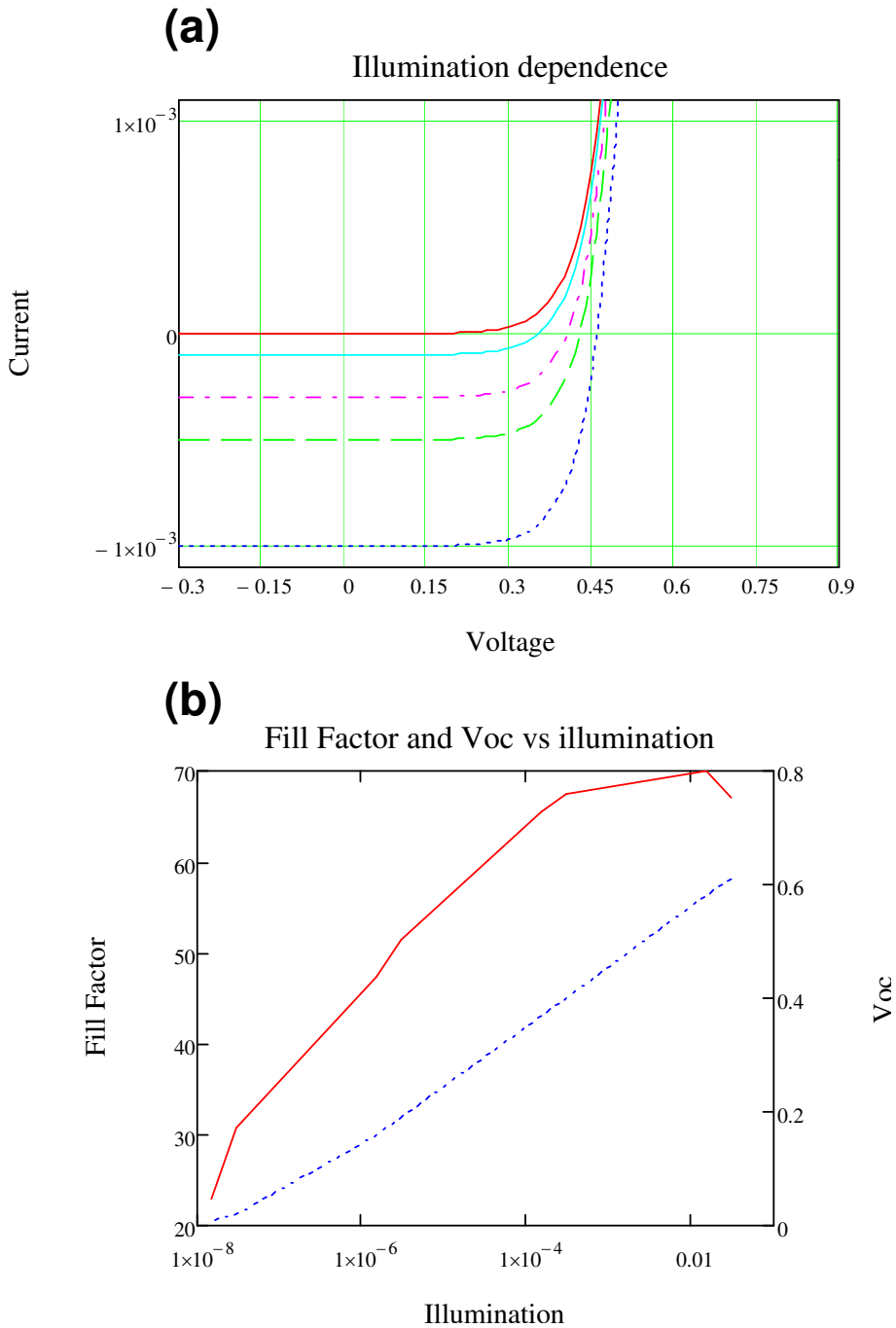

Figure 4.11. Simulation of illumination power influence on I-V (a) I-V characteristic (b) FF and V_{oc} as a function of illumination power.

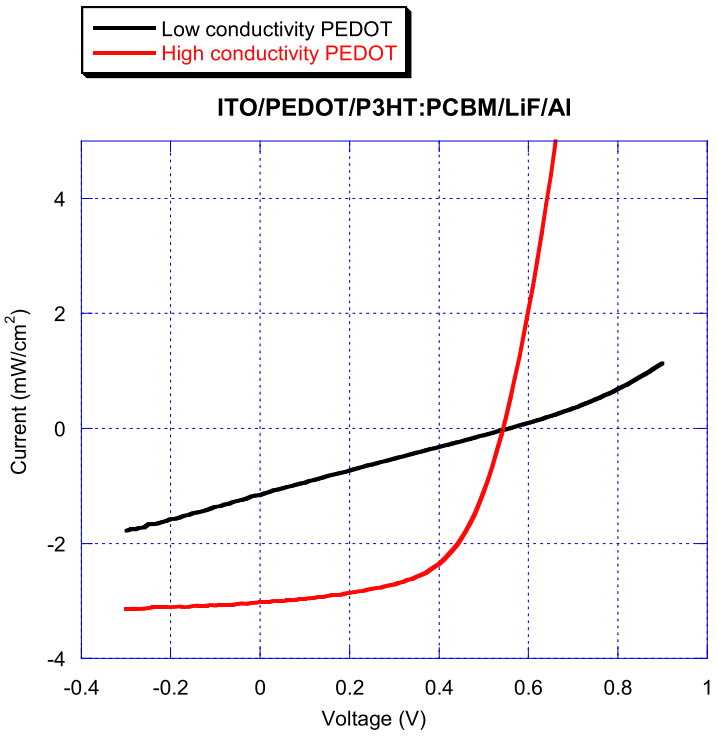

Figure 4.12. I-V characteristics of devices with different PEDOT conductivity.

accumulation in the device, which in turn will lead to an increase in recombination rate, thus the decrease in shunt resistance and short circuit current.

4.2.1.1 Device thickness

To confirm the influence of the active layer thickness on the I-V, we fabricated two devices: one with an active layer thickness of 130 nm and another with a thickness of 80 nm. The variation in thickness was obtained by changing the spin coating speed. For 130 nm, we spin-coated at 1500 rpms while 80 nm was obtained by spin-coating at 2500 rpms. From Figure 4.13 it is obvious that the recombination effect is more critical at this thickness level than the effect due to photon absorption. From the previous section, we showed that an increase in thickness should result in an increase in photon absorption thus an increase in photogenerated carriers. However just as we cautioned, this increase becomes detrimental once the device thickness becomes higher than the carriers drift length.

4.2.1.2 Contact with the electrode

The effect of the contact electrode will be studied in depth in the next section. We however would like to show that to optimize contact with electrode and prevent hole injection in the device, Lithium Fluoride (LiF) is often used. Figure 4.14 shows its effect.

4.2.2 Best B-OPV device obtained

After optimizing the above parameters, we have been able to achieve a 4.1% power efficiency under AM1.5 ($100mW/cm^2$). This was obtained using P3HT purchased from Rieke Metals with 93% regio-regularity; PCBM was purchased from ADS. A blend of these two 1.2 : 1 (P3HT:PCBM) was made with about $16mg/ml$concentration of P3HT. For this, we used as electrode $1.2nm$ of LiF, $10nm$ of Magnesium (Mg) and $60nm$ of Aluminium. The device active area was $0.2 \times 0.3cm^2$. The device yielded a short circuit current of $\sim 13mA/cm^2$, an open voltage circuit of ~ 0.55 V and fill factor of 57%. Figure 4.15 shows the obtained I-V characteristics.

We obtained a modified PCBM molecule from Plextronics that was dubbed Jalapinos. Devices fabricated with this acceptor gave us 4.92% power efficiency at $80mW/cm^2$. The obtained I-V characteristics (Figure 4.16) shows that the main parameter that was changed by the use of Jalapinos is the V_{oc} that went from $0.55V$ for the nonmodified PCBM to $0.72V$ for Jalapinos. It is worth mentioning that Plextronics holds the record for the highest efficiency in single active layer bulk hetero-junction solar cell with 5.4% efficiency[55].

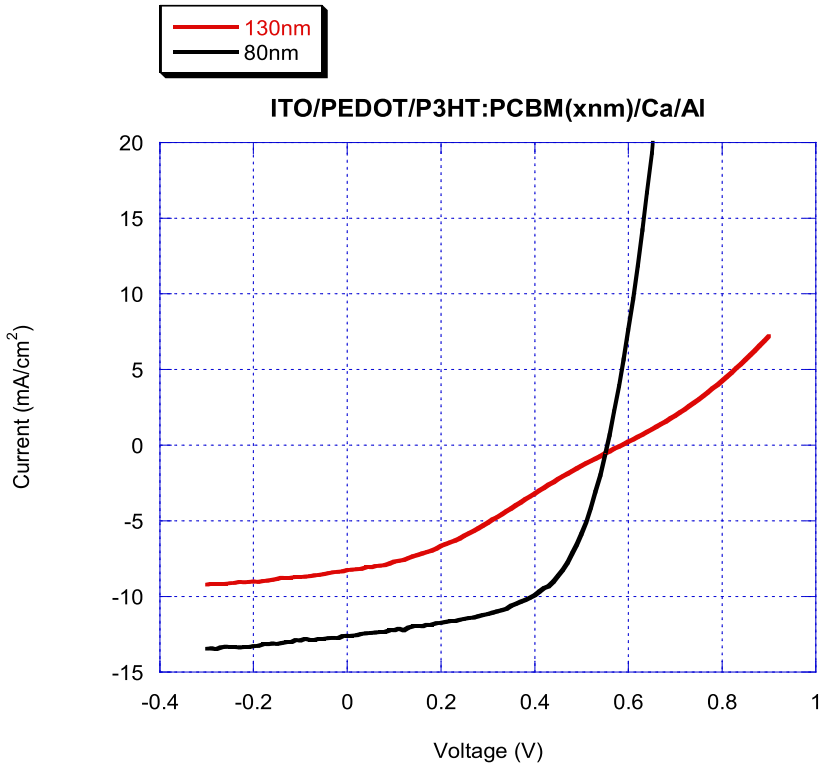

Figure 4.13. I-V characteristics of devices with different active layer thickness.

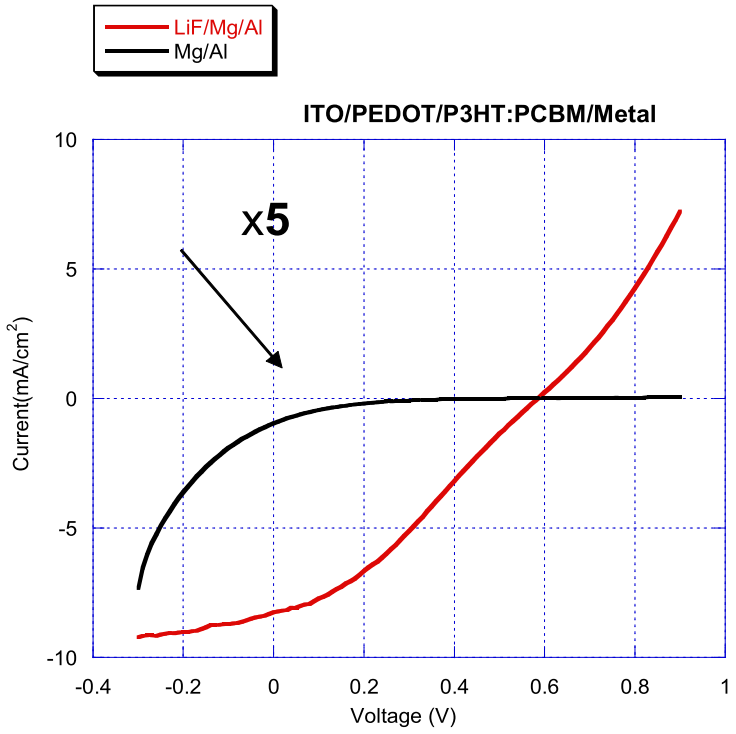

Figure 4.14. I-V characteristics of devices with and without LiF.

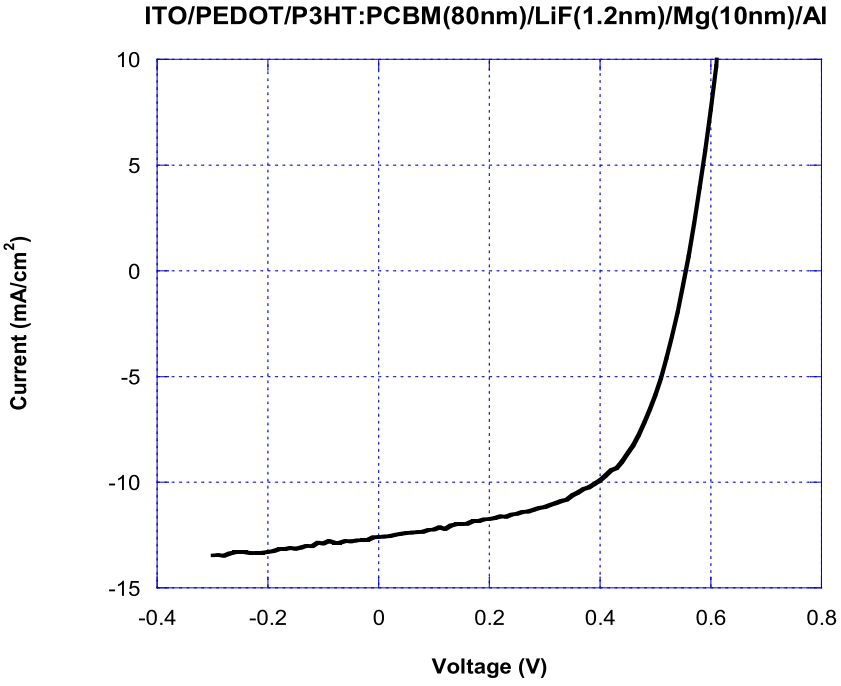

Figure 4.15. I-V characteristics the best device obtained with P3HT:PCBM.

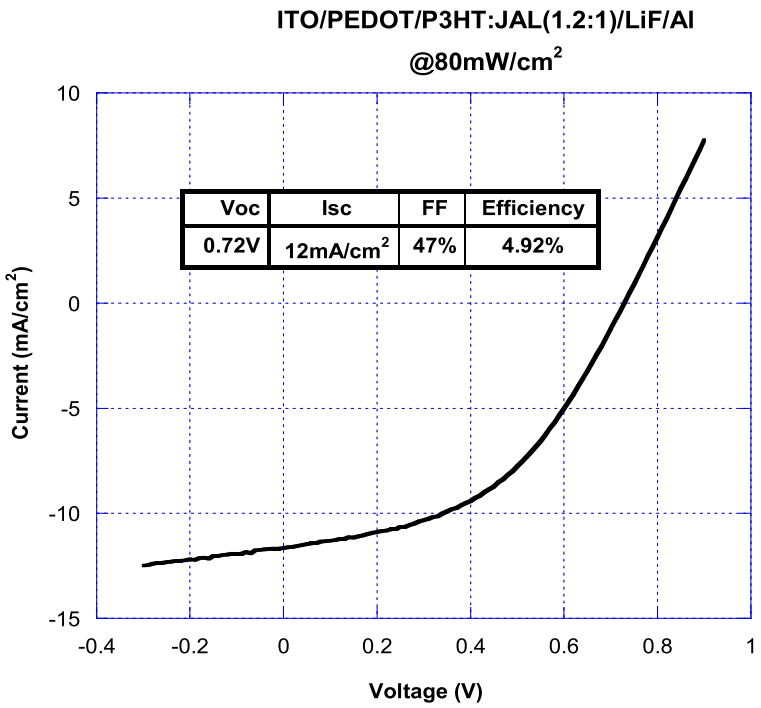

Figure 4.16. I-V characteristics of the best device obtained with P3HT:JAL; the insert is a table of the obtained parameters.

4.3 Origin of V_{oc}

4.3.1 Introduction

The B-OPV power efficiency essentially depends on three parameters: the short circuit current I_{sc}, open voltage circuit V_{oc}, and fill factor FF. In the first section of this chapter we looked at the various parameters that could influence the fill factor. In the next chapter we will examine one of the ways of improving I_{sc}. In this section, we would like to understand what the V_{oc} represents for the device and the parameters that influence it.

The origin of V_{oc} has been subject to debate for a long while. One of the early works on this was done by X.Wei et al. [56]. He fabricated and illuminated a device with the following geometry: ITO/MEHPPV/Metal. By changing the electrode from aluminium to copper, he observed a decrease in V_{oc}. From this he concluded that V_{oc} should be proportional to the difference in work function between ITO and the metal. A few years later, C.M. Ramsdale et al. [57] studied the dependence of V_{oc} in a bilayer device configuration with the upper electrode work function. While there appears to be a linear dependence between V_{oc} and the difference in work function, there seems to be an extra $1V$ that the authors assumed to be the result of space charge limited current resulting from carrier accumulation at the interface. While this was fairly accepted in the bilayer device, in bulk hetero-junction, things seemed to be very different. By looking at the V_{oc} dependence on the acceptor strength, C. J. Brabec et al. [58]. found a strong correlation between them while A. Gadisa et al. [59] found a strong correlation with the donor's electron affinity. This strong correlation with the electron affinity was dependent on the presence of LiF in the device. With LiF the correlation was strong but without LiF there was no correlation. All of these findings were later on summarized by V. D. Mihailetchi et al. [60]. They concluded from their studies that in a bulk hetero-junction device, there exist two cases as far as the V_{oc} is concerned. In the first case there is ohmic contact with the blend, meaning the fermi level of the anode and that of the cathode align with the HOMO of the donor and the LUMO of the acceptor, respectively; assuming that the HOMO (LUMO) can directly inject holes unto the anode (cathode) Fermi E. The other case is when this alignment does not exist (nonohmic contacts). In the first case, it was concluded that :

$$e(V_{oc} - \Delta V_b) = HOMO_{donor} - LUMO_{accpetor} \tag{4.9}$$

where ΔV_b is the sum of the voltage loss at the contact due to band bending. In the case of nonohmic contact,

$$e(V_{oc}) = W_{Anode} - LUMO_{Cathode} \tag{4.10}$$

This has been more or less accepted in the field up to this point, as there has been no challenge.

4.3.2 V_{oc} vs. $V_{built-in}$

4.3.2.1 V_{oc} as an extrinsic parameter of the device

From our simulations in section 4.2, it is clear that V_{oc} depends on almost all parameters.

Figure 4.9(b) shows a dependence on the sample thickness. This can be understood from the fact that by increasing the device thickness beyond the drift length of the carriers, the drift current is reduced. The total current in a device is the sum of both the diffusion current and the drift current. At V_{oc}, these two are opposite and equal in magnitude; that is why the total current is zero. By increasing the device thickness we also reduce the drift current; since the current is proportional to the voltage it is only normal that V_{oc} should decrease with increasing thickness.

In Figure 4.10(b) we observe an increase in V_{oc} with increase in $\mu \times \tau$. This too is expected as an increase in $\mu \times \tau$ will lead to an increase in drift current (see Chapter 2), which will mean an increase in the voltage at which the drift current is the same as the diffusion current.

The same reason could be used to explain the increase in V_{oc} with illumination in Figure 4.11(b). Lin et al. [61]. have shown that V_{oc} can be modified by the type of solvent used for the blend. Hence the device morphology controls V_{oc} as well.

All these are indications that V_{oc} is an extrinsic parameter of the device. It varies from device to device depending on the device thickness, morphology and the number of defects in the device. So while it might be a good parameter from the engineering point of view, it says very little about the fundamental physics of the device.

4.3.2.2 $V_{built-in}$ as an intrinsic parameter of the device

From all the figures (Figure 4.9 to 4.11), there is a maximum value for V_{oc} and that value is $V_{built-in}$. This means that after having performed all possible optimizations, we still will not be able to go beyond the value of $V_{built-in}$. From equation 4.8, $V_{built-in}$ can be identified as the point at which the I-V characteristics at various illumination intensities meet.

Figure 4.17(a) and 4.17(b) show the I-V characteristics of a device made with the P3HT:PCBM (1.2:1) and MDMOPPV:PCBM (1:4), respectively. These devices show $V_{built-in}$ of $0.73V$ and $0.77V$, respectively.

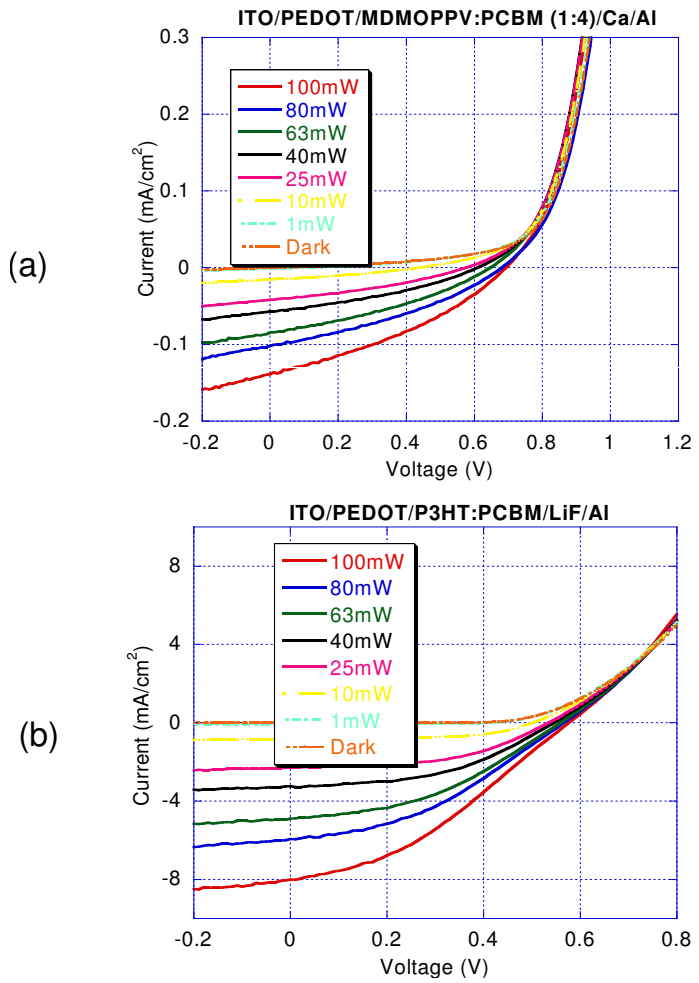

Figure 4.17. Illumination dependence of MDMOPPV:PCBM (a) and P3HT:PCBM (b) I-V characteristics.

4.3.3 Origin of $V_{built-in}$

Because a higher $V_{built-in}$ means a higher upper limit for V_{oc}, it is important to determine the origin of $V_{built-in}$ or at least the parameters that determine it. In this section, we will study the effect on $V_{built-in}$ of the electrodes' work function in an ohmic configuration, as well as in a nonohmic configuration. In an ohmic configuration, we will also look at the effect of the HOMO of the donor and LUMO of the acceptor on $V_{built-in}$. This is to determine whether what was observed as the origin of V_{oc} applies to $V_{built-in}$ as well.

4.3.3.1 Electrode work function effect on $V_{built-in}$ in nonohmic contact

We fabricated devices with the following configuration:

ITO/PEDOT/P3HT:PCBM(1.2:1)/Ag and ITO/PEDOT/P3HT:PCBM(1.2:1)/Al.

From the Energy diagram in Figure 4.18, the work function of silver and that of aluminium is $4.3eV$ and $3.9eV$, respectively. There is an energy difference with respect to the LUMO of PCBM of $.6eV$and $.2eV$. From this it can be deduced that there is no ohmic contact between either of these metals and the PCBM.

Figure 4.19(a) and (b) present the I-V characteristics obtained from these two devices. The built-in voltage obtained for the device with silver is $0.5V$ and for the device with aluminium it is $0.7V$. The difference in work function between ITO and silver is $0.5eV$; the same difference with aluminium is $1.2eV$. We can thus conclude that there is a correlation between the built-in voltage and the electrodes' work function difference when there is no ohmic contact. In the case of silver this difference is exactly the value of the built-in voltage. There is a difference of about $0.5V$ for aluminium.

4.3.3.2 Electrode work function effect on $V_{built-in}$ in ohmic contact

We made and characterized devices with LiF as shown in Figure 4.20. These have been commonly used to create an ohmic contact between the electrode and PCBM. The reason for this is that there is a dipole-dipole interaction between LiF and PCBM which pins the electrode Fermi level to the LUMO of PCBM thereby creating an ohmic contact. To see its effect on the built-in voltage, we made devices with various electrodes (magnesium, silver, aluminium, and gold). V. D. Mihailetchi et al. [60] concluded from their study of V_{oc} in an ohmic contact case that it does not depend on the difference in work function of the electrodes but rather on the difference between the HOMO of the donor and the LUMO of the acceptor. Even though in our study the contact is ohmic, we see a clear correlation with the work function difference. This is in contradiction with the result obtained when

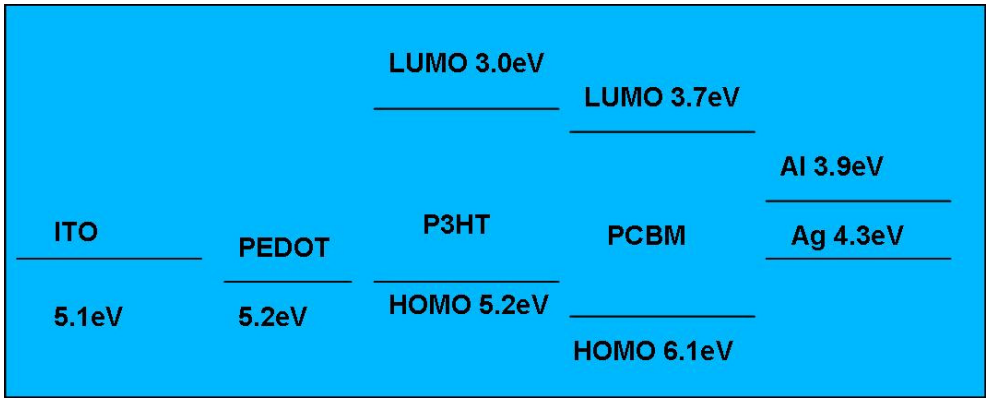

Figure 4.18. Energy diagram of ITO/PEDOT/P3HT:PCBM/Al or Ag.

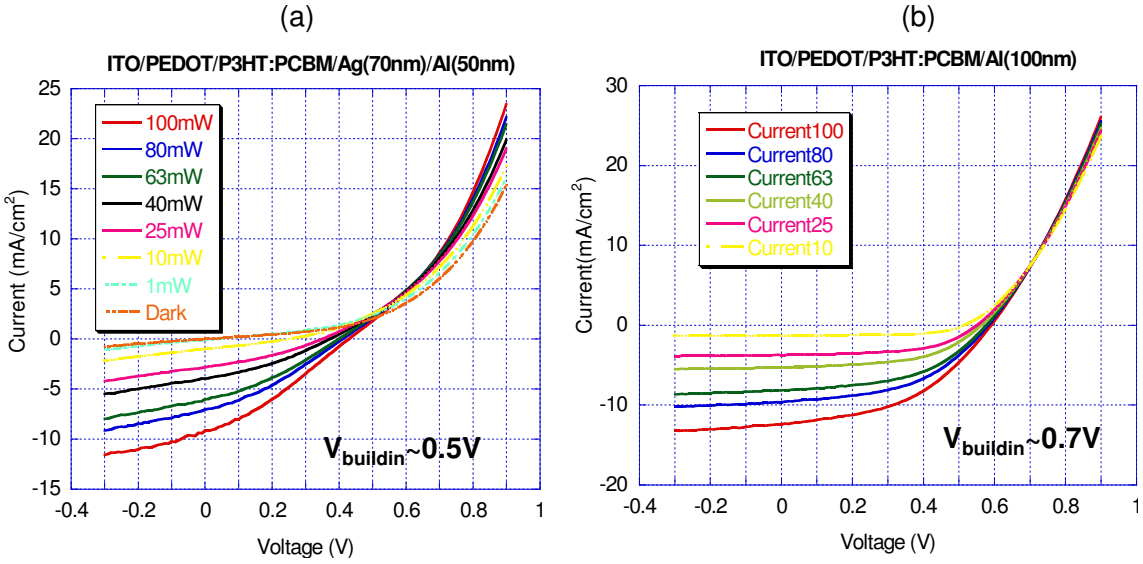

Figure 4.19. I-V characteristics of ITO/PEDOT/P3HT:PCBM/X; (a) X = Ag (b) X = Al.

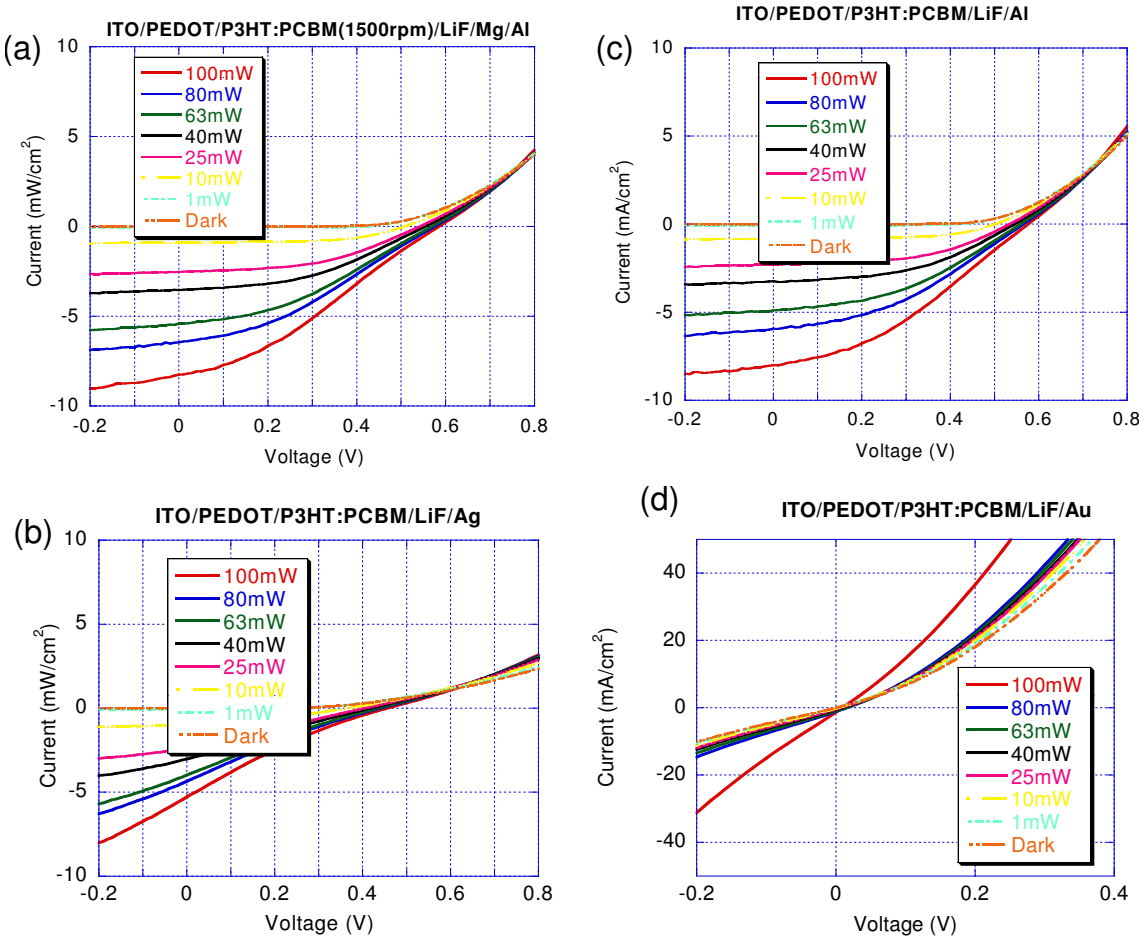

Figure 4.20. I-V characteristics of ITO/PEDOT/P3HT:PCBM/LiF/X;(a) X = Mg (b) X = Ag (c) X = Al (d) X = Au.

looking at V_{oc}. The results from our study are presented in Table 4.1 which summarizes the various built-in voltages obtained and compares them with the difference in work function of the electrodes. Just as in the case of nonohmic contact, the difference in work function is not exactly the same as the built-in potential.

4.3.3.3 Donor HOMO and acceptor LUMO effect on $V_{built-in}$

In ohmic contact configuration, we fabricated devices with different blend constituents. We made devices with P3HT:PCBM (1.2:1); Poly(3-dodecylthiophene-2,5 diyl)(P3DT):PCBM (1.2:1) and lastly MDMOPPV:PCBM (1:4). P3DT is a modified version of P3HT; in this compound the $(CH_2)_5CH_3$ of P3HT is replaced with $(CH_2)_{11}CH_3$. Even though the structure of P3HT is very different from that of MDMOPPV, these two have almost the same HOMO level $\sim 5.1eV$. We assumed that P3DT had the same HOMO level as well; we were unable to find its energy diagram in the literature. The difference observed in built-in voltage is indicative of the fact that the influence of $HOMO_{donor} - LUMO_{acceptor}$ might be smaller compared to the influence of the electrode work function difference. There is an intimate relation between the analysis done for determining V_{oc} in bulk heterojunction solar cells and the one used in a silicon photodiode. When there is ohmic contact, the anode is assumed to be pinned to the HOMO of the donor while the cathode is pinned to the LUMO of the acceptor. Thus the internal voltage is equal to the difference $HOMO_{donor} - LUMO_{acceptor}$. This is very similar to the situation in PN-junction. The HOMO of the donor can be regarded as one of the quasi Fermi level and the LUMO of the donor as the other one. So just like in a silicon photodiode, V_{oc} at $0K$ is just the band gap energy. In our case it will be

$$e(V_{oc}) = HOMO_{donor} - LUMO_{acceptor} - e\Delta b \tag{4.11}$$

where Δb is related to the carrier accumulation at the organic/metal interface. At temperature different from $0K$, V_{oc} is given by:

$$e(V_{oc}) = E_g - KTlog(1 + \frac{I_0}{I_{sc}}) \tag{4.12}$$

where E_g is the band gap energy. Figure 4.21 summarizes the results obtained from this experiment. This equation shows that V_{oc} decreases with temperature. The question therefore is can this model be applied to the built-in voltage? To provide an answer to this question we compared the dependence of the built-in voltage with temperature to that of V_{oc}. The result of this experiment is presented in Figure 4.22.

Table 4.1. Build in voltage as a function of work function difference

LiF/Metal	V_{bi}	$W_{ITO} - W_{Metal}$
Mg	$0.75V$	$1.52eV$
Al	$0.72V$	$1.2eV$
Ag	$0.6V$	$0.8eV$
Au	$0V$	$0eV$

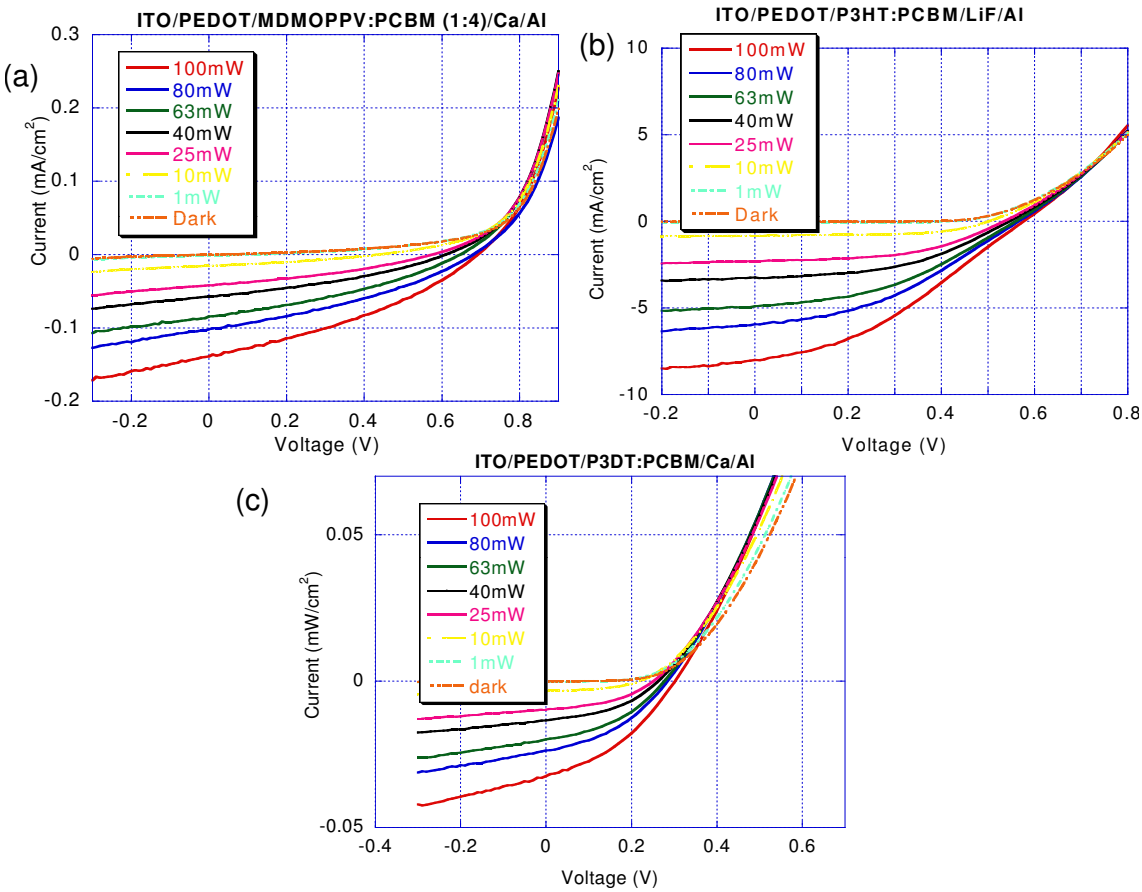

Figure 4.21. I-V characteristics of MDMOPPV:PCBM (a), P3HT:PCBM (b) and P3DT:PCBM (c)

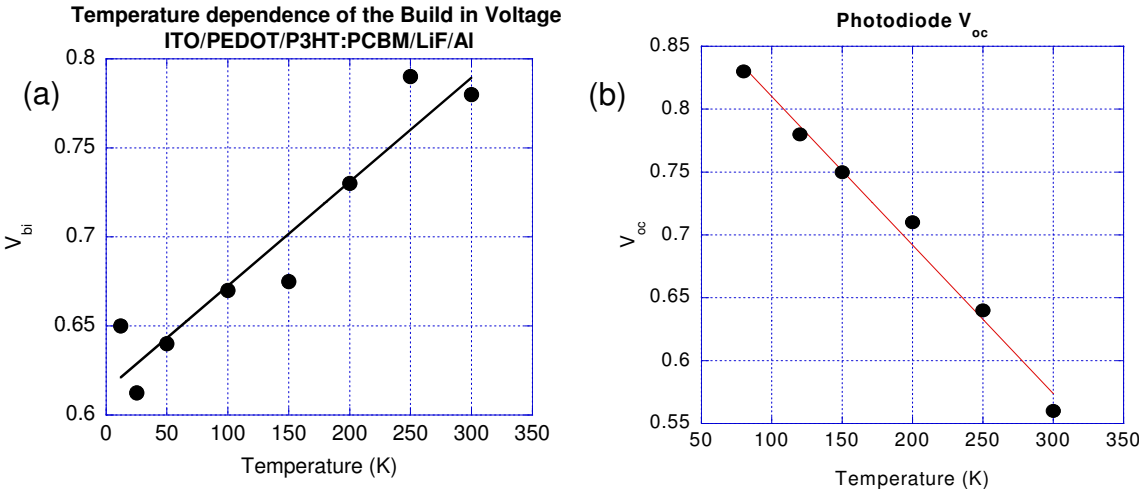

Figure 4.22. Built-in voltage of a P3HT:PCBM device (a) and open circuit voltage of a silicon photodiode (b) as a function of temperature.

Clearly the behavior is completely opposite; thus this model cannot be applied to determining $V_{built-in}$.

4.4 Discussion and conclusion

We have shown that V_{oc} is an extrinsic parameter of the device. It depends on many parameters such as the illumination intensity, device thickness, and morphology. V_{oc} from our simulation has an upper limit, which is the built-in voltage in the device. From this we can safely say that $V_{built-in}$ is the ultimate parameter to look into when trying to improve the device performance.

In nonohmic configuration, $V_{built-in}$ shows a correlation with the work similar to what was observed by V. D. Mihailetchi et al. [60] in their summary paper on the origin of V_{oc}. However, in nonohmic where they observed no dependence on the metal work function, we found that there is correlation between $V_{built-in}$ and the work functions of the electrodes.

In ohmic contact configuration, the behavior of $V_{built-in}$ with temperature is completely opposite to that of a silicon diode. This cast doubts on the use of a Metal-semiconductor-metal-type model in this case. Considering however that the HOMO and LUMO energy levels of organic semiconductors are not discrete but are best represented by temperature dependent gaussian distributions, a temperature dependent $V_{built-in}$ is easily deduced. It was also found in this configuration that even with the same difference in electrode work function and the same difference $HOMO_{donor} - LUMO_{acceptor}$, there is still a difference in $V_{built-in}$. This implies that the carrier accumulation at the interface between the organic and the metal is blend specific with every blend leading to a particular carrier accumulation amount.

CHAPTER 5

SPIN 1/2 RADICAL EFFECT ON BULK HETERO-JUNCTION ORGANIC PHOTOVOLTAICS

OPVs have been the subject of intensive investigation because of the prospects in cost effectiveness and environmental benignity. However, this investigation is slow in yielding practical returns due to the low power conversion efficiency ($\sim 6\%$) and the low stability of these devices. One of the main contributing factors to the low efficiency is the low output current due to the high carrier's recombination rate and low carrier mobility.

In BH-OPV, the accepted mechanism for current production is the following: First, upon illumination, there is exciton generation in the blend, followed by a migration of the exciton to the donor-acceptor interface where either because of the existence of a build in potential or the dipole interaction between the donor and the acceptor, this exciton is separated into a free electron in the acceptor and hole in the donor. From this point, the electron and hole migrate to the cathode and the anode, respectively. For efficient device performance, one must have an exciton diffusion length that is larger than the average donor or acceptor aggregate size to minimize exciton recombination. For efficient exciton separation the exciton binding energy must also be smaller than the dipole-dipole interaction between the donor and the acceptor or the build in voltage. There must be high and equal electron and hole mobility for better carrier collection, and lastly, for the same purpose, an ohmic contact between the organic constituents and the electrodes should be formed.

Yang et al. [62] recently showed that adding spin 1/2 radical molecules to a solution of MEHPPV leads to an improvement of the triplet exciton lifetime by about 20%. Based on these results and some other preliminary results, we decided to perform an in depth study of the effect of these radical molecules on BHOPVs.

5.1 Spin 1/2 radical effect on various polymer blends

5.1.1 Experimental

We used two different polymer blends to which we added: a free radical organic compound at various weight ratios with respect to the donor: 2,2,6,6-Tetramethylpiperidine 1-oxyl (TEMPO). We started the study with different concentrations of TEMPO in MEHPPV:PCBM (1:2) blends. Dr. Xiamey [63] had already observed that the radical effect on an MEHPPV:PCBM blend is best observed when the concentration of these two constituents is 1:2. We also studied the effect of these radicals in blends of P3HT:PCBM (1:1). To better comprehend the origin of the effect, we performed I-V characterization, frequency dependent polaron PA measurements, quantum efficiency picosecond Photo-bleaching and impedance spectroscopy measurements.

5.1.2 Spin 1/2 radical effect on MEHPPV:PCBM blends

The addition of 10% and 20% radicals in MEHPPV:PCBM (1:2) blends leads to an increase in efficiency for the larger concentration and an unchanged efficiency for the smaller one (Figure 5.1). We also observed that the fill factor is unchanged upon addition of radicals. Reducing the radical concentration to 2% and 5%, we observed an increase in efficiency for 2% radical with a reduction for 5%. The fill factor also remains unchanged. While the increase in current and the constant value of the fill factor were repeatable for different batches, the observed decrease in V_{oc} was not. We believe that the amount of radical added to the system is too small to change the potential profile of the devices. Thus, the increase in efficiency is solely due to the increase in current.

5.1.3 Spin 1/2 radical effect on P3HT:PCBM blends

Figure 5.2 shows the IV characteristics of a blend of P3HT:PCBM with various concentrations of radicals. The insert also represents the obtained efficiencies, fill factors and current densities. In P3HT:PCBM devices, everything seems to behave the same as in devices with MEHPPV:PCBM. However, the fill factor seems to increase at 2% before dropping drastically at 5%. The sharp increase in current is responsible for the sharp increase in efficiency. On average, for devices from the same fabrication batch we see a 20% increase efficiency for a 2% concentration and a decrease of almost the same amount 14% for 5% concentration.

With this blend, it was rather difficult to observe any trend in the fill factor as a function of the concentration as shown in Figure 5.2. The variation on the V_{oc} and the fill factor

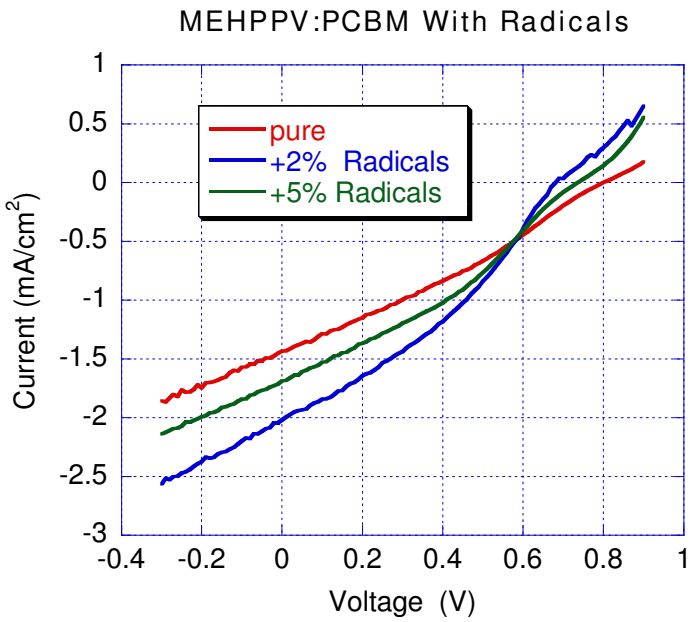

Figure 5.1. IV- curves device: ITO/PEDOT/MEHPPV:PCBM+TEMPO(1:2 + x%)/Al with $x = 0\%$, $x = 10\%$ and $x = 20\%$ at AM 1.5 elimination.

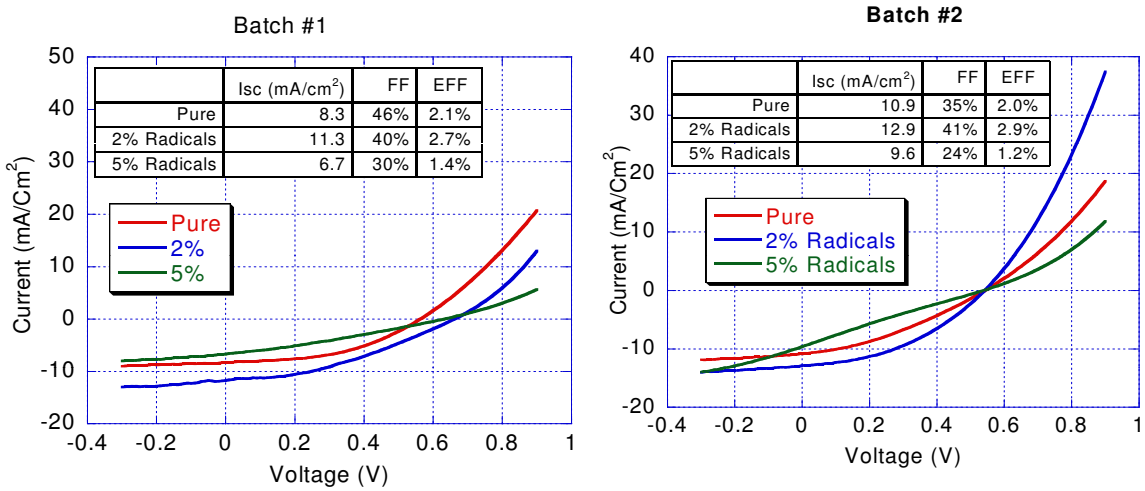

Figure 5.2. IV-curves device: ITO/PEDOT/P3HT:PCBM+TEMPO(1:1 + x%)/Al with $x = 0\%$, $x = 2\%$ and $x = 5\%$ (a) Batch 1 (b) Batch 2 under AM 1.5 illumination.

are not consistent from device to device. We therefore assume that these values remain constant with radical concentration.

5.1.4 Discussion

For both blends, we observe an increase in efficiency with increasing concentration of radicals. This increase is mainly due to the increase in current. Even though in some cases this increase in efficiency is accompanied by some increase in fill factor, we choose to disregard this effect, since it is not consistent from device to device. The open voltage circuit does not show any substantial change that we can attribute to the increase of radical concentration. As stated above, the concentrations of radicals used in this study are so low that it is unlikely that they can change the internal electric field profile of the device.

While devices fabricated with MEHPPV:PCBM seemed more or less stable from one batch to another in terms of their efficiencies and fill factors, the devices with P3HT:PCBM showed a lot of fluctuations both in terms of open voltage circuit and fill factor. This is mainly due to the fact that devices based on P3HT have a very regular film, and defects can disrupt the regio-regularity, leading to all kinds of fluctuating V_{oc}'s and fill factor.

The question at hand is: where does this increase in current upon increasing radical concentration come from?

5.2 Origin of the short circuit current increase

The photogenerated current density in an organic material film is given by:

$$J = \eta \times G \times \tau_r \times \mu \times E, \tag{5.1}$$

where η is the quantum efficiency for polaron photogeneration, G is the optical generation rate i.e. photon flux, τ_r is the polaron recombination time, μ is the polaron mobility and E is the internal electric field.

As stated in the previous section, the low concentrations of radicals used here have no influence on the internal electric field in the device; thus E is constant. In the following subsections, we are going to examine the effect of radicals on η, τ_r and μ.

5.2.1 Radical effects on the photocurrent action spectrum

The photocurrent action spectrum measures the efficiency of photocurrent generation with respect to the photon wavelength. The addition of radicals in the system could extend the action spectrum in regions where P3HT and PCBM by themselves show no photocurrent. Any such changes can lead to an increase in current.

IPCE measurements performed on MEHPPV:PCBM devices with different concentrations of radicals (Figure 5.3) show only an increase in the magnitude of the photogenerated current. There is no new band created in the spectrum. This implies that there is no change in the absorption of the film on addition of radicals, and thus no states are created in the gap.

5.2.2 Radical effects on the quantum efficiency polaron generation

Linear photon absorption in conjugated polymers generates self-trapped photoexcitations due to the strong electron-phonon coupling. These excitations originate new electronic states within the gap, giving rise to photoinduced transitions with redistribution of the oscillator strength. This results in an inherently strong and fast ($\sim 10^{-13}s$) nonlinear optical response. Photoexcitations can be studied in the visible, near-infrared and infrared spectral regions by measuring the photoinduced absorption (PA), either by continuous wave (CW) photomodulation or by pump-probe techniques. As seen in Chapter 2 the quantity of interest in these measurements is given by:

$$-\frac{\Delta T}{T} = \frac{T - T_{ex}}{T} \tag{5.2}$$

where T and T_{ex} are, respectively, the transmission of the sample in the ground state and in the excited state. Considering Figure 5.4, let level 2 be an electronic state that is formed upon photoexcitation of the transition from the ground state (level 1) to level 3, with a characteristic time τ. By monitoring the transmittance of such a system following photoexcitation, one would observe the emergence of a new absorption feature ($2 \Rightarrow 3$), the so called photoinduced absorption (PA), within the characteristic time τ. Moreover, due to the population depletion of the ground state, the transition ($1 \Rightarrow 3$) will lose some strength, a phenomenon that is known as photobleaching (PB). As a consequence, the negative differential transmittance spectrum will show a negative peak at the energy corresponding to the ($1 \Rightarrow 3$) transition (PB) and a positive peak at the energy corresponding to the photoinduced ($2 \Rightarrow 3$) transition (PA). Time-resolved photoinduced absorption measurements provide information on the dynamics of the nonlinear photoexcitations, which is fundamental for understanding the basic events occurring in the excited state. By time-resolving the photobleaching, we can obtain the quantum efficiency of polaron generation.

Such measurements were performed on MEHPPV films with different concentrations of radicals by a colleague (Sanjeev Singh). The time range for this measurement is limited to 100 picoseconds; which is inadequate for monitoring any polaron generated from triplet

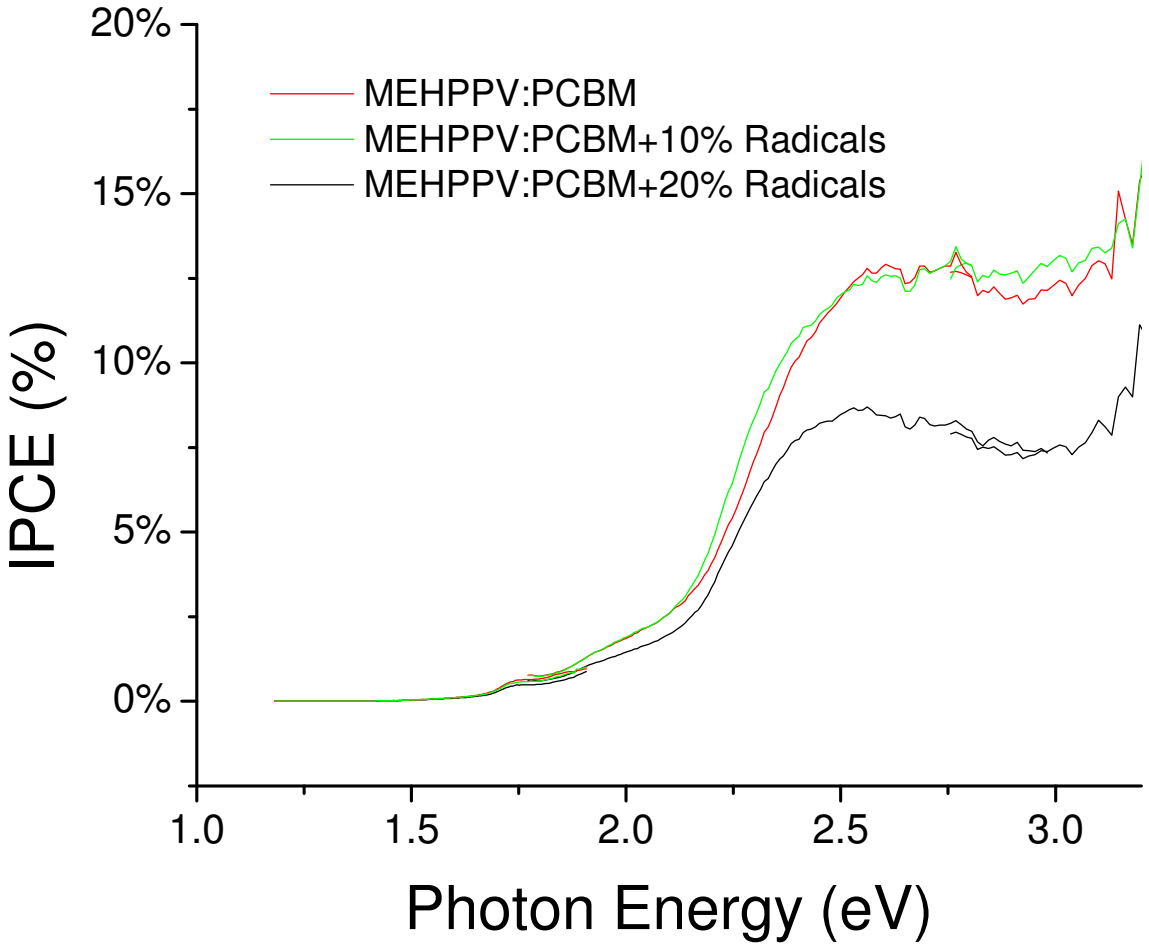

Figure 5.3. Action spectrum of: ITO/PEDOT/MEHPPV:PCBM+TEMPO(1:2 + x%)/Al with $x = 0\%$, $x = 10\%$ and $x = 20\%$.

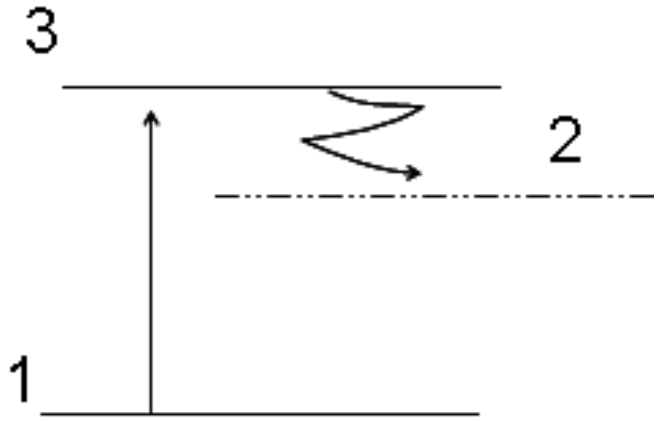

Figure 5.4. Energy diagram of photoexcited film.

exciton separation that occurs at a later time. It was observed (see Figure 5.5) that up to 100 ps, the polaron generation rate remains unchanged upon addition of radicals to the film, i.e., η is constant. We know from Dr. Yang [62] that in the microsecond range, triplet excitons resulting from the intersystem crossing of singlet excitons live longer. Thus the dynamics of the resulting polarons are not accounted for in this ultra fast measurement.

5.2.3 Radical effects on the polaron recombination time

As discussed in Chapter 2, by monitoring the frequency dependence of the PA by CW photomodulation, it is possible to obtain the polaron recombination time. Any change in this time upon addition of radicals should be observable from this measurement. The results of the use of this technique are summarized in Figure 5.6. Up to 100kHz, we observed no change in recombination time upon adding radicals.

The recombination time monitored is the sum of recombination times of bound and free polarons. It is unlikely that the dynamics of these two are the same. Because we are interested in the lifetime of free polarons, there is a possibility that we could have a change in recombination time, but given the high density of bound polaron compared to that of free polarons, we are observing the average value of this time - so this time does not change upon adding radicals.

5.2.4 Radical effects on the film morphology

The reason for an increase in current might not be limited to an increase in mobility. There could also be a change in the film morphology or a combination of the two effects. We studied the effect on morphology by AFM contact mode. Kim et al. [64] have demonstrated that the higher features observed in the AFM picture represent the aggregation of PCBM in the film. They showed that by annealing the P3HT:PCBM blend, phase separation between P3HT and PCBM occurs with the aggregates' size increasing. In addition they observed that the PCBM molecules protrude above the film surface; this is one of the main effects of thermal annealing. As PCBM protrudes, there is an increase in interface area with P3HT which means increase in charge separation efficiency. The undesirable effect in this case is the increase in aggregates' size; the higher the aggregates, the more we move away from the hetero-junction structure to a bilayer structure. Figure 5.7(a),(b) and (c) show the morphology of a pure P3HT:PCBM, P3HT:PCBM +2% radicals and P3HT:PCBM +5%. The same features observed by Kim et al. [64] are observed in these films. We observe an increase in both peaks' heights and aggregates' size with increasing concentration as we go from pure to 5%. The increase in aggregate size as said above is detrimental for the device,

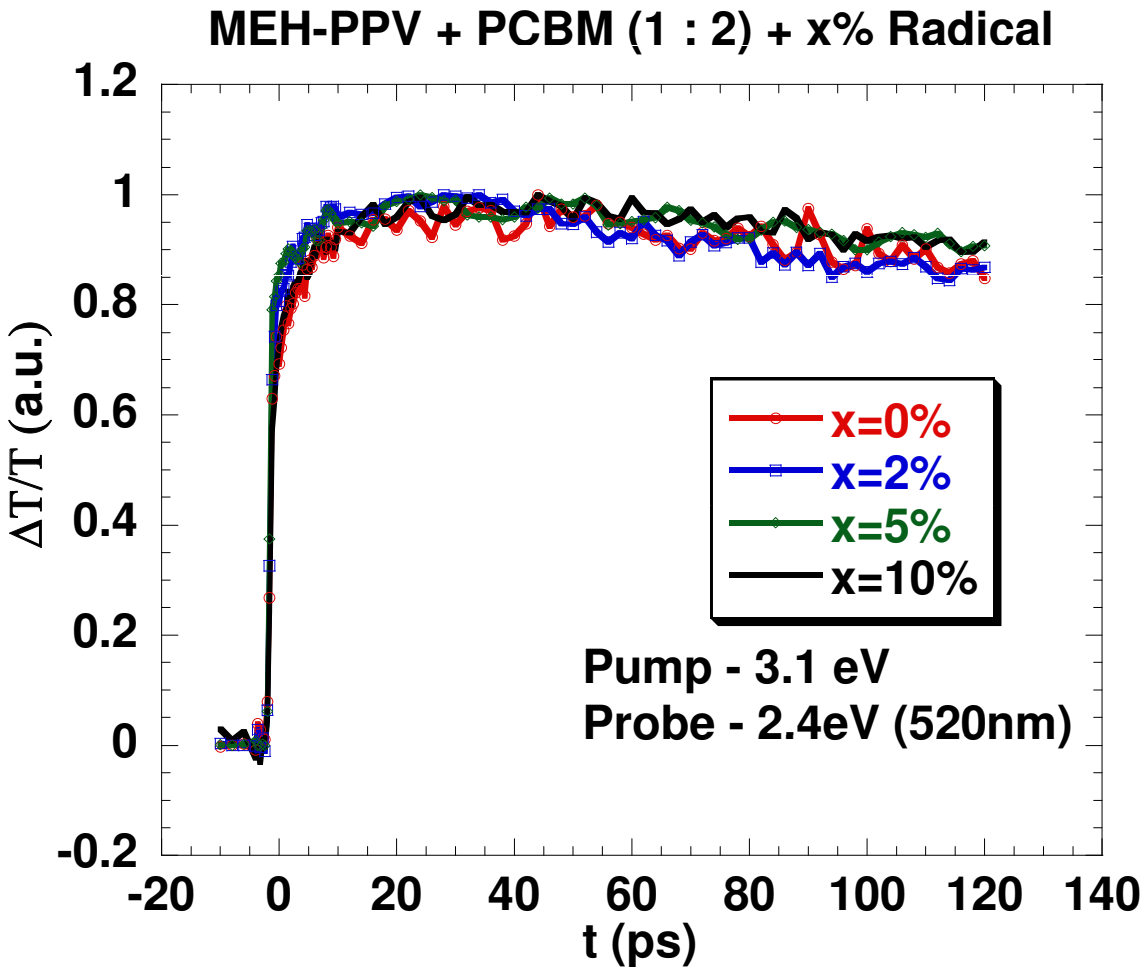

Figure 5.5. Photobleaching of MEHPPV + x% radicals.

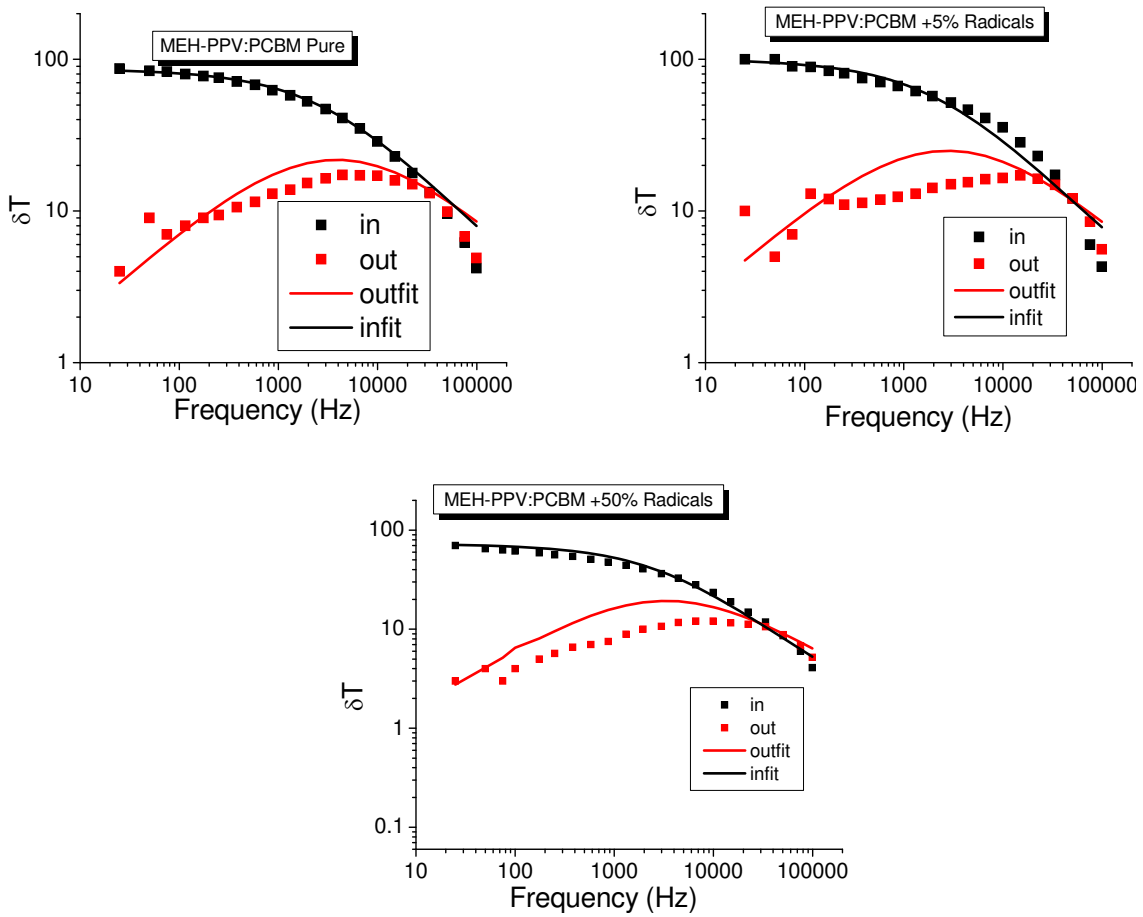

Figure 5.6. PA frequency dependence (both in phase and quadrature) of MEHPPV + x% radicals at room temperature.

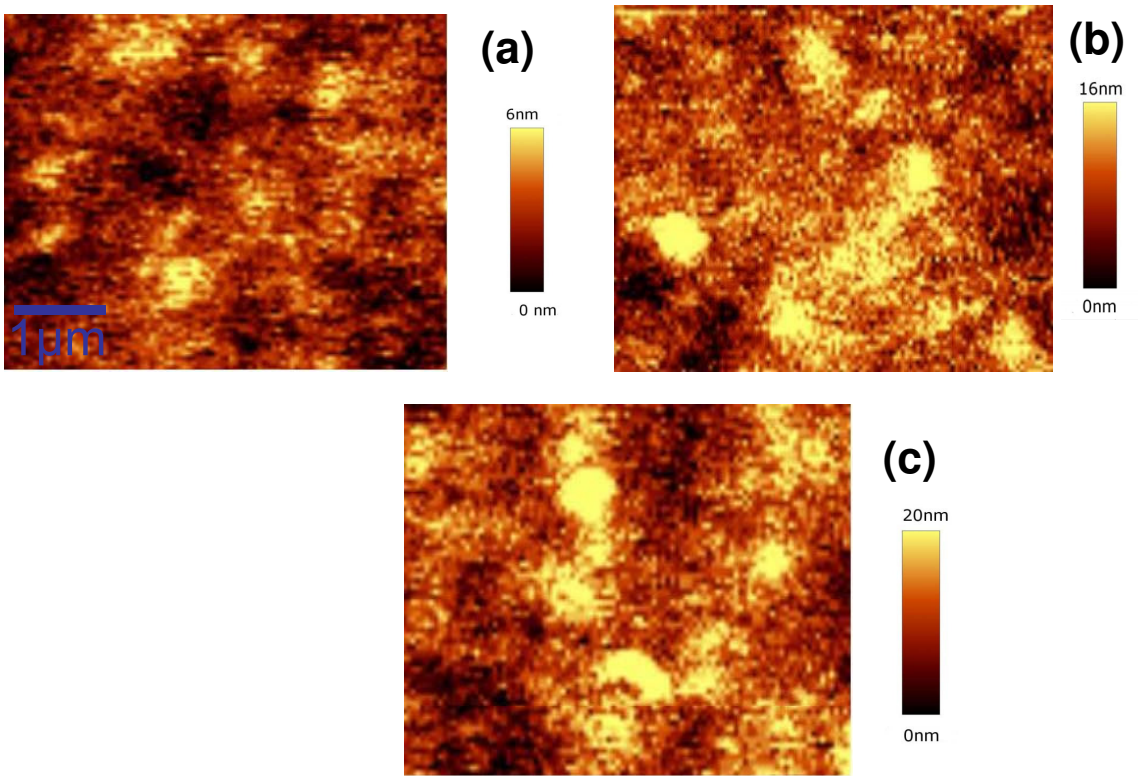

Figure 5.7. AFM images of P3HT + x% Radicals (a) Pure (b) 2% Radicals (c) 5% Radicals.

which could explain why the 5% devices have such low power conversion efficiencies. The increase in peak height is not enough to account for the increase in efficiency from pure to 2%. We can thus conclude that the increase in efficiency cannot account for the increase in current.

5.2.5 Radical effects on the carriers' mobility

Carrier mobility has been measured using the impedance spectroscopy technique described in Chapter 2. Data analysis was performed based on the assumption that we are in the framework of trap limited space, charge limited current. In order to extract the mobility of one carrier only, we fabricated hole-only devices (ITO/polymer/Au). This was done to avoid bipolar injection which might make it difficult to extract the mobility from the data. The devices were fabricated and sealed to prevent degradation from air exposure. In order to preserve the geometric capacitance during the measurements, we applied dc fields below 7V. At higher fields, there is carrier injection into the device, which could lead to trap filling and thus change the geometric capacitance.

5.2.5.1 Radical effects on the hole mobility in MEH-PPV hole-only devices

In our circuit for impedance spectroscopy measurements, the device acts as a low pass filter. Any frequency dependent process through the device is only observable for frequencies lower than the cut-off frequency. This means that the transit time in our device must be longer than the circuit's time constant: $\tau_{dc} >> RC$. It is therefore important to choose the appropriate device thickness and area in order to minimize R and C, respectively.

For our devices with MEHPPV, the optimum values for the thickness and the device area were, respectively, $0.5\mu m$ and $3mm \times 3mm$. The thickness was measured using a profilometer.

Figure 5.8 shows the impedance spectrum of pure MEHPPV hole-only devices as a function of applied DC voltage. We fitted these curves as described in Chapter 2. As can be seen from the fit quality, the trap limited space charge limited assumption is appropriate. Table 5.1 through 5.3 represent the fitting parameters obtained.

The film thickness was calculated using the obtained values of the geometric capacitance. This voltage does not depend on the applied voltage biasing. Using its average value, we obtained a film thickness of about $405 \pm 50nm$ which is in fair agreement with the measured value of $487nm$. The values of M and γ obtained are typical for a dispersive material such as MEHPPV. We note that at low voltages the values of M are larger, and these values

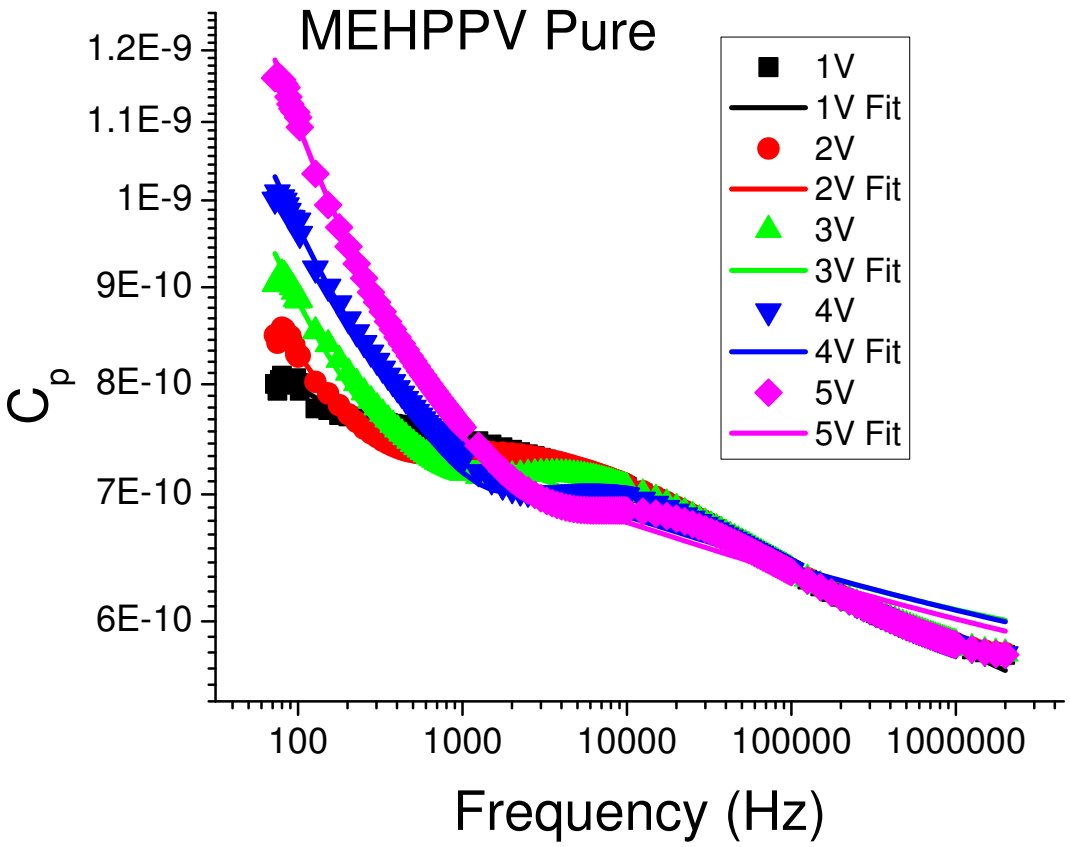

Figure 5.8. Impedance spectrum of pure MEHPPV fitted with the trap limited space charge limited current model developed in Chapter 2.

Table 5.1. Fit parameters for the impedance spectrum of pure MEHPPV

	1V	2V	3V	4V	5V	7V
Cp	3.10×10^{-10}	4.7×10^{-10}	5.37×10^{-10}	5.59×10^{-10}	5.54×10^{-10}	6.30×10^{-10}
μ_{dc}	5.42×10^{-03}	2.21×10^{-03}	2.00×10^{-03}	1.54×10^{-03}	2.31×10^{-04}	2.14×10^{-04}
M	0.59	0.29	0.23	0.22	0.17	0.16
γ	0.06	0.11	0.18	0.24	0.25	0.63
mobility	1.08×10^{-07}	1.33×10^{-07}	9.87×10^{-08}	9.54×10^{-08}	4.62×10^{-07}	3.56×10^{-07}

Table 5.2. Fit parameters for the impedance spectrum of MEHPPV + 2% radicals

	1V	2V	3V	4V	5V	6V	7V
Cp	1.01×10^{-9}	1.15×10^{-9}	1.40×10^{-9}	1.06×10^{-9}	5.74×10^{-10}	4.06×10^{-10}	2.72×10^{10}
μ_{dc}	4.40×10^{-04}	1.79×10^{-04}	1×10^{-04}	5.98×10^{-05}	3.98×10^{-05}	2.98×10^{-05}	1.50×10^{-05}
M	0.85	0.85	1.09	1.09	1.09	1.09	1
γ	0.96	0.95	0.97	0.96	0.96	0.96	0.96
μ	1.21×10^{-06}	1.49×10^{-06}	1.78×10^{-06}	2.23×10^{-06}	2.68×10^{-06}	3.58×10^{-06}	5.08×10^{-06}

Table 5.3. Fit parameters for the impedance spectrum of MEHPPV + 5% radicals

	1V	2V	3V	4V	5V	6V	7V
Cp	1.18×10^{-9}	1.16×10^{-9}	1.20×10^{-9}	1.14×10^{-9}	9.67×10^{-10}	9.71×10^{-10}	9.39×10^{10}
μ_{dc}	4.00×10^{-2}	3.00×10^{-2}	2.44×10^{-4}	1.31×10^{-4}	9.17×10^{-5}	7.10×10^{-5}	5.06×10^{-5}
M	3.01	4.73	0.33	0.34	0.42	0.42	0.43
γ	0.58	0.62	0.69	0.75	0.74	0.76	0.75
μ	1.42×10^{-08}	8.22×10^{-09}	7.29×10^{-07}	1.02×10^{-06}	1.16×10^{-06}	1.25×10^{-06}	1.50×10^{-06}

get lower at high voltages. This is evidence of traps being filled in the material. At low voltages, the trap density is high, thus there is high dispersity in the system. As expected, the transit time τ_{dc} is lowered by increasing the bias voltage.

The same analysis was performed for devices with 2% and 5% radicals added to MEH-PPV. Care was taken to insure that the film thickness remained the same as radical solution was added to the MEHPPV solution, since the final concentration of MEHPPV is also changed. This can lead to discrepancies in the devices' thicknesses. To make sure this does not occur, we added into all solutions (Pure and 2%) as much solvent as there was in the solution with 5% radicals.

The field dependence of the mobility for different radicals' concentrations is given in Figure 5.9.

The mobility for disordered materials is best described by the Poole-Frenkel model as:

$$\mu = \mu_0 exp(-\frac{\Delta}{KT} + \beta\sqrt{E}) \tag{5.3}$$

Where μ_0 is the zero field mobility, Δ is the zero field mobility thermal activation energy, β is the electric field coefficient.

Fitting Figure 5.9 with the above equation, we can obtain Δ and β for each radical concentration. Table 5.4 shows these parameters.

The values obtained for Δ agree with the reported value for MEHPPV in the literature[65]. As expected the zero field mobility thermal activation energy increases with radical concentration from pure to 2%. But just like the mobility or the current, this activation energy decreases as we reach 5% radical concentration. At 2% radical, the field coefficient is very small. This is indicative of the low field dependence observed at this concentration. This could be an indication of an increase in the energetic order in the system. That is the traps present in the system contribute no more to the decrease of the mobility, but rather to its increase.

5.2.5.2 Radical effects on the hole mobility in P3HT hole only devices

For P3HT devices, we found the optimum thickness to be $835\mu m$ with a device area of $3mm \times 1mm$. We performed the same measurements and analysis for devices with P3HT. This gave us a thickness of $600 \pm 20nm$, which again is close to the measured value. Figure 5.10 shows the spectra that were obtained at various biases of the pure sample with their respective fits.

The fit parameters obtained are summarized in Table 5.5 through 5.7.

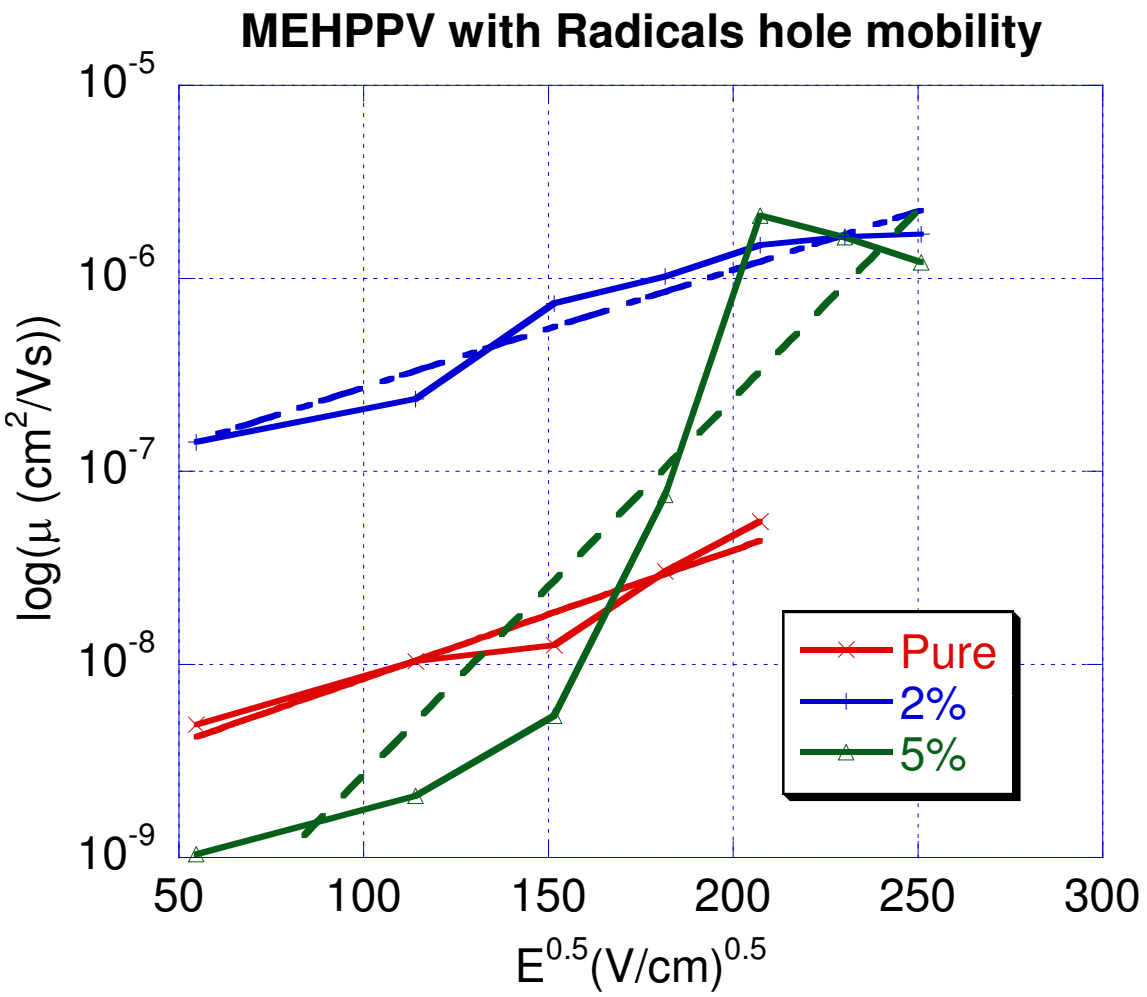

Figure 5.9. Field dependent mobility of MEHPPV as a function of radical concentration.

Table 5.4. Fit parameters for the field dependence of the mobility for MEHPPV as a function of radical concentration

	Δ	β
Pure MEHPPV	$344meV$	0.0016
MEHPPV +2% Radicals	$287meV$	0.00061
MEHPPV +5% Radicals	$410meV$	0.019

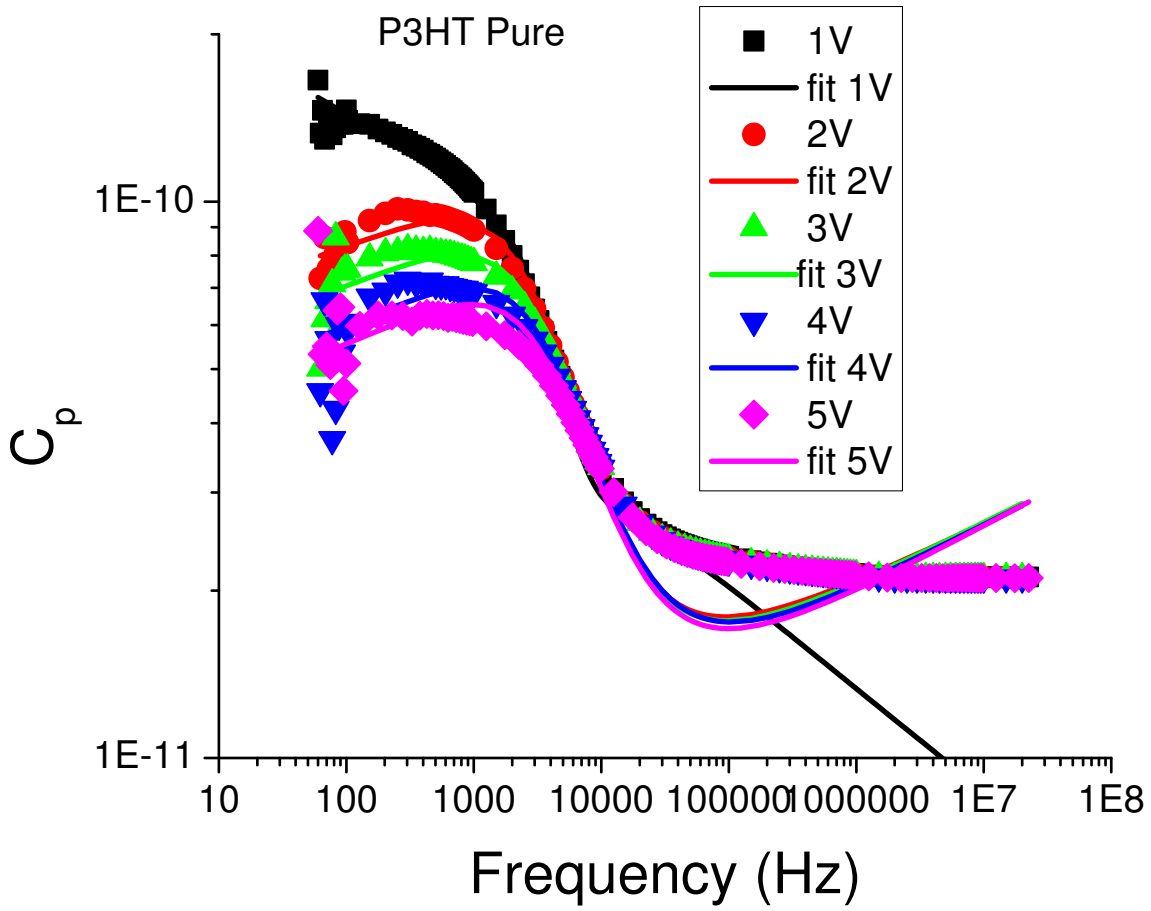

Figure 5.10. Impedance spectrum of pure P3HT fitted with the trap limited space charge limited current model developed in Chapter 2.

Table 5.5. Fit parameters for the impedance spectrum of pure P3HT

	1V	2V	3V	4V	5V
Cp	1.44×10^{-11}	1.89×10^{-11}	1.81×10^{-11}	1.76×10^{-11}	1.71×10^{-11}
τ	1.17×10^{-5}	3.32×10^{-5}	2.97×10^{-5}	2.90×10^{-5}	2.52×10^{-5}
M	0.72	0.34	0.33	0.33	0.31
γ	0.89	0.48	0.42	0.38	0.34
μ	2.85×10^{-4}	5.02×10^{-5}	3.73×10^{-5}	2.87×10^{-5}	2.64×10^{-5}

Table 5.6. Fit parameters for the impedance spectrum of P3HT + 2% radicals

	1V	2V	3V	4V	5V
Cp	1.91×10^{-11}	1.79×10^{-11}	1.11×10^{-11}	9.93×10^{-12}	9.58×10^{-12}
τ	8.69×10^{-6}	8.72×10^{-6}	1.04×10^{-5}	1.06×10^{-5}	1.13×10^{-5}
M	0.46	0.44	0.39	0.42	0.43
γ	0.91	0.96	0.58	0.49	0.44
μ	3.84×10^{-4}	1.91×10^{-4}	1.06×10^{-4}	7.84×10^{-5}	5.88×10^{-5}

Table 5.7. Fit parameters for the impedance spectrum of P3HT + 5% radicals

	1V	2V	3V	4V	5V
Cp	2.88×10^{-11}	2.91×10^{-11}	2.69×10^{-11}	2.67×10^{-11}	2.66×10^{-11}
τ	1.38×10^{-5}	1.26×10^{-5}	1.05×10^{-5}	1.02×10^{-5}	1.08×10^{-5}
M	0.28	0.27	0.29	0.28	0.28
γ	0.39	0.34	0.3	0.29	0.27
μ	2.42×10^{-4}	1.32×10^{-4}	1.06×10^{-4}	8.15×10^{-5}	6.14×10^{-5}

Upon addition of radicals in the device, the value of M goes above 1. Unlike in the MEHPPV case, these values seem constant with respect to the bias voltage. The value γ also remains unchanged during the bias application. Unlike in the case of MEHPPV, we observe a negative field dependence of the mobility with P3HT (Figure 5.11).

This was also observed by A. J. Mozer et al.[66] in their time of flight measurement of the hole mobility in P3HT. Using the Gaussian disorder model, he redefined the mobility as:

$$\mu(E,T) = \mu_\infty exp[-(\frac{2\sigma}{3kT})^2]exp[C(\frac{\sigma}{kT})^2 - \Sigma^2]\sqrt{E} \tag{5.4}$$

where μ_∞ is the high temperature limit of the mobility, σ and Σ, respectively, represent the energetic and the positional disorder of the material in use and C is just a fitting parameter with value $2 \times 10^{-4}(cm/V)^{1/2}$ for P3HT.

Mozer attributed the observation of the negative field dependence to a combination of a small energetic disorder (σ) with large positional disorder Σ). At low field and high temperature, the photogenerated carriers can reach the electrodes even though the pathways are longer as they have enough energy to hop from site to site until they find the path that leads to the electrode. At high field, there is realignment of these paths in the direction of the field which leads to a reduction of the number of pathways available for the carriers, hence a decrease in mobility. Fitting the observed field dependent mobility with equation, we obtained the parameters (σ) and (Σ) as a function of the radical concentration.

The obtained values of (σ) and (Σ)(Table 5.8) for the pure P3HT are in agreement with the values obtained by A. J. Mozer et al. [66] $\sigma = 70meV$ and $\Sigma = 3.4$.

The slight discrepancies originate from the fact that their devices were thicker than ours, as the level of disorder will depend on the sample thickness.

5.2.6 Mobility dependence on radical concentration

We believe that the increase in mobility in the device upon addition of radicals comes from spin interaction between free carriers, trap carriers and the radical molecules.

In its transit in the device, a free carrier could move totally unhindered, or it could encounter an empty trap or a half filled trap. Carriers that encounter an empty trap will have very little contribution to the current in the device. When the carrier encounters a half field trap, depending on their (incoming carrier and the trap carrier) spin configuration (parallel or antiparallel); there could be a positive or a negative contribution to the current.

When their spin configuration is parallel, because of the Pauli principle, the incoming carrier is reflected away; thus it cannot transit through the device. If, on the other hand

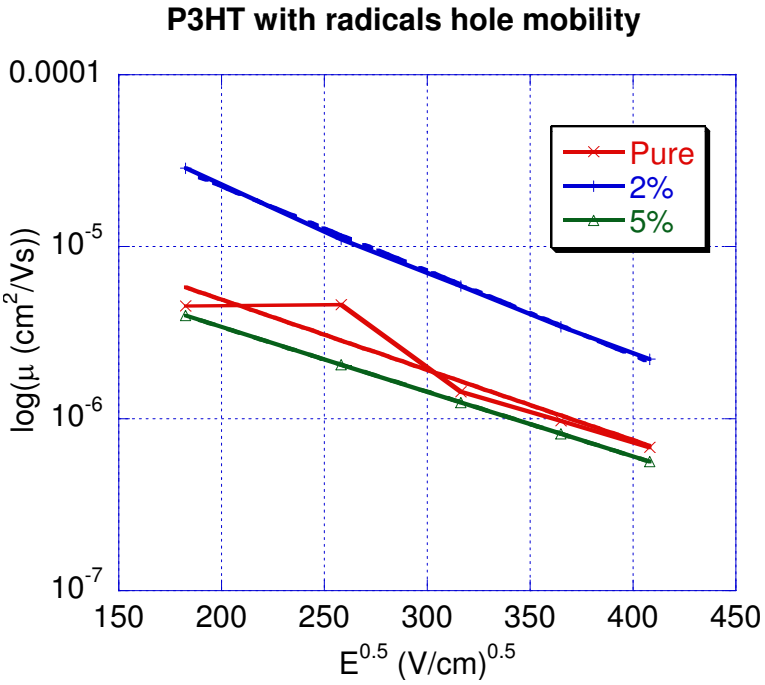

Figure 5.11. Field dependent mobility of P3HT as a function of radical concentration

Table 5.8. Fit parameters for the field dependence of the mobility for P3HT as a function of radical concentration

	σ	Σ
Pure P3HT	$44meV$	5.4
P3HT+ 2% Radicals	$39meV$	5.86
P3HT + 5% Radicals	$44meV$	5.28

their spin configuration is antiparallel, the incoming carrier can hop in and out of the trap and still transit through. Figure 5.12 summarizes these situations. Addition of spin 1/2 radicals will induce spin randomization in the system and this will lead to a change in the spin configuration of pair free carrier-half filled trap. Thus a carrier that was stuck and unable to move across the trap will be unlocked by its spin flip.

Let n_1 be the density of carriers that go unhindered (free carriers), n_2 the density of carriers that encounter an antiparallel half-filled trap and lastly let n_3 be the density of carriers that encounter a half-filled trap with parallel spin orientation.

It is worth noticing that if the carriers' transit times are much smaller than their lifetime, then n_2 and n_3 are negligible compared to n_1, and we are just in an injection limited regime. In this regime, the total current will be given by

$$J = G(V)l/E \tag{5.5}$$

where $G(V)$ is the carrier generation rate or injection rate that is voltage dependent, l is the device thickness and E is the applied field.

Since we are dealing with disordered material with small mobilities, we clearly are away from the above regime especially as the applied voltage at short circuit current is zero. It is therefore justified to write the total current density through the device as:

$$J = (n_1\mu_1 + n_2\mu_2 + n_3\mu_3) \tag{5.6}$$

where μ_1, μ_2, μ_3 are the respective mobilities of n_1, n_2 and n_3.

The rate equations of n_1, n_2 and n_3 are given by:

$$\begin{cases} \frac{dn_1}{dt} = (1-2\eta)G - \frac{n_1}{\tau_1} \\ \frac{dn_2}{dt} = \eta G - \frac{n_2}{\tau_2} - \frac{n_2 - n_3}{t_{sl}} \\ \frac{dn_3}{dt} = \eta G - \frac{n_3}{\tau_3} - \frac{n_3 - n_2}{t_{sl}} \end{cases} \tag{5.7}$$

where η is the trapping efficiency, G is the generation efficiency, τ_1, τ_2 and τ_3 are monomolecular recombination times of the free carriers, the parallel carriers and the antiparallel carriers, respectively; lastly t_{sl} is the spin lattice relaxation time in the blend. The steady state solution of equation 5.7 is given by:

$$\begin{cases} n_1 = (1-2\eta)G\tau_{t1} \\ n_2 = n_3 X \\ n_3 = G\eta Y \end{cases} \tag{5.8}$$

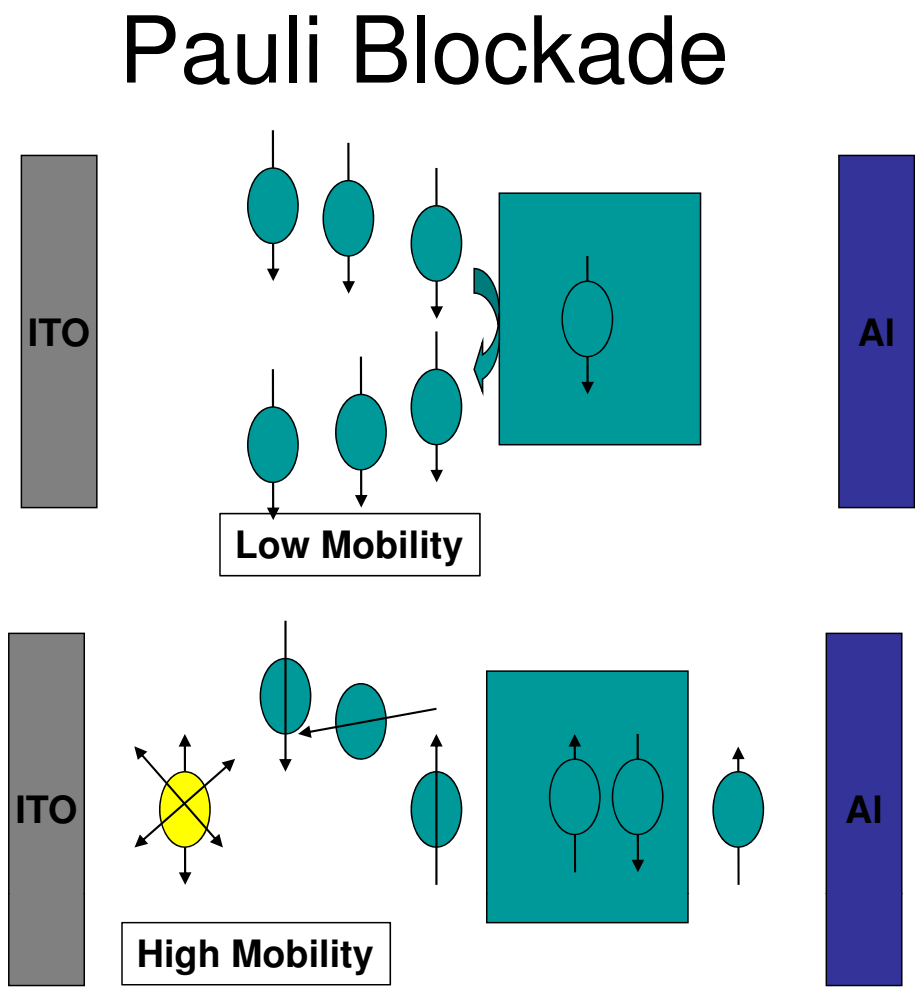

Figure 5.12. Diagram illustrating the Pauli Blockade process.

where:

$$\begin{cases} X = \frac{\frac{1}{\tau_3}+\frac{2}{t_{sl}}}{\frac{1}{\tau_2}+\frac{2}{t_{sl}}} \\ Y = \left[\left(\frac{1}{\tau_3}+\frac{1}{t_{sl}}\right) - (\frac{1}{t_{sl}})X\right]^{-1} \end{cases} \tag{5.9}$$

The total current density from the device will then be given by:

$$J = G[\tau_{t1}\mu_1(1-2\eta) + \eta\mu_2 XY + \eta\mu_3 Y] \tag{5.10}$$

- In case the spin lattice relaxation time is much longer than the transit times and the recombination times of all types of carriers; meaning the spin flip time is much longer than the characteristic times of the system, equation 5.9 becomes

$$\begin{cases} X = \frac{\tau_2}{\tau_3} \\ Y = \tau_3 \end{cases} \tag{5.11}$$

  This leads to:

$$J_0 = G[\tau_1(1-2\eta)\mu_1 + \tau_2\mu_2\eta + \tau_3\mu_3\eta] \tag{5.12}$$

  Assuming that the recombination time is $\tau_1 = \tau_2 = \tau$, because in this case there is no chance of spin flip, the n_3 are almost immobile thus their contribution to the total current is zero. The total current is then given by:

$$J_\infty = G\tau\mu_1[1+\eta(\frac{\mu_2}{\mu_1}-2)] \tag{5.13}$$

  It is unlikely that the mobility of n_2 be larger than the mobility of n_1. A plot of J_∞ is simulated (Figure 5.13) and as expected, the current decreases as the trap density is increased.

- In case the spin lattice relaxation time is equal to zero $t_{sl} = 0$, we get

$$\begin{cases} X = 1 \\ Y = \frac{2}{\frac{1}{\tau_2}+\frac{1}{\tau_3}} \end{cases} \tag{5.14}$$

  If we assume that $\tau_1 = \tau_2 = \tau_3 = \tau$ and neglecting the mobilities of n_3 we obtain the same current as in the condition $t_{sl} \to \infty$, namely,

$$J_{00} = G\tau\mu_1[1+\eta(\frac{\mu_2}{\mu_1}-2)] \tag{5.15}$$

  However in case $\tau_1 = \tau_2 = \tau =\neq \tau_3$ with $\theta = \frac{\tau_2}{\tau_3}$, then

$$J_{01} = G\tau\mu_1[1+\eta(\frac{1}{1+\theta}\frac{\mu_2}{\mu_1}-2)] \tag{5.16}$$

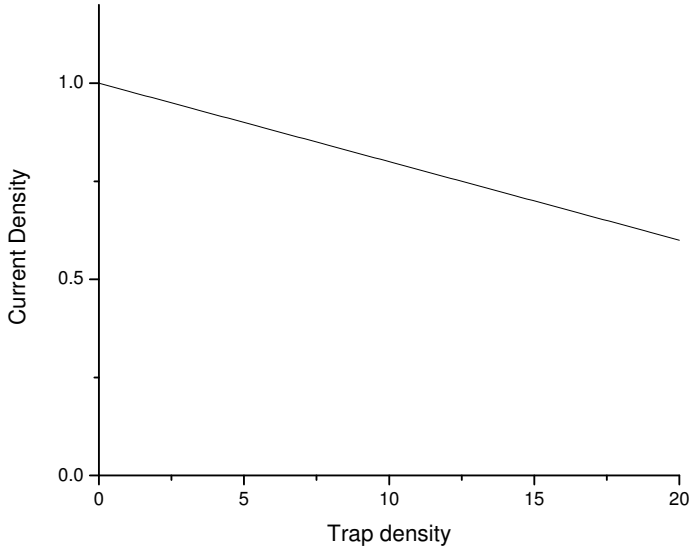

Figure 5.13. Current as a function of trap density when there are no radicals in the system.

So in any case, there is a cap to the current level in case the spin relaxation time is reduced.

The current thus goes from J_∞ to a higher value J_{01} or it remains the same when spin randomization is activated in the system. The sign of the derivative of XY if there is one should tell us if we have an increase in current in all cases or not. The derivative of XY is given by:

$$\frac{d(XY)}{dt_{sl}} = \frac{v_3(v_2 - v_3)}{v_3 + 2v} \tag{5.17}$$

where v_2, v_3 and v are, respectively, the inverses of τ_2, τ_3 and t_{sl}. We know that from Dr. Yang's [62] work that $\tau_2 < \tau_3$, which implies that $v_2 > v_3$; thus the derivative of XY is positive that is there is a maximum in the increase of the current as a function of the change in t_{sl}.

In summary, we know that the more radical we add in the system the more we reduce the spin lattice relaxation time. So when $t_{sl} \to \infty$ meaning the radical density is $N_{radicals} = 0$, the current density is J_∞. In between, we observe a maximum in the current as t_{sl} varies. However when $t_{sl} = 0$ i. e. $N_{radicals} \to 0$, the current goes back to the value J_∞ or J_{01}. Figure 5.14 represents the behavior of the current as a function of radical concentration as presented by this model.

5.3 Conclusion

The addition of spin 1/2 radicals has been shown as a means towards enhancing the device efficiency. The efficiency enhancement comes solely from the enhancement of the short circuit current. In order to determine the origin of this effect, we check all the parameters that contribute to the current in the device. The photocurrent action spectrum shows no new features except for the enhancement of the efficiency at each wavelength. We found that up to $100ps$ there is no change in the polaron generation rate. The recombination time of all the photogenerated polarons remains same and the film morphology does not change as well.

The only parameter that was found to change as radical's concentration was increased is the hole mobility. To explain this change in mobility, we proposed a model by which radicals induced not only an increase in trap density but also a decrease in spin lattice relaxation time. This decrease in spin lattice relaxation time allows the transit of some carriers that otherwise would have been blocked because of their spin orientation. This is the essence of Pauli blockade; carriers with spin parallel to the impurity spin orientation are reflected while carriers with spin antiparallel to the impurity are transmitted. The enhancement in the mobility comes from the fact that with the addition of radicals, the

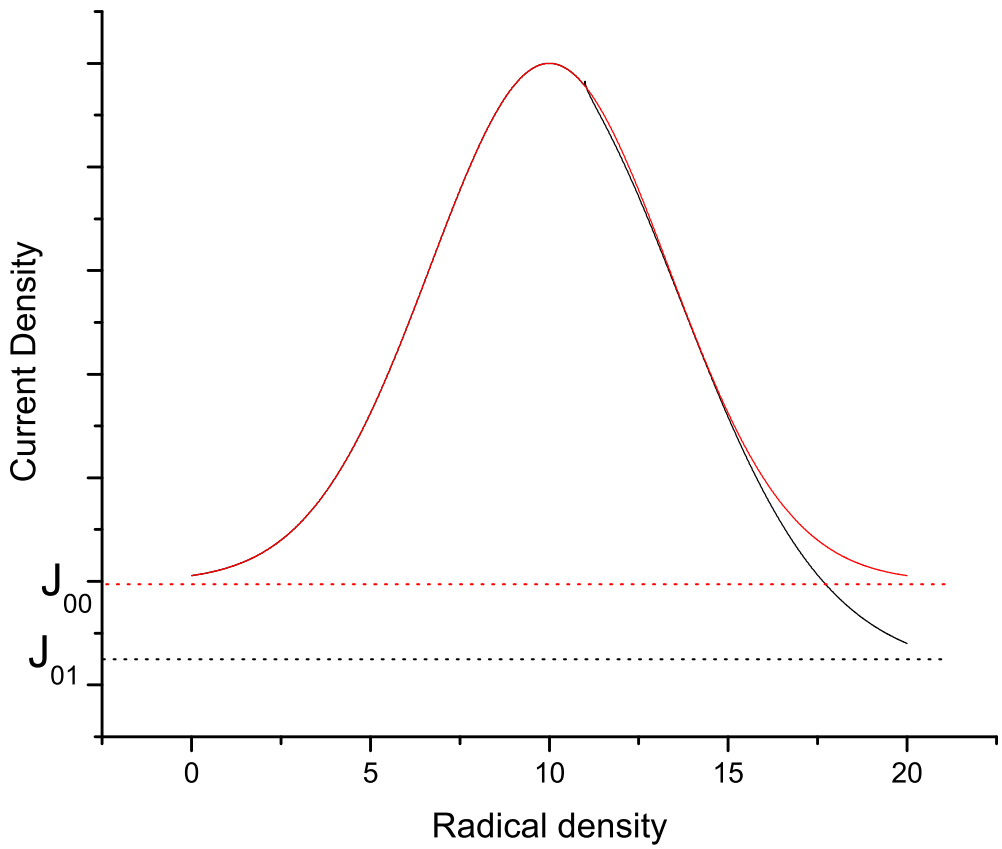

Figure 5.14. Current as a function of radical density.

spin lattice relaxation time is decreased. Thus blocked carriers can see their spin flip and rather than being reflected by the impurity, they are transmitted.

CHAPTER 6

CONCLUSION

In our studies of self-assembled monolayer diodes, we have fabricated solid state mixtures (SSM) of two different kinds of molecules; 1,4 benzene-dimethane-thiol (MeBDT) and 1-pentanethiol (PT). The first kind of molecules are called molecular wires due to their high conductivity compared to the second type which is dubbed molecular spacer as they have very little conductance. We found that by varying the concentration r of MeBDT with respect to that of PT, we can go from a regime of isolated molecular wires ($10^{-8} < r < 10^{-4}$) to a regime of aggregated molecular wires ($r > 10^{-3}$).

For $r = 0$, we found that a potential barrier caused by the spatial connectivity gap between the PT molecules and the upper Au electrode is dominant in the transport properties of the device. In the isolated molecules regime, the conductance of MeBDT dominated the transport. Temperature dependent studies of the electrical transport revealed the importance of the simultaneous bonding of the MeBDT molecules to both Au electrode. This was justified by the weak temperature dependence of devices in this regime compared to those with $r = 0$, from which we found that the energy difference between the Au electrode Fermi-level and the Me-BDT HOMO (or LUMO) level is $1.5eV$; whereas it is $2.5eV$ for the PT molecule.

Looking at the conductance of these devices at $V = 0.1V$, the "single molecule resistance" R_M was obtained. Consistent with previous measurements using other transport measuring techniques, it was found that $R_M = 6 \times 10^{-9}$.

In the aggregated molecule regime ($r > 10^{-3}$), an ohmic response in the current-voltage (I-V) characteristics was obtained for bias voltages up to $0.5V$, with the appearance of a new band in the differential conductance around $V = 0$. Also a new double absorption band feature appeared in the optical gap at $2.4eV$ that resulted in yellow/red photoluminescence emission. The novel optical and electrical properties obtained for the 2D SAM aggregates at $r > 10^{-3}$ were explained by the formation of electronic continuum states in the HOMO-LUMO gap of the Me-BDT molecule, which are caused by weak in-plane charge

delocalization among the Me-BDT molecules in the aggregates. To verify this model we also studied SAM 2D molecular diodes between Al electrodes. The $1eV$ difference in the electrode work function between Au and Al metals resulted in a pronounced shift of E_F with respect to the aggregate-related electronic states in the gap, and consequently, dramatically changed the device electrical I-V characteristics.

Our opto-electrical studies of bulk-hetero junction organic photovoltaic devices reveal that as far as the physics of the devices is concerned, there are very few similarities between these type of solar cells and the conventional solar cells. Just looking at the physical meaning of the open voltage circuit, and using a model developed for BOPV, we have reached the following conclusions:

- From the open circuit voltage, even though important from the engineering point of view, no intrinsic information on the device can be obtained
- V_{oc} maximum value is the build in potential. Therefore efforts to improve device efficiency should be directed to improve the build in voltage rather than V_{oc}

The origin of the build in potential was studied and was found to be dependent on electrodes' work function difference for a nonohmic contact configuration and on the blended materials in an Ohmic contact configuration. It was found that the build in potential is temperature dependent which can only be accounted for by the nondiscrete nature of the HOMO and the LUMO. In a bid to improve BOPV device performance, we added spin 1/2 radical molecules to the active layer blend . We found that while at concentrations higher than 5% an expected decrease in device performance was expected, for lower concentration (2%), an increase was instead observed. To explain the origin of this effect various studies were undertaken, among which were the admittance spectroscopy tool, which led us to the discovery of the mobility as the sole responsible factor for the above effect. A model based on Pauli blockade was used to justify these changes.

Our future plans include the direct measurement of the build in potential in bulk-hetero junction organic photovoltaic devices by means of electro-absorption to confirm the results obtained. A variation of the type of spin radical 1/2 radical molecules used will be another way to go to improve the overall device efficiency. I would like to take some time to write some papers out of this work and possibly declare a patent especially regarding the spin 1/2 radical effect.

REFERENCES

[1] G. E. Moore, Electronics **38** (1965).

[2] A. Aviram and M. A. Ratner, Chemical Physics Letters **29**, 277 (1974).

[3] J. Chen, M. A. Reed, A. M. Rawlett, and J. M. Tour, Science **286**, 1550 (1999).

[4] J. Chen, W. Wang, M. A. Reed, A. M. Rawlett, and J. M. Tour, Appl. Phys.Lett. **77**, 1224 (2000).

[5] A. M. Rawlett et al., Nanotechnology **14**, 377 (2003).

[6] Y. Xue, S. Datta, and M. A. Ratner, The Journal of Chemical Physics **115**, 4292 (2001).

[7] M. Di Ventra, S. T. Pantelides, and N. D. Lang, Phys. Rev. Lett. **84**, 979 (2000).

[8] G. K. Ramachandran et al., science **300**, 1413 (2003).

[9] A. Ulman, Accounts of chemical research **34**, 855 (2001).

[10] D. Y. Goswami, F. Kreith, and J. F. Kreider, *Principles of Solar Engineering*, Taylor and Francis, Philadelphia, 2000.

[11] M. Gratzel, J. of Sol-Gel Sci. and Tech. **22**, 7 (2001).

[12] M. J. Cass, F. L. Qiu, A. B. Walker, A. C. Fisher, and L. M. Peter, Journal Of Physical Chemistry B **107**, 113 (2003).

[13] B. O'Regan and M. Gratzel, Nature **353**, 737 (1991).

[14] C. W. Tang, Applied Physics Letters **48**, 183 (1986).

[15] N. S. Sariciftci, L. Smilowitz, A. J. Heeger, and F. Wudl, Science **258**, 1474 (1992).

[16] C. J. Brabec et al., Chemical physics letters **340**, 232 (2001).

[17] C. L. Braun, The Journal of Chemical Physics **80**, 4157 (1984).

[18] T. E. Goliber and J. H. Perlstein, J. chem. phys. **80**, 4162 (1984).

[19] A. J. Heeger, Angew. Chem. Int. Ed. **40**, 2591 (2001).

[20] C. E. D. Chidsey, G. Y. Liu, P. Rowntree, and G. Scoles, Journal of chemical physics **91**, 4421 (1989).

[21] A. Ulman, *Self-Assembled Monolayers of Thiols, Thin Films*, Academic Press, San Diego, 1998.

[22] F. Schreiber, Prog. Surf. Sci. **65**, 151 (2000).

[23] C. Bain et al., Journal Of The American Chemical Society **111**, 321 (1989).

[24] K. A. Peterlinz and R. Georgiadis, Langmuir **12**, 4731 (1996).

[25] O. Dannenberger, M. Buck, and M. Grunze, J. Phys. Chem. **103**, 2202 (1999).

[26] M. Himmelhaus, F. Eisert, M. Buck, and M. Grunze, J. Phys. Chem. B **104**, 576 (2000).

[27] R. C. Haddon et al., Appl. Phys. Lett. **67**, 121 (1995).

[28] E. Frankevich, Y. Maruyama, and H. Ogata, Chem. Phys. Lett. **214**, 39 (1993).

[29] V. D. Mihailetchi et al., Adv. Funct. Mater. **13**, 43 (2003).

[30] T. A. Chen, X. W. Reuben, and D. Riecke, J. Am. Chem. Soc. **117**, 233 (1995).

[31] Y. Kim et al., Status Solidi (a) **28**, 107 (2006).

[32] S. E. Shaheen et al., Applied Physics Letters **78**, 841 (2001).

[33] C. J. Brabec, S. E. Shaheen, C. Winder, N. S. Sariciftci, and P. Denk, Applied Physics Letters **80**, 1288 (2002).

[34] S. Kar, Applied Surface Science **11**, 3961 (2006).

[35] H. C. F. Martens, H. B. Brom, and P. W. M. Blom, Phys. Rev. B **60**, R8489 (1999).

[36] E. Lebedev, T. Dittrich, V. Petrova-Koch, S. Karg, and W. Brutting, Applied Physics Letters **71**, 2686 (1997).

[37] Z. Bao, A. Dodabalapur, and A. J. Lovinger, Applied Physics Letters **69**, 4108 (1996).

[38] M. A. Lampert and P. Mark, *Current injection in solids*, Academic Press, New York, 1970.

[39] D. Lungenschmiedt, *Injektions-und Rekombinationsphnomene in organischen Dunnschichtbauelementen*, Linz Institute, Linz, 2002.

[40] I. Shao and G. T. Wright, Solid State Electronics **3**, 291 (1961).

[41] I. Dudeck and R. Kassing, J. Appl. Phys **48**, 4413 (1977).

[42] V. Burtman, A. S. Ndobe, and Z. V. Vardeny, Journal of Applied Physics **98**, 034314 (2005).

[43] C. K. Chiang et al., Phys. Rev. Lett. **39**, 1098 (1977).

[44] H. Shirakawa, E. Louis, A. G. Macdiarmid, C. Chiang, and A. Heeger, Journal of the chemical society, chemical communications **10**, 578 (1977).

[45] R. Hesper, *The influence of surfaces and interfaces on the properties of C60 compounds*, PhD. Thesis, Groningen, 2000.

[46] R. E. Peierls, *Quantum Theory of Solids*, Oxford University Press, London, 1955.

[47] A. J. Heeger, S. Kivelson, J. R. Schrieffer, and W. P. Su, Rev. Mod. Phys. **60**, 781 (1988).

[48] V. Burtman, A. S. Ndobe, X. Jiang, and Z. V. Vardeny, Synthetic metals **154**, 329 (2005).

[49] C. Joachim, J. Gimzewski, and A. Aviram, Nature **408**, 541 (2000).

[50] S. L. Sargent, Bull. Of the Meteorological Soc. **53**, 360 (1972).

[51] J. A. Duffie and W. A. Beckman, *Solar Engineering of Thermal Processes*, J. Wiley, New York, 1991.

[52] C. L. Braun, The Journal of Chemical Physics **80**, 4157 (1984).

[53] C. Waldauf, *PhD thesis*, University of Oldenburg, Oldenburg, 2001.

[54] P. Schilinsky, C. Waldauf, J. H., and C. J. Brabec, Journal of Applied Physics **95**, 2816 (2004).

[55] A. Hannah, *World First - 5.4% Efficiency from Single Layer Organic Solar Cells*, http://www.plextronics.com/press.aspx?view=100, 2007.

[56] X. Wei, M. Raikh, Z. V. Vardeny, Y. Yang, and D. Moses, Phys. Rev. B **49**, 17480 (1994).

[57] C. M. Ramsdale et al., Journal of Applied Physics **92**, 4266 (2002).

[58] C. J. Brabec et al., Advance Functional Materials **11**, 374 (2001).

[59] A. Gadisa, M. Svensson, M. R. Andersson, and O. Inganäs, Applied Physics Letters **84**, 1609 (2004).

[60] V. D. Mihailetchi, P. W. M. Blom, J. C. Hummelen, and M. T. Rispens, Journal of Applied Physics **94**, 6849 (2003).

[61] J. Liu, Y. Shi, and Y. Yang, Advanced Functional Materials **11**, 420 (2001).

[62] C. G. Yang, E. Ehrenfreund, and Z. V. Vardeny, Physical Review Letters **99**, 157401 (2007).

[63] X. Jiang, *Photophysics of organic semiconductor films*, University of Utah, 2004.

[64] Y. Kim et al., Nature Materials (2006).

[65] J. C. Scott et al., Synthetic Metals **111-112**, 289 (2000).

[66] A. J. Mozer and N. S. Sariciftci, Chemical Physics Letters **389**, 438 (2004).